ION CRYSTALS PRODUCED BY LASER AND SYMPATHETIC COOLING IN A LINEAR RF ION TRAP

A Dissertation

by

FENG ZHU

Submitted to the Office of Graduate Studies of
Texas A&M University
in partial fulfillment of the requirements for the degree of

DOCTOR OF PHILOSOPHY

December 2010

Major Subject: Physics

Ion Crystals Produced by Laser and Sympathetic Cooling

in a Linear RF Ion Trap

ION CRYSTALS PRODUCED BY LASER AND SYMPATHETIC COOLING IN A LINEAR RF ION TRAP

A Dissertation

by

FENG ZHU

Submitted to the Office of Graduate Studies of
Texas A&M University
in partial fulfillment of the requirements for the degree of

DOCTOR OF PHILOSOPHY

Approved by:

Chair of Committee,	Hans A. Schuessler
Committee Members,	Siu A. Chin
	Alexei V. Sokolov
	Philip R. Hemmer
Head of Department,	Edward S. Fry

December 2010

Major Subject: Physics

ABSTRACT

Ion Crystals Produced by Laser and Sympathetic Cooling

in a Linear RF Ion Trap. (December 2010)

Feng Zhu, B.S., Tsinghua University, China;

M.S., Texas A&M University

Chair of Advisory Committee: Dr. Hans A. Schuessler

A detailed investigation of ion crystals produced by laser and sympathetic cooling in a linear RF trap has been conducted.

The laser cooling methods were examined and applied to the trapped $^{24}Mg^{+}$ ions. The crystals produced by the laser cooling were studied, including the dependence on RF voltage, end cap DC voltage, laser power and laser frequency. By manipulating the different RF voltages and endcap DC voltages, the structure phase transition of the ion crystals was observed.

In addition, the sympathetic cooling of different ion species with the laser cooled $^{24}Mg^{+}$ was carried out. In this process, the mixed Mg^{+} and He^{+} crystals were created and identified, and mixed Mg^{+} and H_2^{+} crystals were produced. The effect of an unwanted chemical reaction of Mg^{+} and H_2 was observed and minimized. After sympathetic cooling of light ion species, the sympathetic cooling of heavy molecular ions such as fullerene ions was also carried out. The efficiencies and final temperature in both cases are very different. Theoretically to interpret the results, molecular dynamics simulations

of the laser cooling and sympathetic cooling were implemented. And the simulations were compared with the experimental results.

In the process of carrying out this research, the optics were rebuilt to provide reliable UV sources for the photoionization and laser cooling of Mg ions. The imaging system was reconfigured to take the images of ion crystals. New elements were added tin the ion trap to improve the ability to manipulate ions.

ACKNOWLEDGEMENTS

I would like to thank my advisor and committee chair, Dr. Hans A. Schuessler, for his guidance and support throughout all the stages of the research. The members of my Ph.D. committee, Dr. Siu A. Chin, Dr. Alexei V. Sokolov, Dr. Philip R. Hemmer have my thanks for all their time and help.

The Department of Physics & Astronomy, Texas A&M University has my thanks for the financial assistantship in the past few years. I also acknowledge the Robert A. Welch Foundation, the National Priority Research Project of the Qatar Foundation and the National Science Foundation for the financial support of this project.

I would also like to express my appreciation to all of the wonderful people who have worked in our lab. Dr. Gerhard Paulus, Dr. Alexander Kolomenski, Dr. James Strohaber, Dr. Xiaojun Liu, Dr. Sergei Jerebtsov, Dr. Vladimir Lioubimov, Xudong Xu, Yunfeng Li, Ricardo Nava, Francisco Pham, Nathan Hart, and Cade Perkins, it has been a pleasure to work in the laboratory with them.

Prof. T. W. Hänsch and Dr. Thomas Udem from Max Planck Institute for Quantum Optics (MPQ, Garching, Germany) have my special thanks. It’s a privilege to work in MPQ during several summers. In particular, it's an honor to work with Dr. Maximilian Herrmann, Sebastian Knünz, and Valentine Batteiger. And many thanks go to Dr. Roland Holzwarth, Dr. Christopher Gohle, Dr. Guido Saathoff, Dr. Janis Alnis, Akira Ozawa, Helmut Brückner, Wolfgang Simon from MPQ.

Many thanks to Thomas Weimer and Ronald Page in the Machine Shop and Steve Payne and Erwin Thomas in the Electronic Shop for the work they have done for this research as well as valuable advice.

Chris Jaska from Spectra Physics has my special thanks for the instructions with the lasers.

TABLE OF CONTENTS

CHAPTER Page

CHAPTER Page

LIST OF FIGURES

FIGURE Page

FIGURE Page

FIGURE Page

LIST OF TABLES

CHAPTER I

INTRODUCTION

In 1958, Wolfgang Paul invented the first radio frequency (RF) ion trap [1, 2]. In 1978, two research groups demonstrated the laser cooling of single trapped ions independently [3, 4]. In 1989, the Nobel Prize in Physics was awarded to Wolfgang Paul and Hans Dehmelt for the development of ion trap technique. By now, the ion trap has evolved to a very important tool for fundamental and applied research [5, 6].

The most important feature of an ion trap is the ability to isolate and store charged particles such as ions and electrons. In a linear RF trap, the ions are trapped radially by RF field and axially by DC field, and usually they are stored under ultra high vacuum (UHV) conditions. At the same time, the Coulomb forces keep them apart. As a result, a sparse ion cloud is floating in the UHV for long period of time (hours and days). With the laser Doppler cooling, the ions will lose their translational kinetic energies. In this cooling down process the ion cloud undergoes the phase transition from a gaseous chaotic cloud to an ordered ion crystal [7].

The beauty and rich physics of the ion crystals formed by laser cooled ions is drawing increased attention and being applied to various research areas, not only to spectroscopic applications [8, 9], but also to other growing new research areas. Atomic clocks based on laser cooled single ions were developed, which are discussed to be a new frequency standard [10]. The first proposal to use stored ions for such a standard

---

This dissertation follows the style of Physical Review A.

was for Mercury ions by Hans A. Schuessler [11], present standards are based on this system. Experiments on trapped ions demonstrated quantum gates for the first time [12, 13], and simple algorithm were carried out [14], these paved the way to quantum computing [15].

Moreover, a large number of the ion species, which could not be directly cooled by lasers, can be sympathetically cooled by simultaneously trapped laser cooled ions through the mutual Coulomb interaction. Such sympathetic cooling is being employed to cool any (singly charged) atomic or molecular ion species in the wide range of 1~470 atomic mass unit (amu), as well as much heavier ions (up to 12,400 amu) if they are highly charged [16]. This sympathetic cooling method facilitates a lot of research applications from cold ion-molecule chemistry [17] to high precision spectroscopy [18]. Translationally cold molecular ions are easily produced by the sympathetic cooling, which makes it possible to study the photochemical reactions, photodissociation and Coulomb explosion processes in detail [19].

In this dissertation, I describe my research on a detail study of the ion crystals produced by both laser and sympathetic cooling in a linear RF ion trap, not only experimentally but also supported by the molecular dynamics (MD) simulations. The research gives an insight into the dynamics of the laser cooling and sympathetic cooling. Also it reveals a lot of information of the ions in the crystals. It provides the starting point for different applications, such as the precision spectroscopy, cold ion molecule chemistry, etc.

Our linear RF ion trap is a versatile tool. Because of its large size, it is capable to trap millions of ions and form large ion crystals where the ions were well separated. This large size can however also trap single ions as well. Due to the large center segment, the distance between the individual ions is much larger than the distance in a conventional trap. In this way it provides a unique opportunity to study ion chain dynamics in long ion chains produced under low axial confinement. The study includes the generation of ion crystals, manipulation of the ion crystals by all the trapping and cooling parameters, such as the RF trapping voltages, end cap voltage, laser power, laser detuning, secular excitation, etc. When changing the RF trapping voltage and endcap voltage, the crystals undergoes the structural phase transition as the theory points out [20]. The structural phase transitions were observed and discussed in detail in this dissertation.

Also, it is important to study the sympathetic cooling with ions of different species. It is of interest to see if there is a charge to mass ratio limit for the heavier molecular ion to be crystallized, such as the fullerene ions with the laser cooled Mg^+. And He^+ and H_2^+ are two very important targets for the precision spectroscopy. It is crucial to study the various effects of the sympathetic cooling on these two species to make sure that the targets are ideal for spectroscopy with highest precision.

The basic experimental apparatus was developed in previous dissertation work by X. Zhao and V. Ryjkov [21, 22]. It consists of the vacuum chamber with a linear RF ion trap, the lasers and optical system, and related electronics and the data acquisition systems. To achieve the research goals of this proposal, the apparatus was significantly modified and expanded.

The pump laser was switched from an Ar ion laser to a more reliable diode pump solid state laser. Two dye lasers were realigned, two new second harmonic generation cavities were built, the whole optics were rebuilt to provide reliable UV sources for the photoionization of Mg atoms and cooling of Mg^+ ions. The image system was realigned to take the photos of not only the single ions but also large and small ion crystals. Some additional ion manipulation electrodes were added on the linear RF trap, electronics as well as the experimental control software were improved to yield good control of trapped ions. With this improved apparatus, the studies of the ion crystals produced by laser and sympathetic cooling were conducted.

In order to better understand the laser and sympathetic cooling, molecular dynamics simulations were carried out and compared with the experimental results. The purpose of the MD simulation is to get insight into the physics of both laser cooling and sympathetic cooling mechanisms. With the MD simulations compared to the experimental results, several parameters of the process were revealed, in particular, the crystal temperature, ion numbers in a large crystal, effect of sympathetic cooling, etc.

The MD simulations are a flexible and efficient tool, the effect of various heating or cooling factors could be studied simultaneously or individually. In particular, the simulations can be performed with the time varying RF potential, or in the pseudo potential approximation, and the results were compared. Also the MD simulations are in agreement with the results from other group [23].

CHAPTER II

ION TRAPPING AND COOLING

This chapter provides the basic theoretical frame work for ion trapping and cooling. The focus is on the confinement of ions in a linear RF trap, and on Doppler cooling, because these two factors are the most important elements to form the ion crystals. Also trapping and cooling of different ion species are introduced at the last section of this chapter.

2.1 Ion trapping

To trap a charged particle in free space, it is necessary to create a three dimensional potential well. However, according to Earnshaw's theorem, no three dimensional potential well can be created by static electric fields [24]. Therefore, there are two kinds of ion traps to circumvent this restriction: time dependent electric potential used in Paul trap or RF trap [1, 2], or static magnetic and electric field in Penning trap [25, 26].

2.1.1 RF trap

In an RF trap, an alternating quadrupole elcctric field is used to trap ions. With well chosen frequency and amplitude, the quadrupole electric field generates on average a three dimensional potential well.

In a quadrupole field, the potential φ is given by

$$\varphi = \frac{\varphi_0}{2r_0^2}(\alpha x^2 + \beta y^2 + \gamma z^2), \tag{2.1}$$

where φ_0 is an electric potential applied on the electrodes, r_0 is the distance from the trap center to the electrodes. To fulfill the Laplace's equation, it must have

$$\nabla^2 \varphi = \frac{\varphi_0}{r_0^2}(\alpha + \beta + \gamma) = 0, \tag{2.2}$$

$$\alpha + \beta + \gamma = 0. \tag{2.3}$$

Two usual choices are $\alpha = \beta = -2\gamma$ and $\alpha = -\beta$, $\gamma = 0$. The first one corresponds to a spherical RF trap, in which the ions are confined by three dimensional quadrupole RF field. The second one corresponds to a linear RF trap, in which the ions are confined radially by quadrupole RF field, and axially by DC field. Fig. 1 shows the typical electrode structure for both, namely a three dimensional RF trap and a linear RF trap.

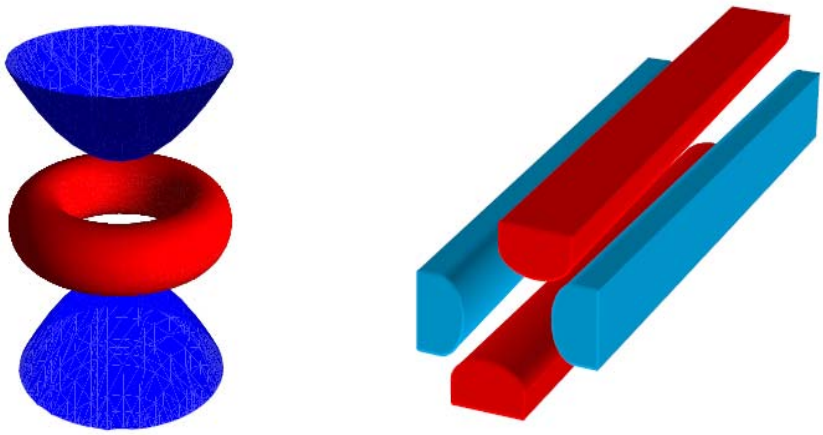

Fig. 1. Electrode structure for a three dimensional and a linear RF trap.
(Left, a three dimensional RF trap; right, a linear RF trap.)

The electrodes with the same colors in Fig. 1 are connected together, and the RF voltages are applied to the electrodes with different colors. In a spherical trap, ions are only confined in a region around the trap center. In a linear trap, the confinement region is actually along the whole electrode length, which allows trapping millions of ions. Also, in a linear trap, segmentation is possible, so the trapped ions can be manipulated by applying different DC voltage to separated segments. Another advantage is that a linear trap provides better access to the trapped ions than a spherical trap. And for laser spectroscopy, all ions can be illuminated by the laser beam in a linear trap. For these reasons, a linear trap was assembled and is the main device in our laboratory.

2.1.2 Radial confinement of a linear RF trap

RF traps use the alternating quadrupole potential to trap ions. The ideal shape of the confining electrodes is the equal potential surfaces of the quadrupole field, which is hyperbolic in shape. In practice, cylindrical electrodes are used, because they are easy to make and provide good optical access. Also if the electric field of the cylindrical electrodes is expanded, the lowest order is quadrupolar. Thus as long as the ions are confined in the small region of along the trap axis, approximately they can be treated as driven by the quadrupole electric field.

The geometry of linear RF trap used in the experiments is showed as Fig. 2.

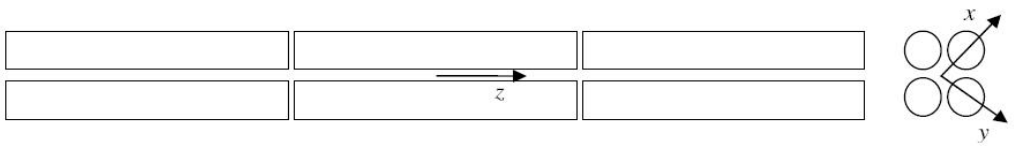

Fig. 2. The ion trap geometry.

The quadrupole RF potential near the center of the trap is:

$$\varphi(x,y,t) = (U - V\cos(\Omega t))\frac{x^2 - y^2}{2r_0^2}, \tag{2.4}$$

where $-V\cos(\Omega t)$ is the RF signal applied on the electrodes, the frequency Ω is usually in the order of several MHz, radio frequency range. The amplitude V varies from tens to thousands of volts, depending on mass of the trapping species. U is the DC offset applied to the electrodes, and r_0 is the distance from the trap center to the electrode surface.

Suppose there is a particle with mass m and charge e in this trapping area, by Newton's second law, the equations of the motion are:

$$\frac{d^2x}{dt^2} + \frac{e}{mr_0^2}(U - V\cos(\Omega t))x = 0, \tag{2.5}$$

$$\frac{d^2y}{dt^2} - \frac{e}{mr_0^2}(U - V\cos(\Omega t))y = 0, \tag{2.6}$$

$$\frac{d^2z}{dt^2} = 0. \tag{2.7}$$

In this incomplete description, in z direction, the ions are free. The confinement of z direction will be discussed in next section. In x and y direction, the equations can be transformed to the well known Mathieu equation by introducing the following dimensionless parameters,

$$a = a_x = -a_y = \frac{4eU}{mr_0^2\Omega^2}, \tag{2.8}$$

$$q = q_x = -q_y = \frac{2eV}{mr_0^2\Omega^2}, \tag{2.9}$$

$$\eta = \frac{\Omega t}{2}. \tag{2.10}$$

If Eq. (2.8) to (2.10) are substituted into Eq. (2.5) and (2.6), it shows the motions of *x* and *y* direction is governed by the Mathieu differential equation,

$$\frac{d^2u}{d\eta^2} + (a - 2q\cos(2\eta))u = 0. \tag{2.11}$$

The coefficient of this differential equation is periodic, according to Flogquet theorem, the general solutions have the same periodicity,

$$u(\eta) = Ae^{i\beta\eta}\sum_{n=-\infty}^{\infty} C_{2n}e^{i2n\eta} + Be^{-i\beta\eta}\sum_{n=-\infty}^{\infty} C_{2n}e^{-i2n\eta}. \tag{2.12}$$

Eq. (2.12) shows that the stable solution exists only if the characteristic exponent β is real and not integer, which means the lowest stability range for β is (0, 1), while *A* and *B* are constants, which depend on the initial conditions. By plugging Eq. (2.12) to Eq.(2.11), a recursion relation of C_{2n} appears,

$$C_{2n}[a - (2n+\beta)^2] - qC_{2n+2} - qC_{2n-2} = 0. \tag{2.13}$$

This can be written as,

$$\frac{C_{2n}}{C_{2n-2}} = \frac{q}{[a - (2n+\beta)^2][1 - \frac{q}{a-(2n+\beta)^2}\frac{C_{2n+2}}{C_{2n}}]}. \tag{2.14}$$

For *n*=0, Eq. (2.14) follows,

$$\beta^2 = a - \frac{1}{(\frac{C_0}{C_{-2}})}q - \frac{C_2}{C_0}q. \tag{2.15}$$

By continuing to insert Eq. (2.14) into Eq. (2.15), the characteristic exponent β is

$$\beta^2 = a + \cfrac{q^2}{(\beta+2)^2 - a - \cfrac{q^2}{(\beta+4)^2 - a - \cfrac{q^2}{(\beta+6)^2 - a - \cdots}}} + \cfrac{q^2}{(\beta-2)^2 - a - \cfrac{q^2}{(\beta-4)^2 - a - \cfrac{q^2}{(\beta-6)^2 - a - \cdots}}} \quad . \quad (2.16)$$

Bounded by the pairs of a and q, which give that the value of β equals integer, the stability region can be plotted as Fig. 3.

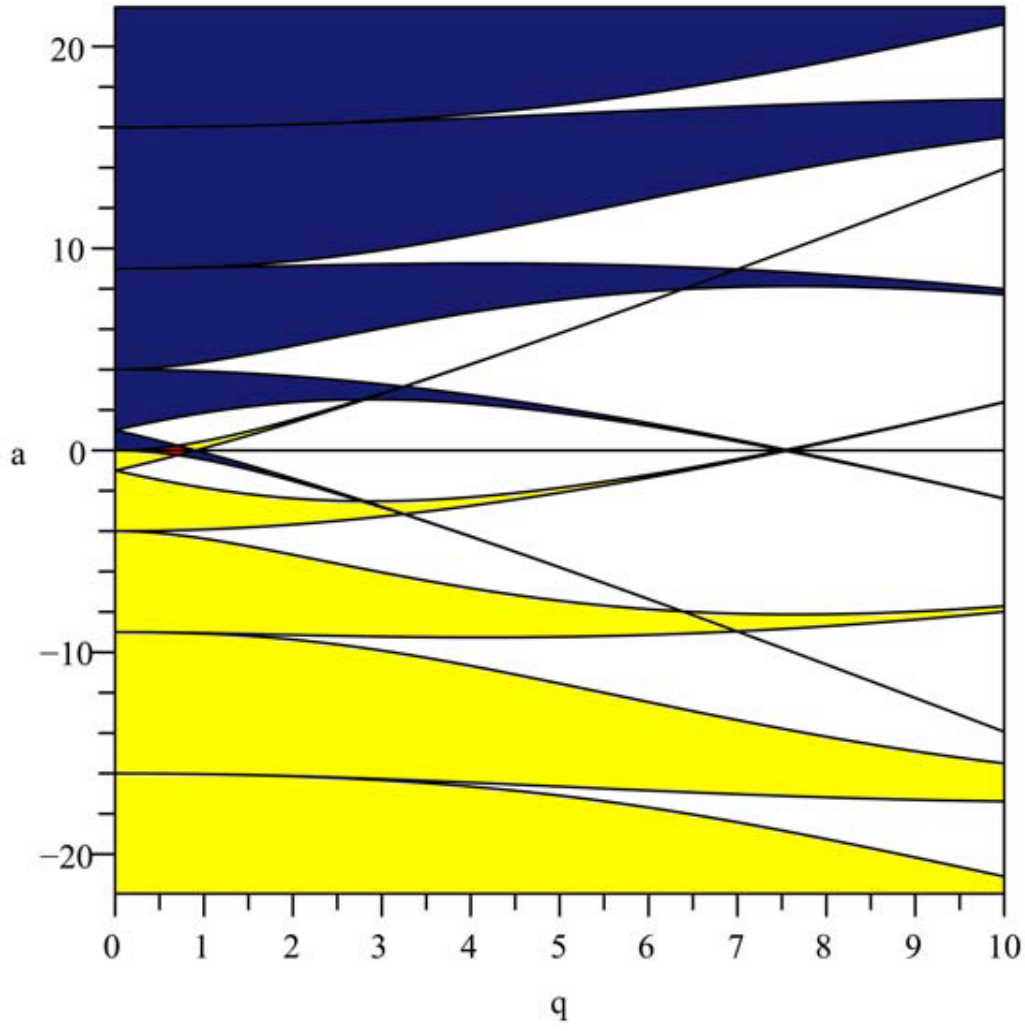

Fig. 3. Stability diagram in the (a,q) plane for a linear RF trap. The yellow areas are the stability regions along the x axis. The blue areas are the stability regions along the y axis.

The stability region which contains $a \to 0$ and $q \to 0$ and bounded by $\beta=0$ and $\beta=1$ is called the lowest stability region. Most of the RF ion traps including the trap in our laboratory are operating in the lowest stability region, as Fig. 4 shows.

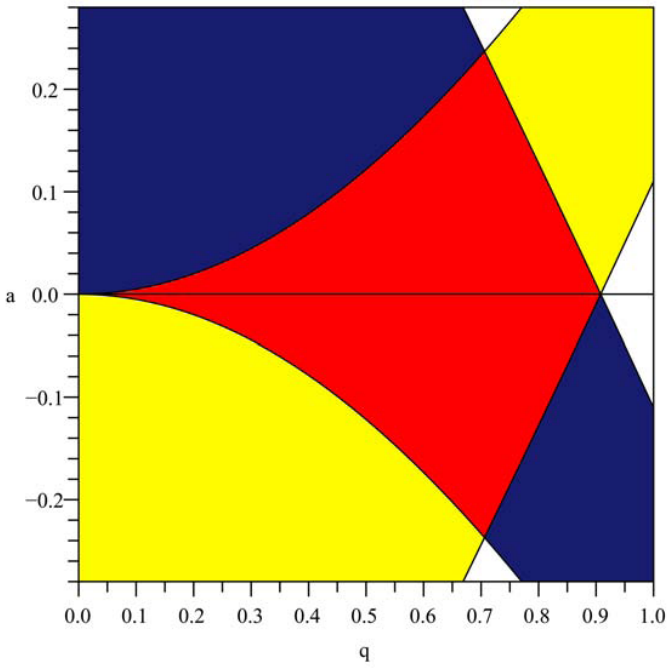

Fig. 4. Lowest stability region for a linear RF trap. The yellow areas are the stability regions along the x axis. The blue areas are the stability regions along the y axis.

For small a and q, more precisely $|a| \ll 1$ and $q^2 \ll 1$, the Eq. (2.16) simplifies to,

$$\beta^2 = a + \frac{1}{2}q^2 . \tag{2.17}$$

With this approximation, the general solutions can be simplified as,

$$u(t) = u_0 \cos(\frac{\beta}{2}\Omega t)[1 - \frac{q}{2}\cos(\Omega t)] . \tag{2.18}$$

The Eq. (2.18) reveals that the trapped ions oscillate with two superimposed motions. First, the ions are oscillating with large amplitude and a slow frequency of

$\omega_s = \beta\Omega/2$, this motion is usually called the secular motion, and the frequency is labeled as secular frequency. Second, the ions are driven by the trapping field, oscillating with the trapping frequency Ω. The amplitude of this motion depends on the position of the ions, if the ion is at the trap center, the amplitude is zero, if the ion is the largest displacement of the secular motion, the amplitude is maximal, but $q/2$ times smaller than the secular motion. This motion is usually called micro motion. Fig. 5 shows the trajectories of different a and q settings.

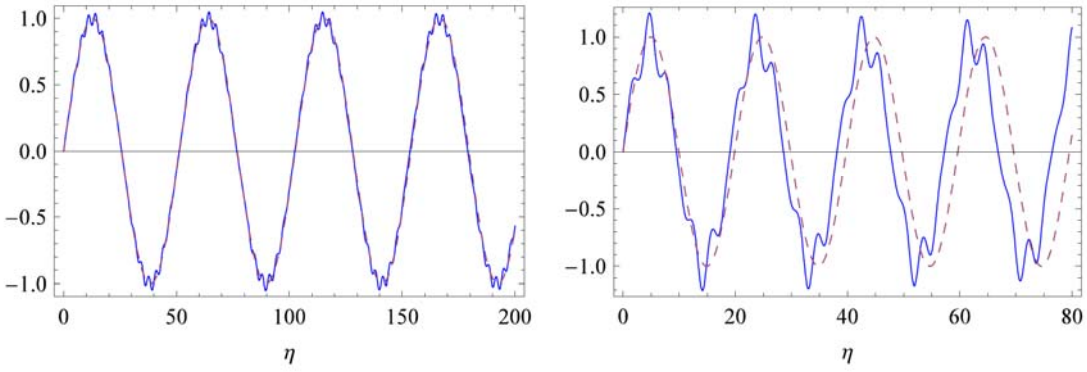

Fig. 5. Trajectories of different a and q settings.
a=0.01 and q=0.1 (left), a=0.02 and q=0.4 (right).

For the left part of Fig. 5, a=0.01 and q=0.1, the blue line is plot directly from the odd solution of Mathieu's equation, while the red dashed line was plot by the corresponding secular motion part from Eq. (2.18). The ion oscillates at the secular frequency with micro motion superimposed, and the amplitude of the micro motion increases as the distance from the axis increases. For the right part of Fig. 5, a=0.02 and q=0.4. The condition of $|a| \ll 1$ and $q^2 \ll 1$ is not fulfilled, the two lines are separated more

and more with time goes on, which means the motion of the ion can not be described by Eq. (2.18).

Another approach to describe the secular motion is by the pseudo potential approximation [27]. In the two dimensional case, assuming a=0, which means no DC offset. The time averaged pseudo potential can be calculated as following:

$$\Psi(x,y)=\frac{e}{4m\Omega^2}[(\frac{\partial\tilde{\varphi}}{\partial x})^2+(\frac{\partial\tilde{\varphi}}{\partial y})^2]=\Psi_o\frac{x^2+y^2}{r_0^2}, \tag{2.19}$$

where $\tilde{\varphi}$ is the spatial part of the quaduapole field and Ψ_0 is the trap depth. With U=0, insert the spatial part of Eq. (2.4) into Eq. (2.19), then the pseudo potential for the linear RF trap is

$$\Psi(x,y)=\frac{eV^2}{4m\Omega^2r_0^2}\frac{x^2+y^2}{r_0^2}. \tag{2.20}$$

And the trap depth is

$$\Psi_0=\frac{eV^2}{4mr_0^2\Omega^2}=\frac{1}{8}qV. \tag{2.21}$$

The typical value for the trap depth of a singly charged ion is around eV range. With the pseudo potential model, the trapped ions oscillate in a harmonic potential well. The trap depth is defined as the potential difference from the trap center to the surface of electrode. Thus, the secular frequency for the pseudo potential can be calculated as

$$\frac{1}{2}m\omega_{secular}{}^2r_0^2=e\Psi_0, \tag{2.22}$$

$$\omega_{secular}=\sqrt{\frac{2e\Psi_0}{mr_0^2}}=\sqrt{\frac{2e}{mr_0^2}\frac{1}{8}qV}=\sqrt{\frac{2eV}{mr_0^2\Omega^2}\frac{1}{8}q\Omega^2}=\frac{1}{2\sqrt{2}}q\Omega. \tag{2.23}$$

This is the same result with the secular motion part of Eq. (2.18).

2.1.3 Axial confinement of a linear RF trap

Since the quadrupole RF field in a linear RF trap does not confine the ions in the axial direction, other methods must be taken. The easiest way is to apply a DC voltage on the additional endcaps near the ends of the linear electrodes, as Fig. 6 shows.

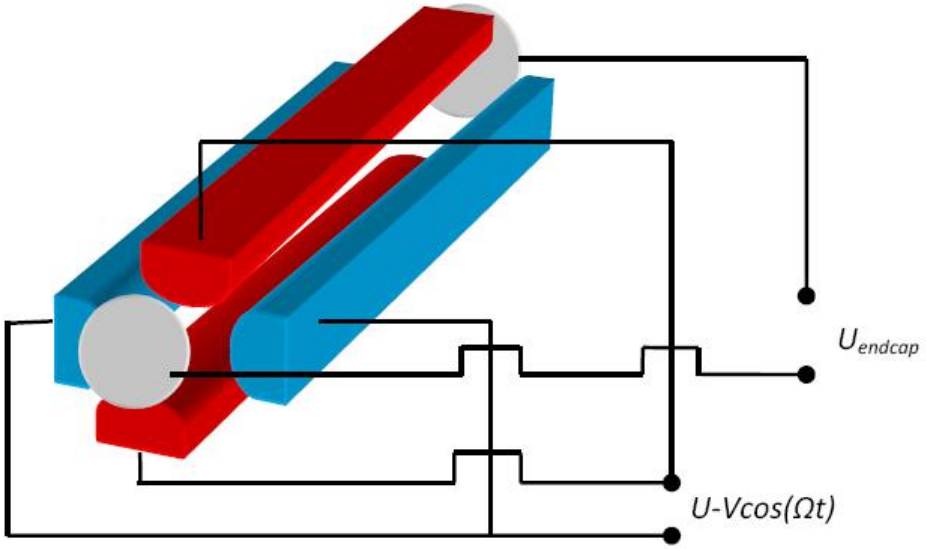

Fig. 6. Endcap voltage for the axial confinement.

For this case, the potential created near the trap center by this boundary condition is:

$$\varphi_{endcap} = \frac{\kappa U_{endcap}}{z_0^2}[z^2 - \frac{1}{2}(x^2 + y^2)], \tag{2.24}$$

where U_{endcap} is the DC voltage applied on the endcap, κ is the geometry factor, z_0 is the distance from the trap center to the endcap.

In the axial direction, the ions see a harmonic well near the trap center. The endcap potential also creates some DC offset in the radial direction, and this factor changes a in Eq. (2.8). If z_0 is much larger than r_0, as long as the U_{endcap} is not too high comparing with RF V, the small change of potential in the radial direction is negligible. If z_0 is comparable with r_0, not only a changes a lot, by using the pesudopotential model, the ω_s also needs to be modified. Combining Eq. (2.20) and (2.24), and ignoring the DC offset on the electrodes,

$$\Phi(x,y) = \frac{eV^2}{4m\Omega^2 r_0^2}\frac{x^2+y^2}{r_0^2} + \frac{\kappa U_{endcap}}{z_0^2}[z^2 - \frac{1}{2}(x^2+y^2)]. \qquad (2.25)$$

Then the secular resonance frequencies in radial and axial directions are:

$$\omega_r = \omega_x = \omega_y = \sqrt{\frac{e}{m}(\frac{qV}{4r_0^2} - \frac{\kappa U_{endcap}}{z_0^2})}, \qquad (2.26)$$

$$\omega_z = \sqrt{\frac{e}{m}\frac{2\kappa U_{endcap}}{z_0^2}}. \qquad (2.27)$$

2.1.4 Space charge effect

In the last two sub sections, the ions are treated individually to interact with the trap field. In a linear RF trap, up to several million ions can be trapped simultaneously. And all the ions are interacting with each other by Coulomb force. Thus the space charge effect is important because it eventually limits the maximum number of ions which can be trapped simultaneously.

The space charge effect is treated by the pseudo potential model. According to Dehmelt's model, because of the Coulomb repulsive force, the ions will rearrange

themselves in such a way that the potential is flat at the bottom and ions are at rest except for the micro motion [27]. Thus the Coulomb potential between the ions is ϕ_i, and the trap potential is pseudo potential Ψ,

$$\phi_i + \Psi = const. \tag{2.28}$$

And according to the Poisson relationship,

$$-\nabla^2 \phi_i = \nabla^2 \Psi = \frac{\rho_{\max}}{\varepsilon_0}, \tag{2.29}$$

where ρ_{max} is the maximum charge density of the trapped ions, ε_0 is the permittivity constant. Plug the Eq. (2.19) to Eq. (2.26), the maximum charge density is:

$$\rho_{mas} = \frac{4\varepsilon_0 \Psi_0}{r_0^2}. \tag{2.30}$$

Then the maximum ion number density is:

$$N_{\max} = \frac{\rho_{\max}}{e} = \frac{\varepsilon_0 V^2}{m r_0^4 \Omega^2}. \tag{2.31}$$

With the typical trap operating parameters for the $^{24}Mg^+$, V is about 100V, r_0 is 2.605 mm, Ω is 7.48 MHz. Eq. (2.31) gives a maximum trapped ion number density of $10^{10}/cm^3$. This density corresponds to a pressure of 10^{-7} mbar. In experiments, due to the heating from the applied RF field, residual gas collisions, electric potential imperfections, etc, the density is about one magnitude lower.

2.2 Ion cooling

The initial kinetic energies of trapped ions are usually about several eV, which corresponds to 10,000 K. Such a high temperature leads to a very large Doppler

broadening in a laser spectroscopy measurement. To avoid this, it is necessary to cool the ions. Before the invention of laser cooling, buffer gas cooling was often used. During the trapping process, Helium gas at room temperature as the buffer gas is leaked into the chamber. The collisions between the trapped ions and buffer gas atoms transfer the kinetic energy from the hot trapped ions to the buffer gas. The lowest temperature attainable in this method is limited to the buffer gas temperature at about 300 K. If the cryogenic technique is used, the temperature can reach several K [28, 29].

Since the beginning of the development of laser cooling, it was used to cool the trapped ions [3, 4]. If micro motion is negligible, the lowest temperature is limited by the natural linewidth of the transition used for the laser cooling [30].

There are many atomic or molecular ions could not be cooled by laser, either because no suitable laser source exists or the ions have no suitable transitions. In this case, the ions of interest can be stored simultaneously with another ion species which can be laser cooled directly. By the Coulomb interaction, the ions of interest will be sympathetically cooled by the laser cooled ions [31, 32].

2.2.1 Laser cooling

In 1975, T. W. Hänsch and A. L. Schawlow first proposed the idea of laser cooling [33]. The key physics behind laser cooling is that the momentum of the atom or ion is reduced by the asymmetry in an absorption-emission cycle of the interaction between the atom or ion and the laser.

In Doppler cooling, the laser cooling is realized by illuminating an ion with a narrow linewidth continuous wave (CW) laser tuned below a cycling transition. Due to

the first order Doppler effect, moving ions see laser light Doppler shifted, the ions moving against the propagation direction of the laser have a higher probability to absorb a photon than the ions moving away from the laser source. Absorbing a laser photon, the ion gets a momentum reduction by $\Delta p_{absorption} = \hbar k$, which lowers the velocity of the ion, k is magnitude the laser propagation vector. The emission process is generally isotropic, so the average momentum transfer from the decay of the excited state is zero, $< \Delta p_{emission} >= 0$. Thus the average net effect in one absorption emission cycle is the reduction of the momentum component towards the laser source by $\hbar k$. Usually free atoms can be cooled in three dimensions by three orthogonal laser beam pairs, and each pair has two counter propagation beams. While in an ion trap, it is sufficient to use only one laser beam at a small angle with respect to the trap symmetry axis for cooling.

As discussed in section 2.1.2, trapped ions oscillate with two superimposed motions, micro motion and secular motion. If the small amplitude micro motion is negligible, the ions can be treated as oscillating in a pseudo potential with secular frequency ω_s.

For the laser cooling process, the ion could be approximately treated as a two level system with ground state $|g\rangle$ and excited state $|e\rangle$. The ion can absorb a laser photon with ω_L, to jump from ground state $|g\rangle$ to excited state $|e\rangle$, which has a lifetime of $1/\gamma$, where γ is the natural linewidth of the transition. Then the ion emits a photon spontaneously and goes back to the ground state $|g\rangle$.

With the picture of ion secular motion and cooling process, two different cooling regime needs to be distinguished [34]: strong and weak binding. In the rest frame of an ion with secular motion, the laser beam is frequency modulated with ω_s. This generates sidebands of the carrier frequency $\omega_L \pm n\omega_s$. If $\omega_s \gg \gamma$, the sidebands are clearly distinguishable from the laser frequency. This situation is called strong binding. The motional sidebands can be addressed individually by the cooling laser, thus it allows resolved sideband cooling [35]. If $\omega_s \ll \gamma$, then the motional sidebands of the trapped ions are not resolved and the cooling is in the weak binding limit and treated as Doppler cooling. In other words, because the secular oscillation period of the ion is much longer than the absorption-emission cycle period, the secular motion of the ion in a trap can be neglected for the laser cooling process. In our trap, the ω_s is around 100 kHz range, while γ is in 42 MHz range, thus the laser cooling method in this dissertation is treated as Doppler cooling.

The fully quantum mechanics treatment of the laser cooling could be found in many references [34, 36]. Here a simple model which focuses on the laser cooling force is introduced [30, 36].

By using the density matrix method, the laser interaction with two level system leads the optical Bloch equations [36, 37]. Solving these equations in steady state, the population of the excited state is given by

$$\rho_{ee} = \frac{s/2}{1 + s + (2\delta_{eff}/\gamma)^2}, \tag{2.32}$$

where $s = I / I_{sat}$ is the dimensionless saturation factor, $I_{sat} = \frac{2\pi^2 \hbar c \gamma}{3\lambda^3}$ is the saturation intensity. Assume an ion is moving with a velocity component *v* to the laser source, the frequency of the transition is shifted due to the Doppler effected by a value *kv*. Thus the detuning $\Delta = \omega_L - \omega_{transition}$ is also Doppler shifted, and the effective detuning is $\delta_{eff} = \Delta - kv$.

The average force executed on an ion from absorption followed by a spontaneous emission in many cycles can be written as

$$F = \hbar k \gamma \rho_{ee}, \tag{2.33}$$

where $\hbar k$ is the momentum transfer from each photon to the ion, γ is the rate of the process, ρ_{ee} is the probability for the ion to absorb a photon to be in the excited state [30, 36].

Combine Eq. (2.32) and Eq. (2.33), the force resulting from the absorption followed by spontaneous emission becomes:

$$F = \frac{\hbar k s \gamma / 2}{1 + s + \frac{4(\Delta - kv)^2}{\gamma^2}}. \tag{2.34}$$

The force can be expanded in the order of *v*,

$$F = F_0 - \beta v + o(v^2), \tag{2.35}$$

$$F_0 = \frac{\hbar k s \gamma / 2}{1 + s + (2\Delta / \gamma)^2}, \tag{2.36}$$

$$\beta = \frac{-4\hbar k^2 s \Delta / \gamma}{[1 + s + (2\Delta / \gamma)^2]^2}, \tag{2.37}$$

where F_0 is the radiation pressure force, it does not depend on the velocity of the ion. When the s»1, the transition saturates, and the F_0 saturates at a maximum value of $\hbar k\gamma/2$, because the ρ_{ee} has a maximum value of ½ for a steady two level system.

The $-\beta v$ part is velocity dependent, and clearly a frictional damping of the motion, when Δ is negative (e.g. laser is red detuned). The damping coefficient β depends on both s and Δ, as can be seen in Fig. 7.

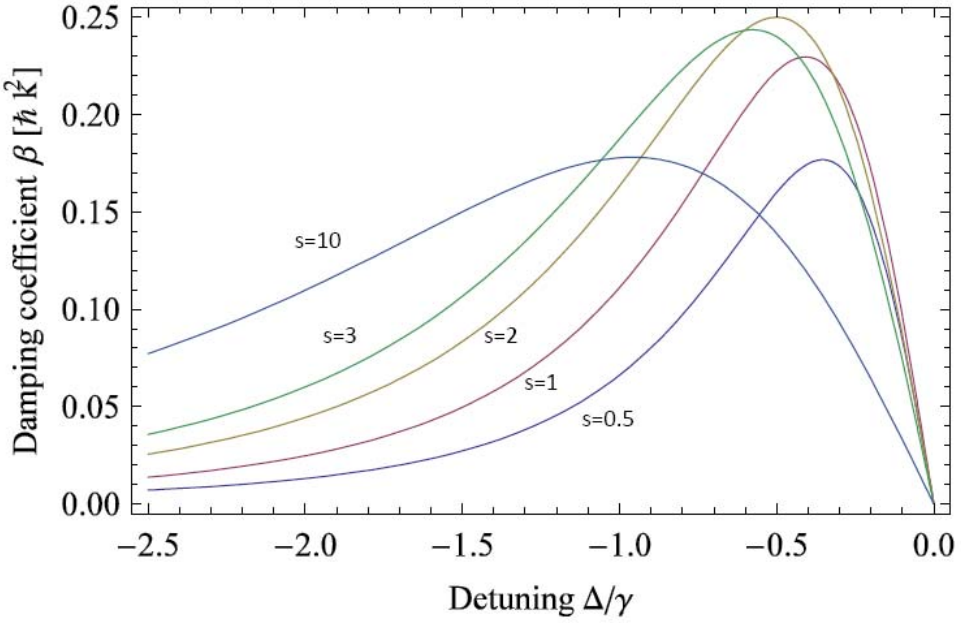

Fig. 7. The damping coefficient.

The maximum value of β is obtained when $\Delta = -\gamma/2$ and s=2,

$$\beta_{\max} = \hbar k^2/4 . \tag{2.38}$$

With the same condition, the radiation pressure force is:

$$F_0 = \hbar k\gamma/4 . \tag{2.39}$$

If the micro motion is negligible, the cooling power and heating power of an ion could be calculated and balanced to find the limiting temperature in Doppler cooling [30].

The average cooling power is:

$$\left\langle P_{cooling} \right\rangle = \left\langle Fv \right\rangle = \left\langle (F_0 - \beta v)v \right\rangle = F_0 \left\langle v \right\rangle - \beta \left\langle v^2 \right\rangle = -\beta \left\langle v^2 \right\rangle, \tag{2.40}$$

since the average $\langle v \rangle$ is 0.

The momentum kicks due to the absorption and emission have the same rate but different direction. By scaling the emission term with a geometry factor ξ which reflects the average component of the emission recoil kick along the x axis, the heating power is approximately:

$$\left\langle P_{heating} \right\rangle = \frac{1}{2m}\frac{d}{dt}\left\langle p^2 \right\rangle = \dot{E}_{abs} + \dot{E}_{em} = \dot{E}_{abs}(1+\xi) \approx \frac{1}{2m}(\hbar k)^2 \gamma \rho_{ee}(1+\xi), \tag{2.41}$$

m is the mass of the ion, ξ=2/5 is a factor that takes non isotropic emission pattern of dipole radiation into account, and in the final stage of cooling, v is close to zero, thus ρ_{ee} takes the value at v=0 [30].

For equilibrium system, the sum of the cooling power and the heating power should be zero, and the Doppler limit temperature is:

$$m\left\langle v^2 \right\rangle = k_B T = \frac{\hbar\gamma}{8}(1+\xi)[(1+s)\frac{\gamma}{2(-\Delta)} + \frac{2(-\Delta)}{\gamma}], \tag{2.42}$$

$$T = \frac{\hbar\gamma}{8k_B}(1+\xi)[(1+s)\frac{\gamma}{2(-\Delta)} + \frac{2(-\Delta)}{\gamma}]. \tag{2.43}$$

The limit temperature of the Doppler cooling as a function of the detuning of the cooling laser is shown in Fig. 8.

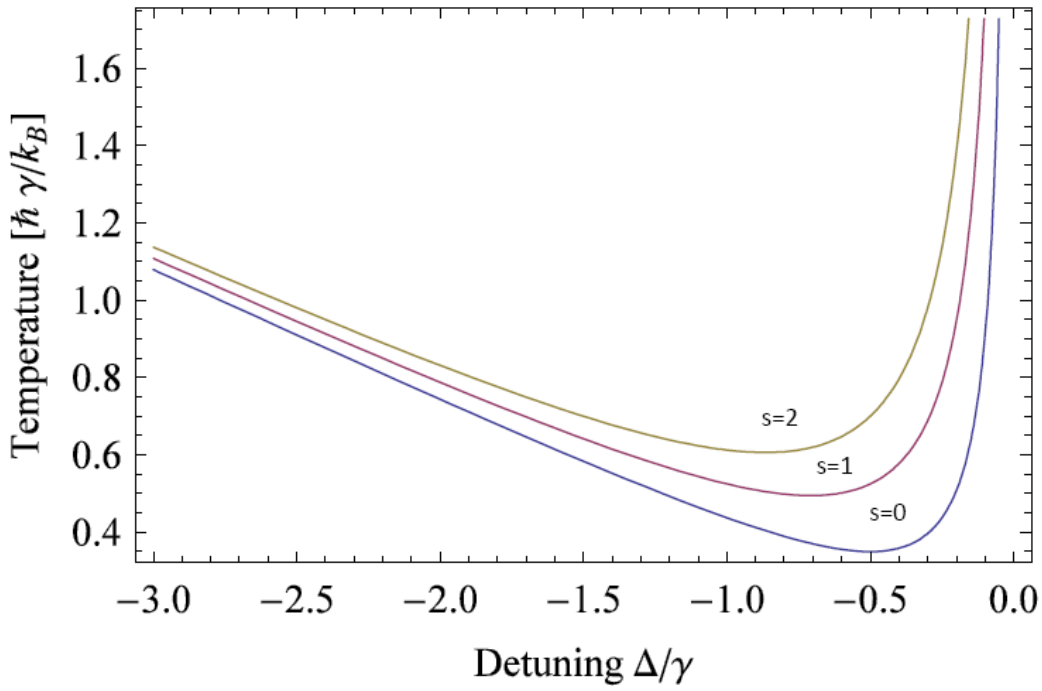

Fig. 8. Doppler cooling limit as a function of detuning of the cooling laser.

For different saturation parameters, the minimum temperature is:

$$T_{\min} = \frac{\hbar\gamma\sqrt{1+s}}{4k_B}(1+\xi) > \frac{7\hbar\gamma}{20k_B}, \tag{2.44}$$

when the laser detuning is $\Delta = -\sqrt{1+s}\gamma/2$. For very small laser intensity (s~0), when the detuning is red detuned by half of the natural linewidth, the minimum temperature is $\frac{7\hbar\gamma}{20k_B}$. It's only depending on the transition linewidth. For the $^{24}Mg^{+}$ $3s_{1/2}$-$3p_{3/2}$ transition, which is used for the laser cooling in the experiments, the Doppler limited temperature is 0.72 mK (γ=41.5 MHz [9]).

2.2.2 Sympathetic cooling

To sympathetically cool the ions of interest with the laser cooled ions, different ion species need be trapped together in one trap with same parameters simultaneously. In this situation, it is necessary to determine where the stability regions of these ion species are overlapped and to choose the q or a value accordingly. This can be obtained by suitable trapping RF and DC offset. The lowest stability region of $^{24}Mg^{+}$ and $^{4}He^{+}$ is shown in Fig. 9.

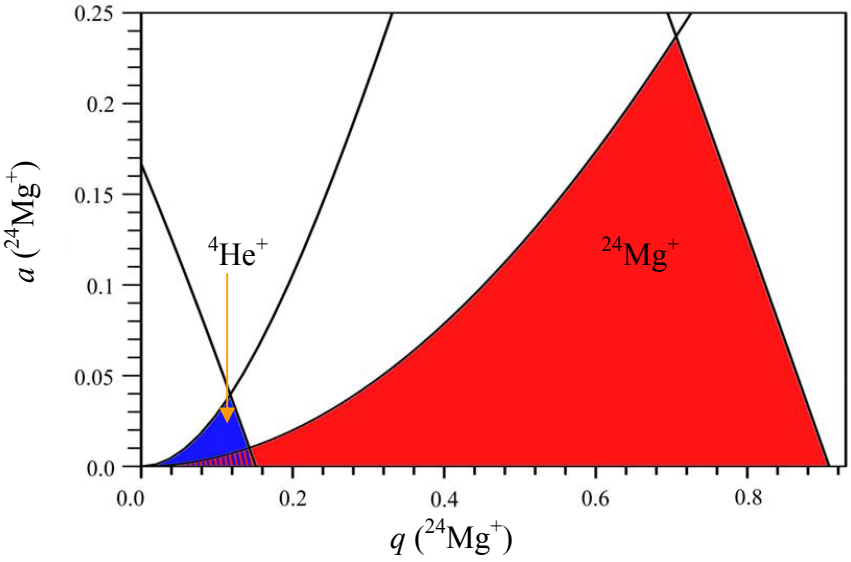

Fig. 9. Lowest stability region of $^{24}Mg^{+}$ and $^{4}He^{+}$.

When the ion clouds or crystals with different ion species reach equilibrium state, the ions rearrange themselves to such a way that the potential is flat at the bottom [27]. According to the Eq. (2.21), the trap depth is reverse to the mass for the singly charged ions. Thus the larger the mass is, the shallower the trap is, as Fig. 10 shows. Thus, in the equilibrium state, the ions with a single charge rearrange themselves so that the species

with the light mass species occupy the center region of the trap, while the species with the heavier mass surround them [38].

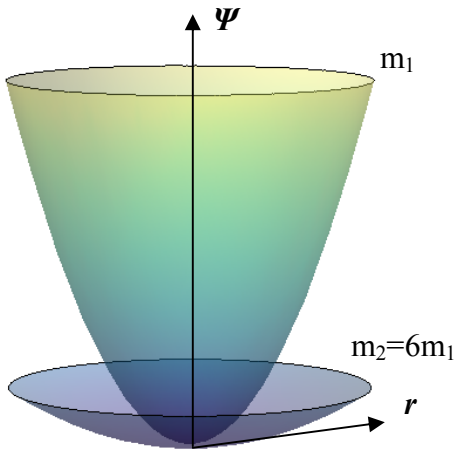

Fig. 10 Pseudo potential for different masses of singly charged ions.

For highly charged ions, there is also a radial separation of the species due to their different pseudo potential strength, which scales as e^2/m. Thus for equally charged ions, the total potential will be minimum if the lighter ions occupy the center of the trap. For the arbitrary charge case, in the limit of cylindrical symmetry, the ratio of outer radius r_1 of the higher charge to mass ratio (e_1/m_1) specie and inner radius r_2 of the lower charge to mass ratio (e_2/m_2) specie is given by [39]:

$$\frac{r_1}{r_2} = \sqrt{\frac{e_2 m_1}{e_1 m_2}}. \tag{2.45}$$

The difference between the charge to mass ratios of the simultaneously trapped ion species is very important for the efficiency of the sympathetic cooling [40]. Generally speaking, the closer the charge to mass ratio is, the better the sympathetic

cooling performs. Also it is preferable that the laser cooled ions have a lower charge to mass ratio so that they could form a cage to the sympathetically cooled ions with a larger charge to mass ratio. It was found that this configuration is much easier to form the mixed ion crystals both experimentally and by simulations [41, 42, 43].

2.3 Research targets

2.3.1 Mg^+

Mg^+ ions have been studied in our TAMU trap for more than ten years. A Mg^+ ion has the electron configuration of $1s^2 2s^2 2p^6 3s^1$ for the ground state. It can be considered as one electron system which has simple electronic energy levels. Natural Magnesium consists of three isotopes, 79% ^{24}Mg, 10% ^{25}Mg and 11% ^{26}Mg. Because the nuclear spin of $^{24}Mg^+$ and $^{26}Mg^+$ is zero, they have no hyperfine structure. Thus with only one laser, they have cycling transitions which makes the cooling process efficient and detection convenient. The cooling transition used in the experiments is showed in Fig. 11.

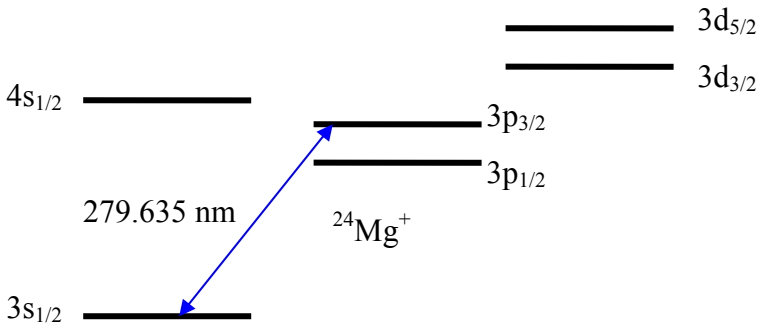

Fig. 11. $^{24}Mg^+$ cooling transition.

The $3s_{1/2}$-$3p_{3/2}$ transition with natural linewidth γ=41.5 MHz at 279.6nm is used as cooling transition. Compared with $3s_{1/2}$-$3p_{1/2}$ transition, this transition is stronger due to the higher degeneracy of the excited state. The energy separation between the $3p_{1/2}$ and $3p_{3/2}$ state is about 2744.6 GHz [44]. So these two transitions are well separated even considering the large Doppler broadening for the hot ions (3.8 GHz at 600 K).

It is shown in Fig. 8, for the temperature limit of the Doppler cooling, the saturation parameter is very important. The saturation intensity can be calculated by using $I_{sat} = 2\pi^2 c\hbar\gamma/(3\lambda^3)$, which is about 247 mW/cm^2 for the cooling transition. For a 100 μm spot size beam waist, about 20 μW UV beam reaches this saturation intensity.

In experiments, sometimes $^{26}Mg^+$ ions are also produced and identified, the isotope shift of the $3s_{1/2}$-$3p_{3/2}$ transition is about 3.088 GHz [44]. For $^{25}Mg^+$, because it has nuclear spin of I = 5/2, the transition splits to hyperfine structure. It makes additional beams necessary to establish a cycling transition and repump from the dark hyperfine levels. Thus it was not observed in the experiments with only one laser source.

2.3.2 $^4He^+$

Our laboratory is collaborating with the laser spectroscopy division of Prof. T. W. Hänsch at Max Planck Institute for Quantum Optics (MPQ, Garching, Germany) on the *1s-2s* two photon spectroscopy of $^4He^+$ [18]. The $^4He^+$ is a simple hydrogen-like system, its *1s-2s* two photon transition with a linewidth about 84 Hz is a good candidate for the experimental measurement and to test bound state quantum electro dynamics. It was reported that $^4He^+$ ions were sympathetically cooled with the $^9Be^+$ ions [41]. To study the sympathetic cooling of $^4He^+$ ions by the laser cooled $^{24}Mg^+$ ions, it gives more

information on the trapped and cooled $^{4}He^{+}$ ions for the MPQ-TAMU ongoing precision spectroscopy project.

2.3.3 H_2^+

H_2^+ is the simplest molecule and has played a similar role in molecular quantum mechanics as the hydrogen atom for atomic quantum mechanics. It was reported H_2^+ ions were sympathetically cooled with $^{9}Be^{+}$ ions [43]. Of course H_2^+ ions can also be trapped and cooled with the $^{24}Mg^{+}$ ions, but H_2^+ is created by electron bombardment on H_2, and Mg^+ ions have some photon assisted chemical reaction with H_2 [17, 45]. There is the question whether or not the H_2^+ can be sympathetically cooled and stored long enough to perform the proposed spectroscopy on hydrogen molecular ions in the high lying bound state ($2p\pi_u$). Our goal is to get the first hand information on that issue

2.3.4 Fullerene ions

Singly or highly charged fullerene ions can be sympathetically cooled by $^{24}Mg^{+}$ ions [22, 46]. And the previous result achieved is around ~14K for singly charged fullerene ions. It is interesting to study the sympathetic cooling on singly or highly charged fullerene ions with the $^{24}Mg^{+}$ ions to see the effect of the sympathetic cooling for the two species with large charge to mass difference.

CHAPTER III

APPARATUS

In this chapter, a detailed description of our ion trap system is provided. The discussion includes ion trap, RF electronics, vacuum system, ion creation, optics and ion detection device.

3.1 Ion trap

Our ion trap is a typical linear quadrupole RF ion trap. It consists of four identical cylindrical rods, which are split into three equal segments. The ion trap geometry is shown in Fig. 2. The diameter of the electrodes is 6.00 mm, the distance between each pair of opposite electrodes is 5.21 mm, and the length of each electrode segment is 50.0 mm. A macor sphere of diameter 1 mm is pressed into a machined notch at the ends of the adjacent segments to isolate them from each other. This facilitates to apply different dc voltages to different segments. Each pairs of opposite electrodes in all segments are coupled to the same RF voltage. The RF voltages applied to these two pairs have opposite phase. This provides the radial confinement of the trapped ions.

At one end of trap, a C_{60} oven bias voltage serves as the endcap DC voltage. At the other end, a closing dish is used to confine the ions in the trap. Also in the experiments, the side segments DC voltage could be used to keep the ions in the center segment of the trap. However, since the center section is 50 mm long, the axial confinement is quite weak if only the side segments are used as the endcap. For a tighter

axial confinement, two rings made by 1 mm diameter tantalum wire were arranged around the electrodes of the center segment, as Fig. 12 shows. The space between two rings is 16 mm, the diameter of the ring circle is about 20 mm.

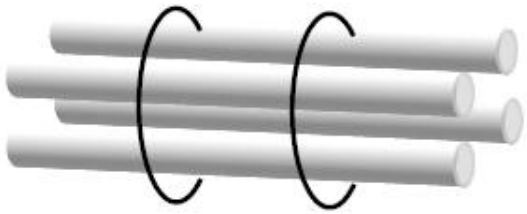

Fig. 12. Diagram of two rings around the center segment of the ion trap.

There are two C_{60} ovens and two Mg ovens mounted around the two side segments. Also there are three electron guns mounted according to the ovens to facilitate the electron bombardment ionization.

3.2 RF electronics

In order to trap ions, especially the heavy molecular ions like C_{60}^{+}, high RF trapping voltage of a few thousand volts has to be applied to the electrodes.

The RF signal is generated by a function generator (Stanford Research Systems, DS 345), amplified by a RF power amplifier (Electronic Navigation Industries, 240L), coupled to the trap LC resonant circuit, or tank circuit, as shows in Fig. 13.

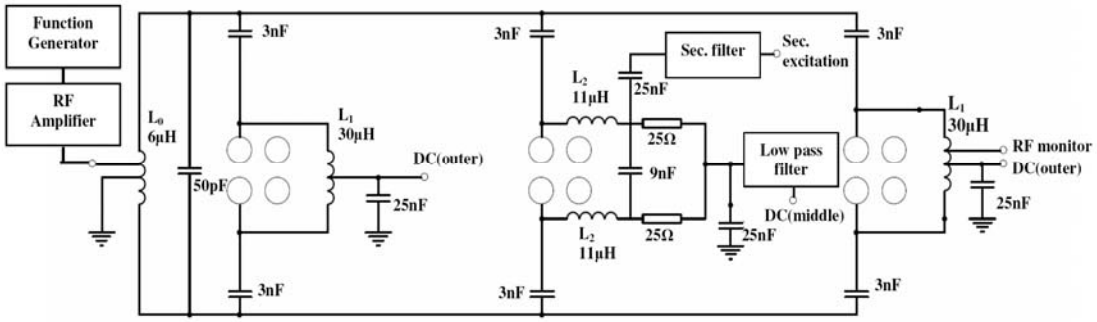

Fig. 13. Schematic diagram of the tank circuit.

It should be pointed out that in Fig. 13, the electrodes on diagonal positions are actually connected. The major part the circuit is the LC circuit with a resonance frequency of 7.48 MHz (It changes slightly after baking the vacuum system.). The 3 nF capacitors are used to isolate the DC offset to the electrodes. On side segments, two L1 coils are connected to the electrodes to minimize the disturbance of DC to RF. In one of them, a point of L1 is used to monitor the RF on the electrodes. On the center segment, 9 nF capacitor is used to isolate the additional DC and AC to the center segment. The DC is used to add the DC offset to the center segment, the AC is used to feed in the secular scan excitation voltage.

3.3 Vacuum system

Trapped ions are very sensitive to the collisions and chemical reactions with other atoms or molecules. In section 2.1.4, the calculated ion density in the trap corresponds to a pressure about 10^{-7} mbar, which means a better vacuum environment is

needed for the ion trap experiments. Therefore ultra high vacuum (UHV), which is a pressure below 10^{-7} Pa or 10^{-9} mbar, is critical for the ion trap experiments. Fig. 14 shows schematically the components of the vacuum system.

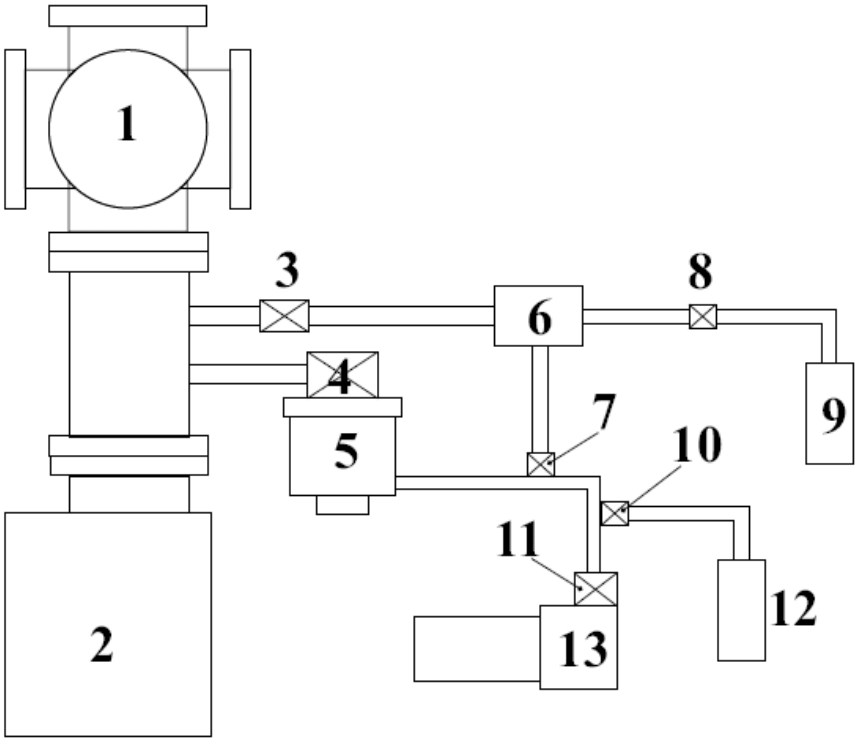

Fig. 14. Diagram of the vacuum system. 1: Six port stainless steel chamber; 2: VacIon pump; 3: High precision leak valve; 4: All metal valve; 5: Turbo molecular pump ; 6: Gas reservoir (H_2); 7: Gas reservoir evacuation valve; 8: gas reservoir fill valve; 9: Gas bottle (H_2); 10: Needle valve used to leak Helium gas into the foreline; 11: Foreline pump shutoff valve; 12: Helium bottle; 13: Foreline dry scroll pump.

The ion trap is mounted on an eight inch flange and placed in a six port stainless steel chamber. This chamber is sitting on a two port extension, which is placed on a Varian VacIon pump with a pumping speed of 140 l/s. On the side of the two port extension chamber, there is a metal valve to connect a Leybold-Heraeus turbo molecular

pump with a pumping speed of 145 l/s. A Varian dry scroll pump is used as the fore line pump. Its pumping speed is about 1.9 l/s. The fore line pressure is monitored with a thermocouple gauge. The pressure in the experiment chamber is monitored with a hot cathode ion gauge.

The general pumping procedure works as follow. The dry scroll pump is used to roughly pump the system. When the pressure reaches about 10^{-2} torr range, the turbo molecular pump is switched on. For a relatively clean chamber, the pressure could reach 10^{-7} mbar range in two days. To achieve the UHV, it is necessary to bake the vacuum system to 200ºC and keep it at this temperature for several days. Controlled by the transformers, heating clamps are connected with many flanges and heating bands are wound around the chambers and VacIon pump. The whole system is covered with Aluminum foil to reduce the temperature gradients. Also temperature sensors, such as thermocouples, are attached to sensible points to monitor the temperature. During the baking, the heating voltages are slowly increased, and the system is gradually heated up at a rate of 10~15 ºC/hr to avoid cracking the glass and quartz windows. After heating up, the pressure could rise to 10^{-5} mbar. Continuing pumping a few days at 200 ºC, the pressure drops about to 10^{-7} mbar as the water and other substances are baked out of the vacuum system, in the mean time VacIon pump should be switched on to further lower the pressure to 10^{-8} mbar. After that, the system is gradually cooled at a rate of 10~15 ºC/hr, and eventually the pressure drops to 10^{-10} mbar range. Sometimes after baking, it is necessary to tighten the screws to get a lower pressure because the heat stress can cause some small leaks.

A pressure about 2.0×10^{-10} mbar is the limit of the current vacuum system. After the bake out procedure, the residual gas consists of mostly molecular hydrogen, which is not pumped effectively by the turbo molecular pump or VacIon pump. With the help of a titanium sublimation pump, which absorbs the molecular hydrogen quite effectively, a pressure in the order of 10^{-11} mbar is expected [47].

3.4 Ion creation

Two ion creation methods are used in the experiments, electron bombardment and photoionization. Generally, electron bombardment is a simple way of producing ions. As long as the electron energy is larger than the ionization energy, any neutral atoms or molecules can be ionized by bombardment. But there are several disadvantages: first, it needs a good alignment of electron gun and the atom oven, if the electron beam and neutral atom beam are not overlapped well, the efficiency of this method is low. Second, after the successful bombardment, the ions gain a lot of kinetic energy, the hot ions are not easily to be trapped and cooled down. Helium buffer gas was used in the experiments to improve the Mg^+ trapping efficiency before. This causes the third drawback, the lack of selectivity, since the Helium atoms were also ionized to He^+, and He^+ ions were trapped together with Mg^+ ions. Fourth, not only the isotopes can be ionized, but also some Mg^{2+} can be created by the bombardment. These unwanted ions pollute the ion crystals. Last but not least, static charges are accumulated in the insulated surfaces during the electron bombardment processes and these electric potentials caused by the static charges will disturb the trapped ions.

Comparably the second method namely photoionization is much more efficient and selective than electron bombardment. It also avoids the build up of static charges. For these reasons, laser systems were developed to photoionize the neutral Mg atom and use photoionization whenever possible.

3.4.1 Ovens and electron guns

There are four ovens around the trap, two filled with Mg wire (Goodfellow, 0.5mm diameter, 99.9+%), two filled with C_{60} powder (BuckyUSA, 99.9%). The information for the ovens is provided in Table I. There are three electron guns mounted according to the trap to facilitate the electron bombardment ionization. The operating current for electron guns is 2.1 A.

Table I. Oven information.

Oven materail	Nickel tube	Tantalum tube
Oven loading	fullerene	Magnesium
Oven diameter [mm]	1.5	1
Oven length [mm]	8-10	10
Operating current [A]	1.2	1.2

After the baking, it is important to degas the ovens and electron guns slowly, because there are some tiny gas bubbles trapped in the oven structure. Slowly increasing the currents which run through the ovens and electrons, the pressure could rise from 10^{-10} mbar range to 10^{-7} mbar range. It takes about several hours to degas all the ovens and electron guns to the working currents.

For the Mg oven, it is very helpful to clean the Mg wire and treat it with citric acid (4 gram in 100 ml water) before it is loaded into the oven. When the Mg is in the air, it is covered with an oxide layer. The MgO has a much higher melting point (~ 3125 K) than the pure Mg (~ 923 K). Therefore, it might happen for the non-treated wire that the inside Mg is melting while the outside shell of MgO still holds. At some point, the MgO shell breaks and the whole oven explodes. By putting the wire into the citric acid, the gray MgO is replaced by the white Magnesium citrate, which has a much lower melting point than the Mg, and easily to be removed in the vacuum by degassing the oven at low current about 1.0~1.1 A for several hours.

3.4.2 Photoionization of Mg

The ionization energy of Mg is 7.65 eV. Initially, the electron bombardment method was used to create Mg^+. With the development of the laser system, photoionzation of Mg is used in all current experiments.

Neutral Mg atoms can be ionized by the resonance enhanced two photon ionization [48]. As Fig. 15 shows, the first step is that the UV laser at 285nm excites the transition from the $3s^2$ ground state to the *3s3p* state. In the second step, when the Mg atom is at the *3s3p* state, any absorption of another 285 nm photon from the photoionization beam or a 280 nm photon from cooling beam will lead the Mg atom to ionization. The natural linewidth of $3s^2$ to *3s3p* the transition is about 78.2 MHz, the average lifetime of Mg atom at *3s3p* state is about 13 ns, therefore this resonance enhanced two photon ionization works quite effectively.

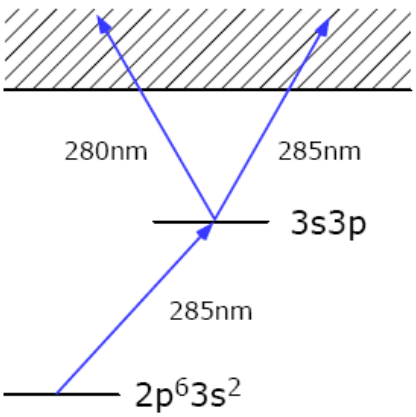

Fig. 15. Resonance enhanced two photon ionization of Mg atom.

In the Table II, the isotope shift of the first step transition is listed.

Table II. Isotope shift of the $3s^2$ to $3s3p$ transition in Mg atom [49].

Isotopes	Abundance	Absolute frequency (cm^{-1})	Relative shift to ^{24}Mg (MHz)
^{24}Mg	78.99%	35051.273	-
^{25}Mg	10.00%	35051.298	744
^{26}Mg	11.01%	35051.320	1413

It looks like the natural linewidth of this transition (~80MHz) is much narrower than the isotope shfit (~750MHz). But in the trap, the Mg atom beam is not perpendicular to the photoionization laser, the large Doppler broadening (~3.8GHz at 600K) causes the overlap of this first step transition used for photoionization for the different isotopes. However, the photoionization is still partially isotope selective if the laser is detuned far above the transition of $^{26}Mg^+$, or far below the transition of $^{24}Mg^+$.

3.4.3 Electron bombardment

Because there are either no suitable transitions or no available lasers, many atoms or molecules have to be ionized by electron bombardment.

The ovens loaded with fullerene could be heated by the operating current at 1.2 A. The thermally evaporated neutral molecular beam is bombarded by the electron beam generated by electron gun in the trap area. Thus fullerene ions can be created in the trap. In the ion creation process, it is helpful to leak about 10^{-7} mbar He buffer gas in the chamber. This will effectively reduce the velocities of the fullerene molecules or ions, and increase the production of the fullerene ions [50]. Also because of the huge mass difference between the fullerene ions and $^4He^+$ ions, the high RF voltage, which is necessary to trap the heavy fullerene ions, is not corresponding to a stable q value for the $^4He^+$ ions. Therefore practically all the $^4He^+$ ions do not stay in the trap.

For He, it is leaked into the chamber through a leak valve between the turbo molecular pump and fore line pump, then the electron gun is turned on to create He^+ in the trap. Because the turbo molecular pump has a lower pumping rate for Helium than for heavier molecules. Thus leaking He into the fore line side makes sure that only very pure He is introduced into the working chamber with turbo molecular pump acting in this way as a purifying filter.

For H_2, it is leaked into the chamber through a precision leak valve to the working chamber. Because the vacuum system is not pumping H_2 effectively, great care must be taken to minimize the leaking flow.

3.5 Optics

The optics set up for the ion trap experiments is shown in Fig. 16. The detailed description includes the lasers, second harmonic generation cavity (SHG cavity), iodine saturation spectroscopy, and imaging system.

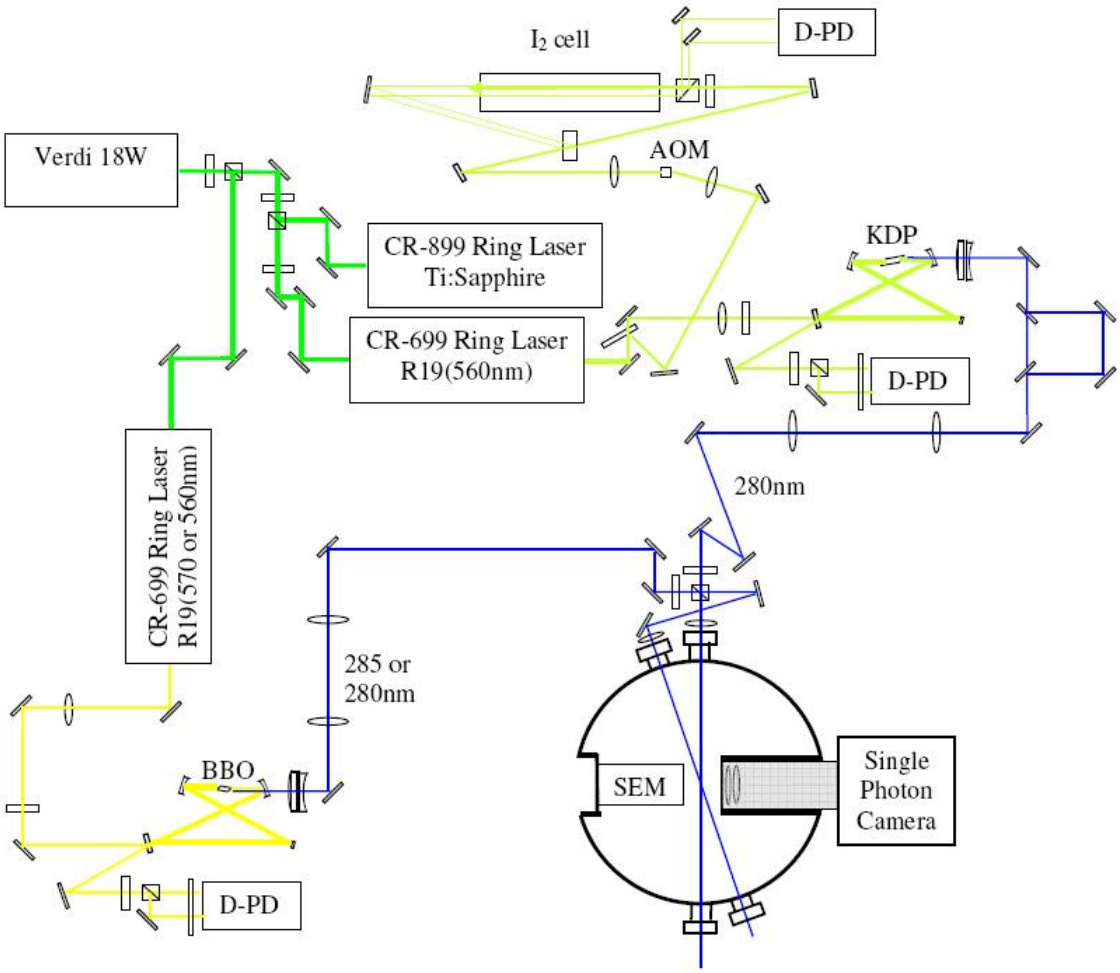

Fig. 16. Optics overview.

3.5.1 Lasers

A diode pumped solid state laser (Coherent, 18W Verdi) serves as the pump laser. The output power is up to 18W, the wavelength is 532nm. The performance of this 18W Verdi is much better than the Ar ion laser (Coherent, Innova 200) used in the ealier experiments. Three half wave plates and two polarized beam splitter (PBS) cubes are used to divide the output of 18W Verdi to pump three CW lasers, two dye lasers (Coherent, CR 699-21) and a Ti:sapphire laser (Coherent, CR 899). The wavelength of the output of one dye laser is 560 nm, it is frequency doubled to generate a 280nm UV beam to cool the Mg^+. The other wavelength is 570 nm, it is frequency doubled to generate a 285nm UV beam to photoionize Mg atom. The Ti:sapphire laser is not used in the present setup.

The CR 699-21 dye laser comprises a single frequency, tunable, traveling wave ring dye laser capable of locked scan operation across a 30 GHz range. The output is stabilized by locking the dye laser cavity to a built-in reference cavity. The actual linewidth is about 3.5 MHz as derived from the fluctuation of the locking signal from the reference cavity using the formula provided in the laser manual.

Rhodamine 19 dye is used with ethylene glycol as the solvent. Usually it gives a spectrum from 562 nm to 602 nm with the peak at about 575nm, which does not quite reach the cooling transition of 560 nm. The emitting spectrum can however be blue shifted to a spectrum range from 555 nm to 580 nm by adding potassium hydroxide, it also increase the power at 570 nm. In some experiments, two 560 nm wavelengths are need. Thus both dye lasers are using the same recipe for the dye preparation.

The dye solution is prepared as follow: first, 1.0 g Rhodamine 19 is stirr into 250 ml benzyl alcohol, the container is put into warm ultrasonic bath to completely dissolve Rhodamine 19. Then the dye mixture is added into 1.75 l ethylene glycol. Also 2.0 g KOH is dissolved into 80 ml methanol and put into the dye solution. The volume of the dye reservoirs of the two dye lasers are different, accordingly the dye solution is prepared proportionally.

The nozzles of the two dye lasers are different, therefore the output powers of the two dye lasers are different. Usually the cooling laser, whose output is 560 nm, pumped by 5.0 W at jet pressure 65 psi, gives about 300 mW for fresh dye solution. The photoionization laser, whose output is 570 nm, pumped by 6.0 W at jet pressure 80 psi, gives about 250mW for fresh dye solution. The fresh dye solution lasts about four months under typical conditions.

3.5.2 Iodine saturation spectroscopy

Iodine molecule I_2 has many absorption lines that span over the major part of the visible spectrum, each of these lines is in fact a group of narrowly spaced hyperfine absorption lines with natural linewidth about a few MHz [51]. Due to the Doppler broadening, groups of these lines are merged together. To observe these hyperfine lines, saturation spectroscopy was used, and with some frequency modulation methods, the saturation spectroscopy is employed to lock the laser [52]. The experimental setup for the iodine saturation spectroscopy is shown in Fig. 17.

A small portion of dye laser output about 7~8 mW is used for the setup. A beam splitter picks out two similar week beams, one is the probe beam, the other is the

reference beam. While the remaining strong pump beam passes through a half wave plate and PBS, and overlaps with the weak probe beam in the Iodine cell. Because the strong pump beam saturates the Iodine molecules in its path, there is a small difference of the transmission between the probe beam and the reference beam. The intensity difference of these two beams is measured with a differential photo detector. To improve the signal to noise ratio, a chopper is used to modulate the pump beam intensity. Therefore the saturation effect of the probe beam is periodically modulated. A lockin amplifier can easily pick up the saturation signal and greatly improve the saturation spectroscopy.

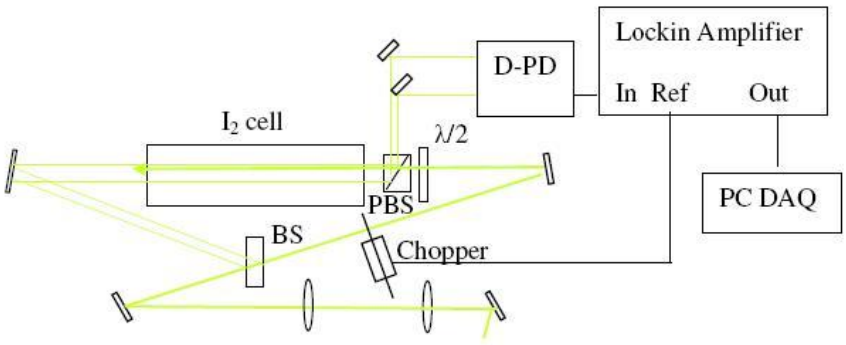

Fig. 17. Diagram of the iodine saturation spectroscopy.

Fig. 18 shows the absorption spectrum of iodine in the frequency range used to cool $^{24}Mg^{+}$ ions. The frequencies of the iodine absorption lines are calculated based on the iodine atlas [53]. The red line is where the transition of $^{24}Mg^{+}$ used in the experiments. Therefore, by simultaneously recording the iodine saturation spectroscopy and $^{24}Mg^{+}$ cooling spectroscopy, an accurate cooling transition of $^{24}Mg^{+}$ is measured.

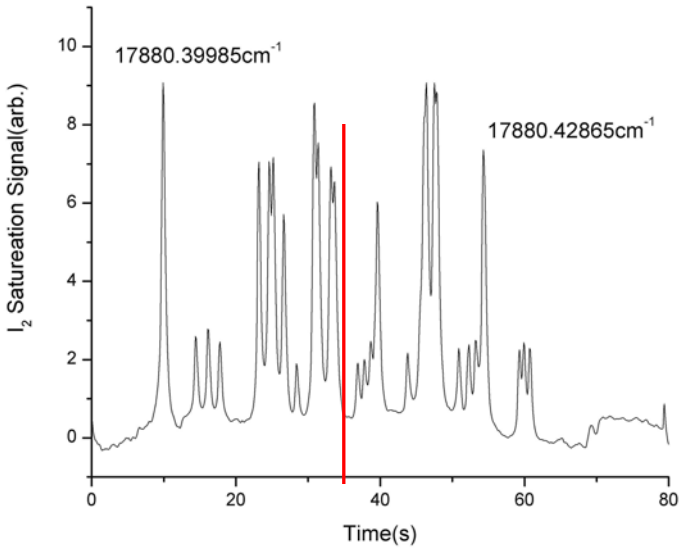

Fig. 18. Saturation spectrum of iodine.

For several experiments on ion crystals, it is necessary to lock the cooling laser for the $^{24}Mg^{+}$. This is achieved by locking the dye laser output to a suitable iodine line with frequency modulation by an acousto-optic modulator (AOM, Brimrose, TEF-800-500).

The modified experimental setup to lock the dye laser on the iodine line is showed in Fig. 19. A small portion of dye laser output is focused on the AOM, the first order of the diffraction beams is used to the saturation spectroscopy. The AOM driver produces the frequency modulation on the AOM, in turn the first order diffraction beam is shifted in frequency and frequency modulated compared with the zero order beam. The frequency modulation not only facilitates the use of lock-in amplifier to improve the

signal to noise ratio, but also the signal of the lock-in amplifier now is the derivative of the saturation signal, which is more like a dispersion signal. It is showed in Fig. 20.

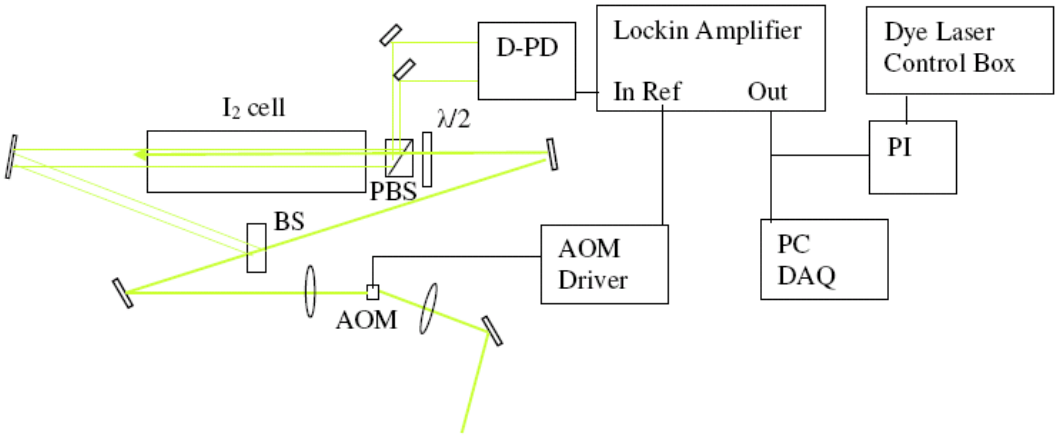

Fig. 19. Diagram of iodine lock system.

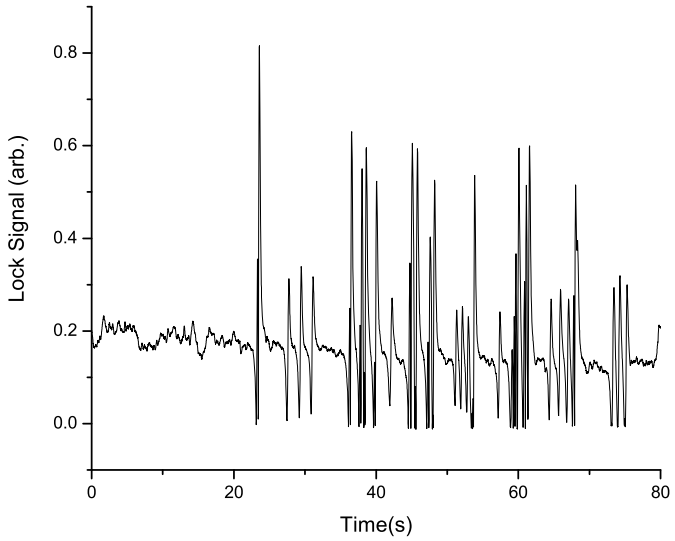

Fig. 20. Iodine lock signal.

This dispersion signal is called error signal, it is sent to proportional integral (PI) controller, and used to lock the dye laser to prevent the frequency drift. A dye laser lock result is showed in Fig. 21.

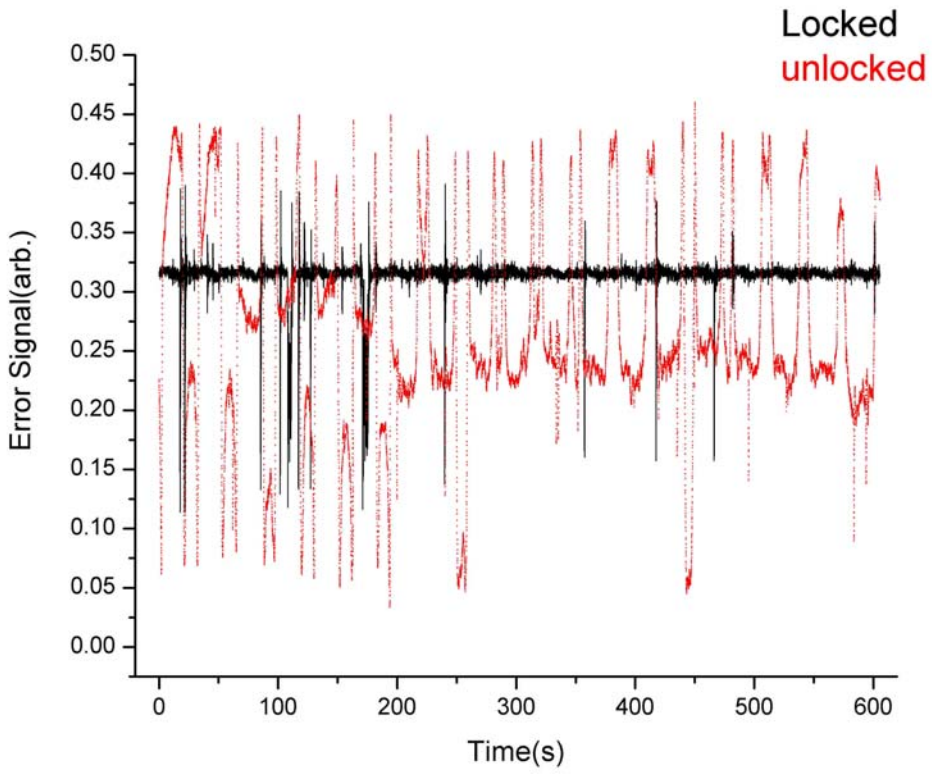

Fig. 21. The error signal of dye laser locked to one iodine absorption line.

Error signals generated by dye laser were recorded. The red lines were the signals without lock. On the locked black line, there were still some frequency jitters. They have a variety of causes, such as the dye bubbles, acoustic noise, mechanic vibrations, etc.

3.5.3 The second harmonic generation cavity

In order to convert the laser wavelength from 560 (570) nm to 280 (285) nm, two second harmonic generation cavities were built. Both cavities are mounted on an optical breadboard and put into an acoustically isolating wooden box to reduce environmental disturbances. As shown in Fig. 22, both cavities are bow-tie cavities stabilized by using the Hänsch-Couillaud method [54].

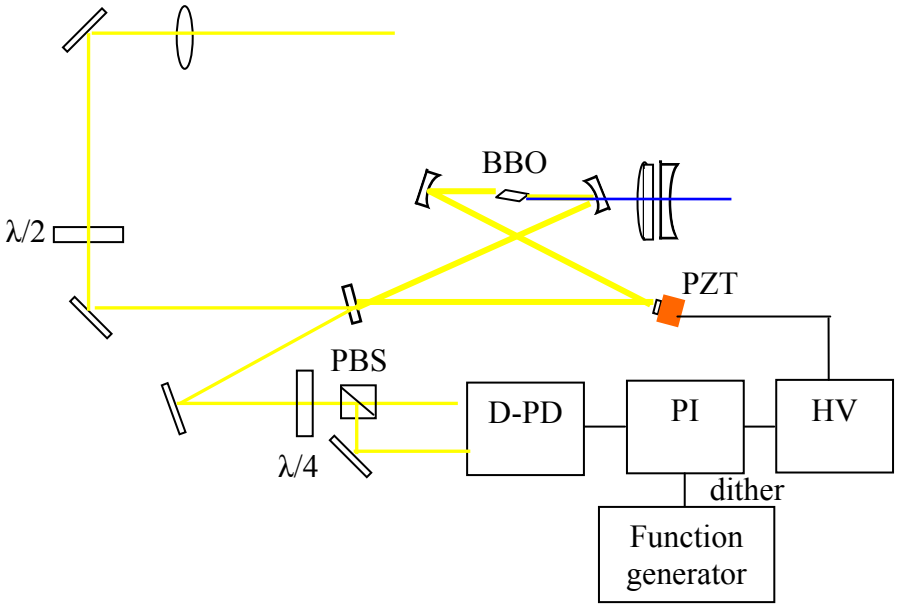

Fig. 22. Diagram of one SHG cavity.

The cavity consists of four mirrors and a non-linear crystal. With the mode matching lens and two mirrors, the output of the dye laser is coupled into the cavity. A half wave plate outside the cavity is used to change the linear polarization of the incident fundamental laser. The beam reflected from input coupler interferes with the transmitted beam from the light inside the cavity. A quarter wave plate and a linear PBS cube

decompose the elliptical polarization of the beam. The intensity difference of the decomposed linear polarized two light beams is monitored by the differential photo diode. With proper optical alignment, scanning the length of the cavity by driving the piezo transducer (PZT) with triangle voltages gives the dispersion signal, as shown in Fig. 23. The dispersion signal is sent to the PI controller to control the PZT and lock the cavity length to obtain an increase of the injected laser power by constructive superposition within the resonator.

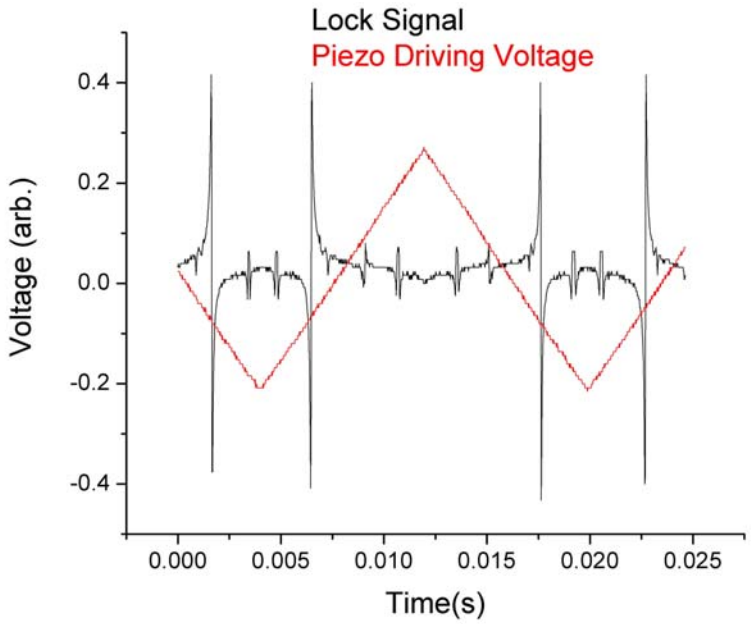

Fig. 23. Lock signal for the SHG cavity.

Two kinds of nonlinear crystals are placed in the similar cavities. One is a 10 mm long barium borate (BBO) crystal, the other is a 20 mm long potassium dihydrogen phosphate (KDP) crystal. The BBO crystal is sitting on a heated crystal holder to prevent condensation by moisture, while the KDP crystal is placed in a small chamber with

desiccants. Phase matching is achieved by angle phase matching for both crystals, therefore the output second harmonic UV is elliptical. A telescope consisting of two cylindrical lenses is used to shape the UV beam to a circular beam profile.

The working parameters of both cavities are given in the Table III.

Table III. Parameters of both SHG cavities [55].

Nonlinear Crystal	BBO	KDP
Fundamental wavelength(nm)	570 or 560	560
Crystal Length(mm)	10	20
SHG type	ooe	ooe
Walkoff(mrad)	0 0 84.55	0 0 21.80
At theat (degree)	44.4	67.9
d_{eff} (pm/V)	1.82	0.434
Curved Mirror ROC (mm)	50	150
Waist in crystal (μm)	20	54
Raleigh region (mm)	4.4	26
Other waist (μm)	186	246
Reflectivity of input Coupler	97.0%	97.7%
Typical input power (mW)	150	120
Typical output power (mW)	1.2	1.0
Enhancement factor	33	29

3.5.4 Imaging system

The most usual method to detect the trapped ions is to measure the laser induced fluorescence emitted by the ions. In the laser cooling process, the emission process is isotropic. That means the fluorescence emits in all direction equally. Because there is always a limitation on the observation angle, windows, etc, the imaging system should collect the photons efficiently with high signal to noise ratio. In many cases, the imaging system is required to resolve the single ions.

To clean up UV beam, two cylindrical lenses shape the UV beam profile, the UV beams pass through a telescope spatial filter. The intensity of the UV beams are adjusted by a half wave plate and a PBS cube, then focused into the chamber by a lenses with 50 cm focal length in the collinear direction and by a lens with 30 cm focal length with a 15° degree inclination with respect to the trap axis. The spot size is about 100 μm for the collinear beam and 80 μm for the cross beam at the trap center.

The imaging system developed in our ion trap system includes one or two lens, and an image device, either a single photon camera or an electron multiplied charged couple device (CCD) camera. The one lens configuration is shown in Fig. 16. Depending on the imaging requirement, magnification coefficient could vary from 6 to 48, and single ions are resolved with the imaging system.

The two lenses, which could be used in the image system, are both UV condensers (Melles Griot, 01-CMP-115) with the focal length of 35mm. The first condenser is placed outside the chamber, which gives some freedom to adjust the lens position to achieve a good focus. This condenser is very close to the reentrance window

and the distance between the trap axis and the objective principle plane of the condenser is approximately 41 mm, which gives a magnification about 6. This is sufficient to resolve single ions in most of current experimental setup. Many ion crystal images were taken in this configuration and are depicted in the next chapter. While in some cases, a larger magnification is needed, a same type of UV condenser is placed between the first condenser and the camera, it is mounted on a three dimensional translational stage, an aperture is place in the objective plane of the second condenser to reduce the stray light from the image of the first condenser. Because of the limited space, the largest magnification of the second condenser is around 8. Thus totally the largest magnification of the two condensers system is about 48.

Two cameras are used in the image system. One is a Quantar 2601B single photon camera. The other is an electron multiplied CCD (EMCCD) camera (Andor DV-885K).Both of them have advantages and disadvantages. Generally speaking, for the small ion crystals, the single photon camera works better. While for large number ion crystals, the EMCCD camera works better.

The imaging sensor head of the Quantar 2601B single photon camera is a microchannel-plate (MCP) type, XY position-sensitive photomultiplier imager. In operation, single incoming photons are incident on the photocathode, producing photoelectrons. Under the influence of a strong electric field, these photoelectrons impact multi-stage MCP electron multiplier spaced closely to the photocathode. The position of each incoming photon is thereby replicated, photon by photon, on the MCP surface. By readout electronics, the special position is recovered. The sensor surface is

circular with a diameter of 25mm and has a spatial resolution of about 55 μm. The output is digitized with a resolution of 512×512 pixels, which corresponds to a pixel size of about 49 μm. The MCP imager produces the images in real time by observing the impact of the photons incident on the photocathode on the screen of the oscilloscope, which is really helpful during the optical alignment of the traps. The quantum efficiency of the photocathode at 280 nm is about 25%. This signal to detector noise ratio is extremely high, often statistically averaging 10,000:1 or more for a single detected photon in a pixel. However the maximum photon count rate is 65 kHz. In experiments, a dozen of $^{24}Mg^{+}$ ions could already saturate the camera and trigger the protection shutter, which makes this camera rather hard to work with large number ion crystals.

The Andor EMCCD chip has about one mega pixel resolution. Each pixel is about 8×8 μm size. The quantum efficiency at 280 nm is about 28%. A big disadvantage of the EMCCD camera is the relatively long acquisition time, which makes the aligning hard. Also there is always readout noise for the CCD camera, which decreases the signal to detector noise ratio. But the CCD camera has a vast dynamic range. It can be used to image huge ion clouds consisting of millions of ions.

The photon detection efficiency of the image system can be estimated based on two factors, the effective solid angle of the ion crystal exposed to the camera; and quantum efficiency of the camera. For the solid angle, in horizontal direction, the size of the condenser limits the observation angle. Vertically, it is limited by the spacing between two adjacent trap electrodes. Taking all dimensions into account, the solid angle

is about 2%, and the quantum efficiency is about 20% for the cameras. Thus, up to about 4×10^{-3} of the emitted photons are detected.

3.6 Destructive ion detection

Besides the optical detection method, a secondary electron multiplier (SEM, Balzers, SEV 217) is installed in the chamber to detect the ions ejected from the ion trap, as shown in Fig. 16. Although it is a destructive detection method, it is useful and provides information concerning mass analysis of the trapped ions. When the ions hit the conversion dynode of the SEM, secondary electrons are created and then accelerated to the second dynode to create more secondary electrons. The total amplification is about $\times10^{8}$ after passing through 17 dynode stage.

3.6.1 Qscan

Qscan is a simple detection scheme to obtain mass spectra with low resolution of all the trapped ion species. The idea of Qscan is straightforward. The trapping potential is decreased to zero, and the trap depth is shallower and shallower. And eventually all the ions are ejected out of the trap, part of the ions are detected by the SEM. The detection efficiency is estimated to be about 15% [21].

When multiple ion species are simultaneously trapped, the stability regions must overlap. The Fig. 24 shows the U and V stability diagram for different masses. Assuming the DC voltage U remains the same, which is the horizontal straight line, and the RF voltage V decreases. When the U line crosses the stability region of a particular ion species, the motions of ions become unstable, and are ejected from the trap. It is

obvious that the heavier ion species are always ejected from the trap first when the RF trapping potential is decreasing.

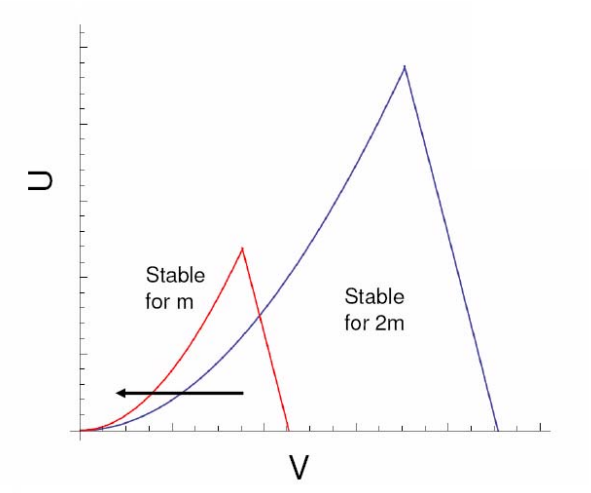

Fig. 24. Qscan diagram.

Fig. 25 is an example of ion counts during a Qscan of laser cooled Mg^+ ions and sympathetically cooled $^4He^+$ ions.

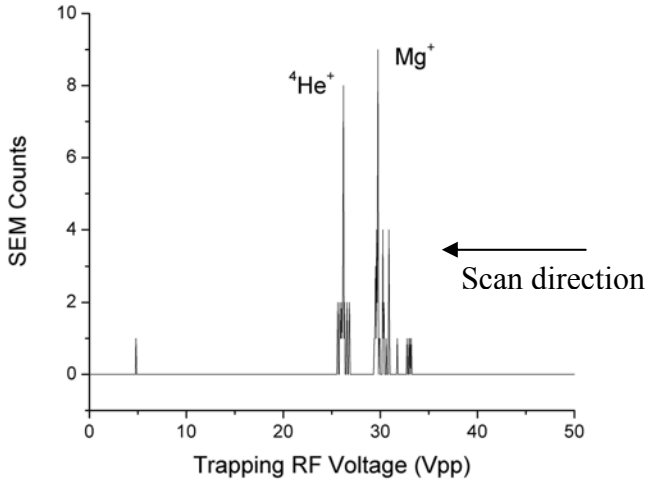

Fig. 25. Qscan of laser cooled Mg^+ and sympathetically cooled $^4He^+$.

If the ions are not cooled, they have different kinetic energies. With the trap potential decreasing, the ions with higher velocities fly out the trap first, then the ions with lower velocities. Fig. 26 shows the Qscan of $^4He^+$ ions, which were not cooled.

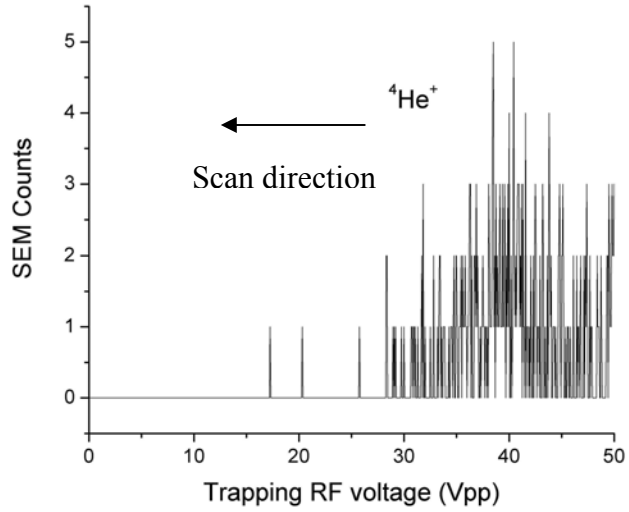

Fig. 26. Qscan of $^4He^+$ without cooling.

3.6.2 Secular scan

The secular scan is one way to get the mass spectra with high resolution. It can be used for the identification of trapped ion species, or for the characterization and calibration of the ion trap.

As discussed in section 2.2.1, in radial direction, the trapped ions have micro motion and secular motion. To obtain the mass spectrum with a secular scan, an excitation AC voltage is applied to the electrodes, and the frequency of the excitation voltage is scanned in time. When the scanning frequency coincides with the secular frequency of the particular ion specie, the ions, which have resonance with the excitation

voltage, are ejected from the trap provided the scanning secular amplitude is large enough. The detection efficiency of a secular scan is estimated to be about 1% [21].

Fig. 27 is an example of a secular scan.

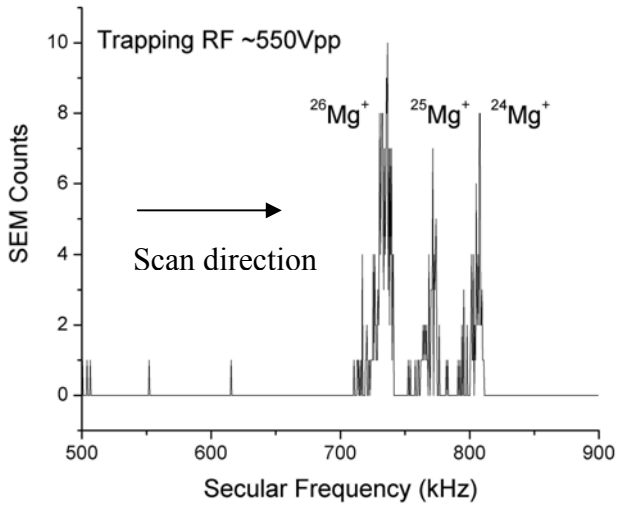

Fig. 27. Secular scan example.

It clearly resolves the three Mg^+ isotopes, present in the trapped ion cloud. The secular scan is an important tool in ion trap. It can be used to characterize trapping RF voltage if the trapped ion specie is known or it can be used to identify the trapped ion species if the trapping voltage is known. It can be used to purify the trapped ions by setting to the particular secular motion frequency of the unwanted ion species. Also it can be used to reduce trapped ions. With optical detection, it can be used to identify the ion species without destruction of the trapped ions. This will be discussed in Chapter IV.

CHAPTER IV

EXPERIMENTAL RESULTS

In this chapter a detailed description of the experimental results is provided. The discussion includes ion cooling spectroscopy, ion crystal images and sympathetic cooling.

4.1 Ion cooling spectroscopy

In 1987, the laser physics division of Prof. H. Walther at MPQ first discovered the phase transition between a cloud and a crystal state of trapped ions by the ion cooling spectroscopy [7]. In the early stage of the experiments, the ion cooling spectroscopy was used to study the laser cooling and sympathetic cooling [21, 22]. The cooling UV beam was scanned from the red to the blue over the cooling transition, in the mean time the counts of the fluorescence emitted by the ions were recorded by a PMT. The typical spectrum is shown in Fig. 28.

Since the ions are continuously cooled when the laser is red detuned to the transition, at some point below a certain temperature, the potential energy of the trap together with the mutual Coulomb repulsion of the ions dominates over the kinetic energy. At his point, the ions will arrange themselves into a regular structure, form the Coulomb crystal or Wigner crystal. The ratio of Coulomb energy of neighboring ions to their kinetic energy was introduced to characterize this behavior [56],

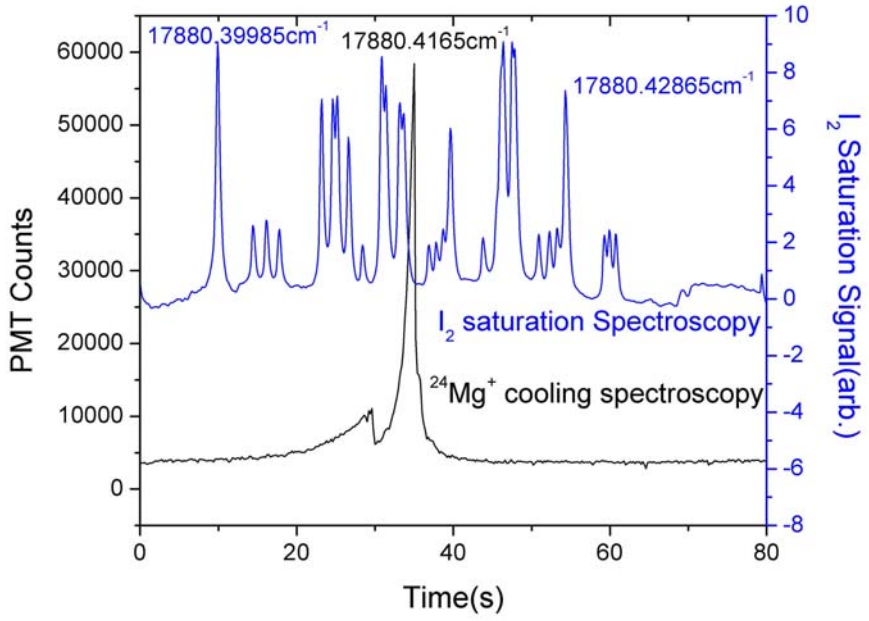

Fig. 28. Ion cooling spectroscopy and iodine saturation spectroscopy.

$$\Gamma_c = \frac{e^2}{4\pi\varepsilon_0 a_{ws} k_b T}, \tag{5.1}$$

where a_{ws} is the radius of the primitive unit cell characterized by $(4\pi/3)na_{ws}^3 = 1$, and n is the ion density. If the Coulomb energy of neighboring ions is smaller than the kinetic energy, the ions can change positions, this is the cloud state. If the Coulomb energy is much larger than the kinetic energy, the ions can not change positions. With the influence of the trap potential, the ions take a certain positions relative to their neighbors and form an ion crystal. When the laser scanning passes the center of the transition, red detuned laser cooling becomes blue detuned laser heating and the ion crystal melts quickly and some ions gain enough kinetic energy to leave the trap.

In Fig. 29, the two colored lines with a Voigt shape are fitted in the cooling spectroscopy before the phase transition and after the phase transition, the HWHM is about 500MHz for the cloud state and 50MHz for the crystal state. The temperatures can roughly be estimated with the Doppler width calculated from the Voigt line shape [22]. For the cloud state, the temperature is about 12 K, for the crystal state, the temperature is about 40 mK.

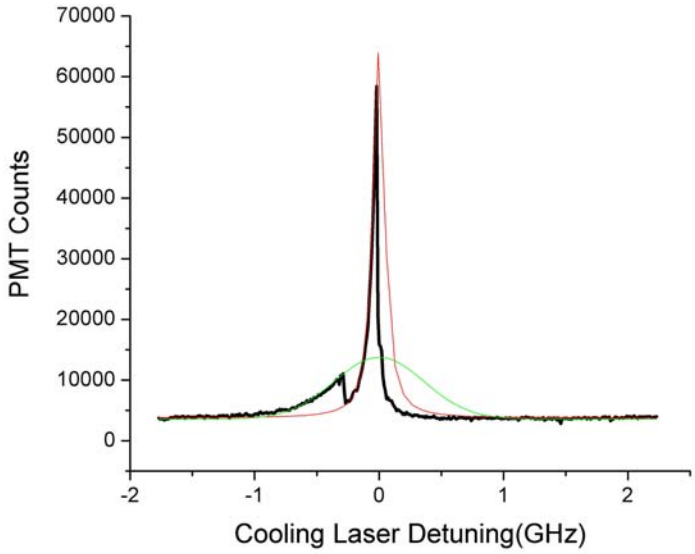

Fig. 29. Voigt lineshape fitting of laser cooling spectroscopy.

In the early stage of the experiments, the laser cooling spectroscopy was the major tool to study the laser cooling and sympathetic cooling [21, 22, 57]. Several interesting experiments were carried out to evaluate the influence of the RF heating to the crystals, the UV power broadening to the cooling transitions, the buffer gas heating to the crystals, and the effect of different ion numbers. This information provided valuable reference for the imaging experiments.

4.2 Ion crystal image

Two cameras are used to take images of ion crystals. These imaging systems facilitate the direct observation of the ion clouds and ion crystals, which provide more information of the laser cooling, sympathetic cooling and ion dynamics in the trap. Also both cameras are capable to work on the spectroscopy experiments. The MCP camera is used to take the images of small number of ion crystals. For ion crystals, ions are localized in a small region, the micro motion is negligible in most of the cases, thus, the ions can be treated as being confined in a three dimensional harmonic potential well,

$$\phi(r,z) = \frac{m}{2}(\omega_r^2 r^2 + \omega_z^2 z^2), \tag{5.2}$$

where r is the distance from the trap axis, ω_r is the secular frequency, which is the radial oscillating frequency, z is the distance from the trap center along the trap axis, and ω_z is the axial frequency. A measurement of the trap anisotropy is given by the parameter α, which is defined as:

$$\alpha \equiv \frac{\omega_z^2}{\omega_r^2}. \tag{5.3}$$

For a given number N of the ions, the crystal structure depends only on α [20, 23]. In the experiments, the chain mode, the zigzag mode and the shell mode were observed with different setting of α and difference number of ions.

4.2.1 Equilibrium positions of small ion chains

An ion chain with more than 70 ions was observed in the experiments, as showed in Fig. 30. All the images taken by the single photon camera use the false color code, the different color shows different intensity. From low intensity to high intensity, the

defining colors are black, blue, red and yellow. The ions crystals are stored in the trap for hours under UHV, as long as the cooling laser beam exists.

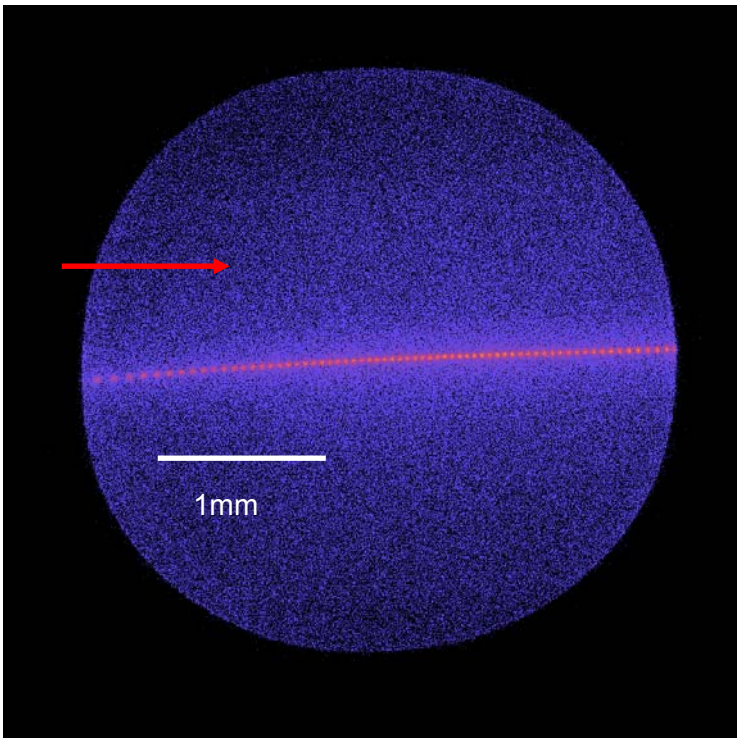

Fig. 30. A long ion chain containing about 70 ions.

It is interesting to include some theoretic calculations for ion positions to compare with the experimental results [58]. For a chain with N ions in the trap, because of the strong bounding in the radial direction and weak bounding in the axial direction, the ions are all on the center axis of the trap. By numbering the ions from left to right, the position of mth ion is assigned as z_m. Hence the potential energy of the ion chain is:

$$V = \sum_{m=1}^{N} \frac{1}{2} m\omega_z^2 z_m^2 + \sum_{\substack{n,m=1 \\ m\neq n}}^{N} \frac{e^2}{8\pi\varepsilon_0} \frac{1}{|z_n - z_m|}. \tag{5.4}$$

Suppose the $z_m^{(0)}$, is the equilibrium position of the mth ion, the equilibrium positions of ions will be determined by the following equation:

$$\left(\frac{\partial V}{\partial z_m}\right)_{z_m = z_m^{(0)}} = 0 . \tag{5.5}$$

By defining the length scale $l^3 = \frac{e^2}{4\pi\varepsilon_0 m\omega_z^2}$ and the dimensionless equilibrium position $u_m = z_m^{(0)} / l$, the Eq. (5.4) can be rewritten as the following set of N couple equations for the values of u_m:

$$u_m - \sum_{n=1}^{m-1} \frac{1}{(u_m - u_n)^2} + \sum_{n=m+1}^{N} \frac{1}{(u_m - u_n)^2} = 0 , \tag{5.6}$$

$$(m = 1,2,...,N) .$$

By solving the equations, the scaled equilibrium positions of ion chains with different ion numbers are given in the Table IV.

Table IV. Scaled equilibrium positions of ion chains [58].

N	Scaled equilibrium positions
2	-0.630 0.630
3	-1.08 0 1.08
4	-1.44 -0.454 0.454 1.44
5	-1.74 -0.822 0 0.822 1.74
6	-2.01 -1.14 -0.370 0.370 1.14 2.01
7	-2.25 -1.41 -0.687 0 0.687 1.41 2.25
8	-2.47 -1.66 -0.967 -0.318 0.318 0.967 1.66 2.47
9	-2.68 -1.89 -1.22 -0.600 0 0.600 1.22 1.89 2.68
10	-2.87 -2.10 -1.45 -0.854 -0.282 0.282 0.854 1.45 2.10 2.87

Fig. 31 gives a summary of the small ion chains observed in the experiments, the theoretical scaled equilibrium positions are displayed in the inset.

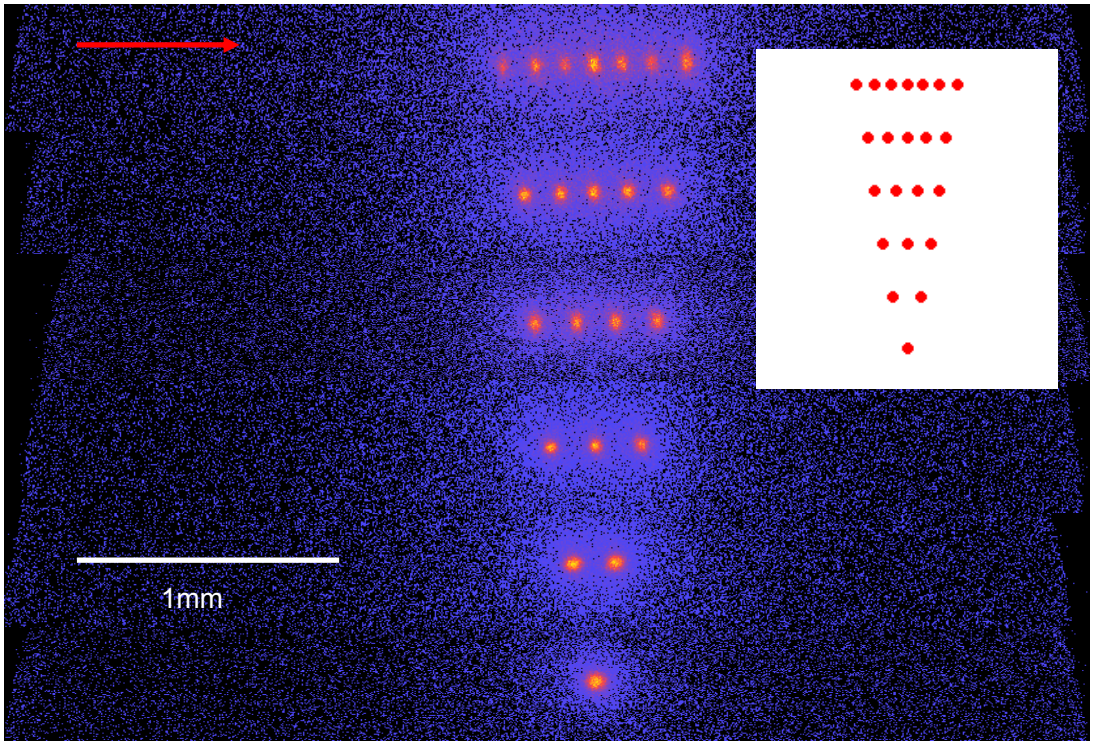

Fig. 31. Equilibrium positions of small ion chains.

Experimentally the radial oscillating frequency or the secular frequency can be measured with a secular scan, while the axial frequency is hard to measure. Usually, the axial frequency is estimated with electric potential simulations of the end cap voltages. With a very good match of theoretic and experimental results, the axial frequency can be calculated from the distance of the ions in the equilibrium state, and compared with the simulation results. Fig. 31 shows that the separation between the ions varies with

different ion numbers. At both ends of ion chain, the ions are further apart, and in the middle of the ion chain, they are closer.

4.2.2 Ion crystal images with different parameters

There are many parameters in the ion trap, which affect the image qualities. For example, the RF trapping voltage or end cap DC voltage can be adjusted to see how the changes of electric potentials move the ion crystal or change the ion crystal shapes. In addition, the UV power or UV detuning can be varied to see how the ion crystal responds with different settings of laser cooling.

Fig. 32 shows the images of same ion crystals at different RF trapping voltage.

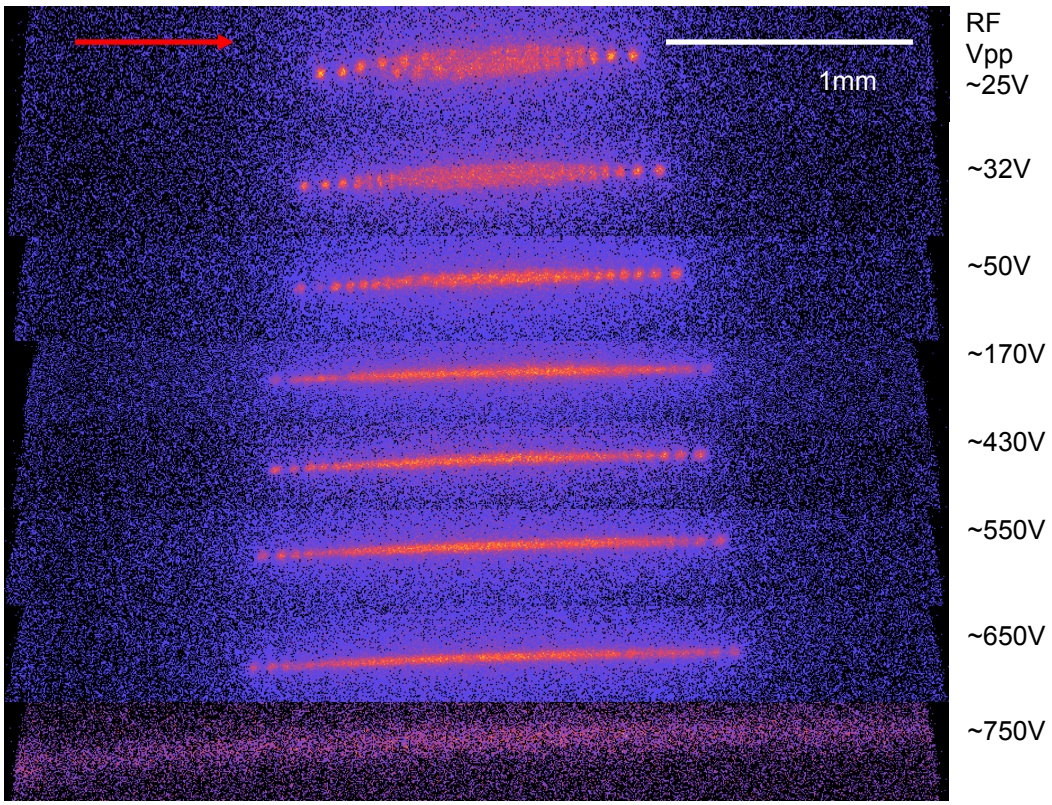

Fig. 32. Ion crystal at different RF trapping voltages.

At low trapping voltage, the ion chain is more likely to evolve into a zigzag mode. This feature will be discussed in the next sub section. If the RF trapping voltage is above 750V, an ion chain dissolves into an ion cloud. Under this RF voltage, the ions are still in the stability region ($q \sim 0.42$). But because of strong RF heating caused by the high RF trapping voltage, the ion crystal melts to an ion cloud. This is depicted as a trace of UV beam in last stripe of Fig. 32. We only see the fluorescence emitted by the ion cloud in the region of the laser beam.

Fig. 33 shows ion chain images at different DC voltages on the outer segments, the voltages are labeled at both sides of the Fig. 33. Because the center segment is 50 mm, it's so long that the quadrupole structure of ion trap actually prevents the DC field to penetrate into the trap center. Thus there is no structure change of the ion chain, the whole ion chain is just being pushed by DC voltages. Also because of the stray electric field introduced by some wiring problems, the ion crystals are actually off the geometry center of the trap, the left side segment DC shows much more influence on the ion chain than the right side.

To the axial confinement more effective, two ring electrodes were placed around the electrodes of the center section. The distance between the rings is 16 mm, each ring is about 8 mm away from the trap center. It provides a tighter confinement in the axial direction. Unfortunately the voltages that can be applied on to the rings are limited to 2.5 kV, which is not enough to observe the drastic shape change of the ion crystals, and this issue will be discussed in the next sub section. The Fig. 34 shows the effective manipulation of an ion chain with the ring voltages labeled at both sides.

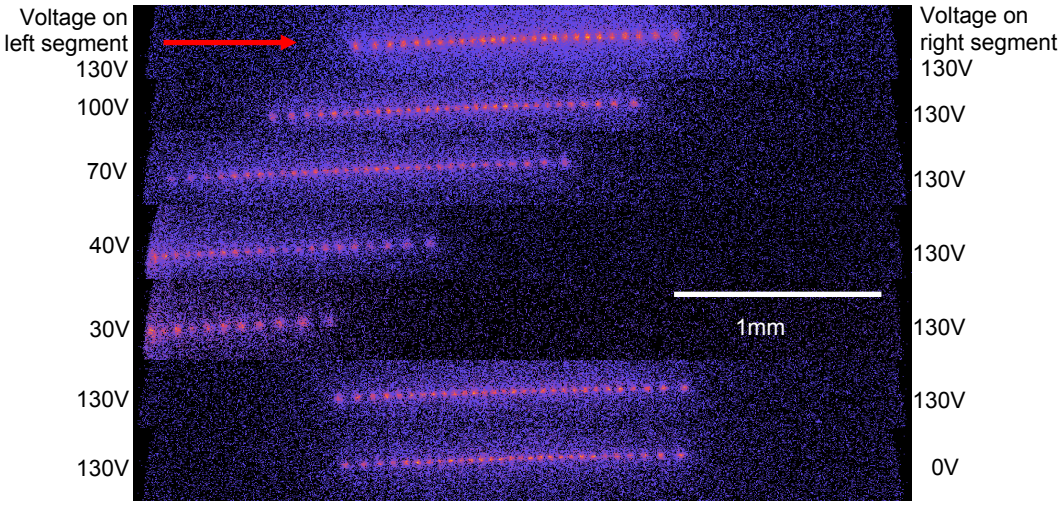

Fig. 33. Ion chain at different DC voltages on the side segments.

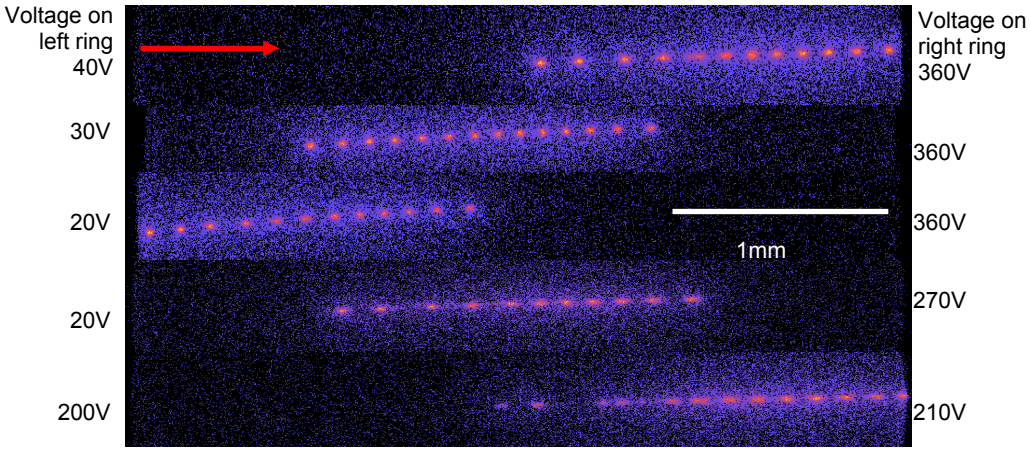

Fig. 34. Ion chain at different DC voltages on the rings.

Still ion crystals are off the trap geometry center, one side of the ring is closer to ion crystals than the other. Sometimes the shade of this ring can be seen in the images. In Fig. 34, it is estimated that the one ring is about 3 mm away from the ion crystal, while the other is about 13 mm away. And the ion chain is about 5 mm off the trap geometry center.

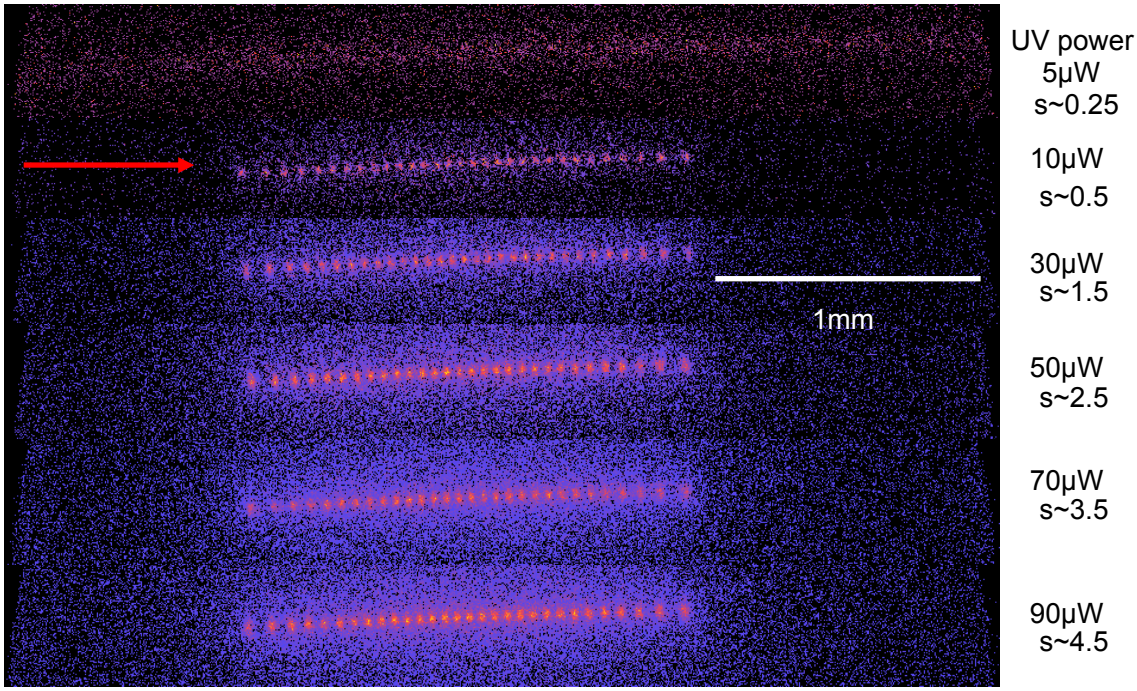

Fig. 35. Ion chain at different UV powers.

Fig. 35 shows the ion chain images with different UV powers. The shape of ion chain doesn't change with different UV Ppowers, while the intensity of the fluorescence is increased with UV power as expected. Also in this situation, when the power is too low, less than 5 μW, the ion crystal melts to the ion cloud because the low laser cooling power could not balance the RF heating and residual gas heating.

Fig. 36 shows the ion chain images with different UV detunings. The linewidth of the dye laser is about several MHz. The UV linewidth should be double of the linewidth of the dye laser, estimated about ~10MHz. When the UV detuned close to the transition, the intensity of fluorescence increased, the shape of the chain did not change. When the UV was very close to the cooling transition, the ion chain showed some oscillations in radial direction.

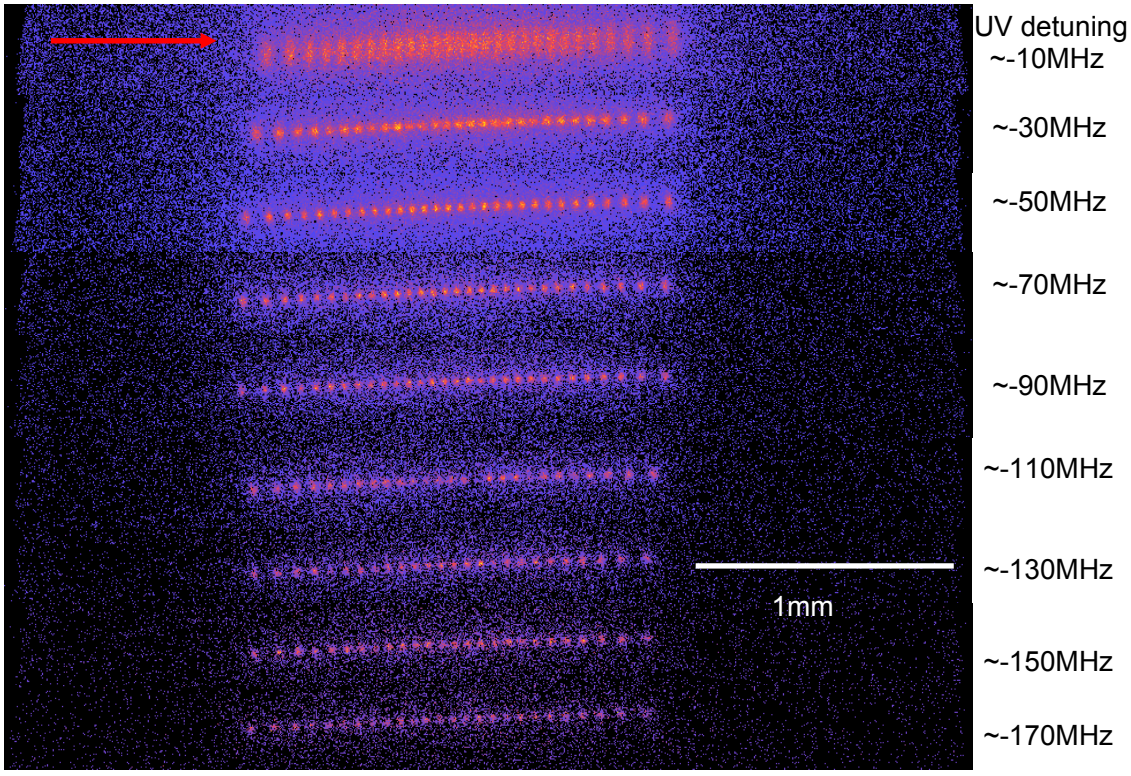

Fig. 36. Ion chain at different UV detunings.

4.2.3 Structure phase transition in ion crystals

Besides the phase transition of cloud state to crystal state, the ion crystals also have the structural phase transitions in the crystal state. Depending on the ion number N and the parameter $\alpha \equiv \omega_z^2 / \omega_r^2$, the ion crystal could show different shapes, the chain mode, the zigzag mode, the helical shell mode and the planar mode [20, 23]. For the current trap, chain mode, zigzag mode and helical shell mode of ion crystal was observed for different ion numbers and different α parameters. These results we compiled in Fig. 37, Fig. 38 and Fig. 39. Because of the lack of efficient control of the axial frequency, the planar ion crystal has not been observed yet.

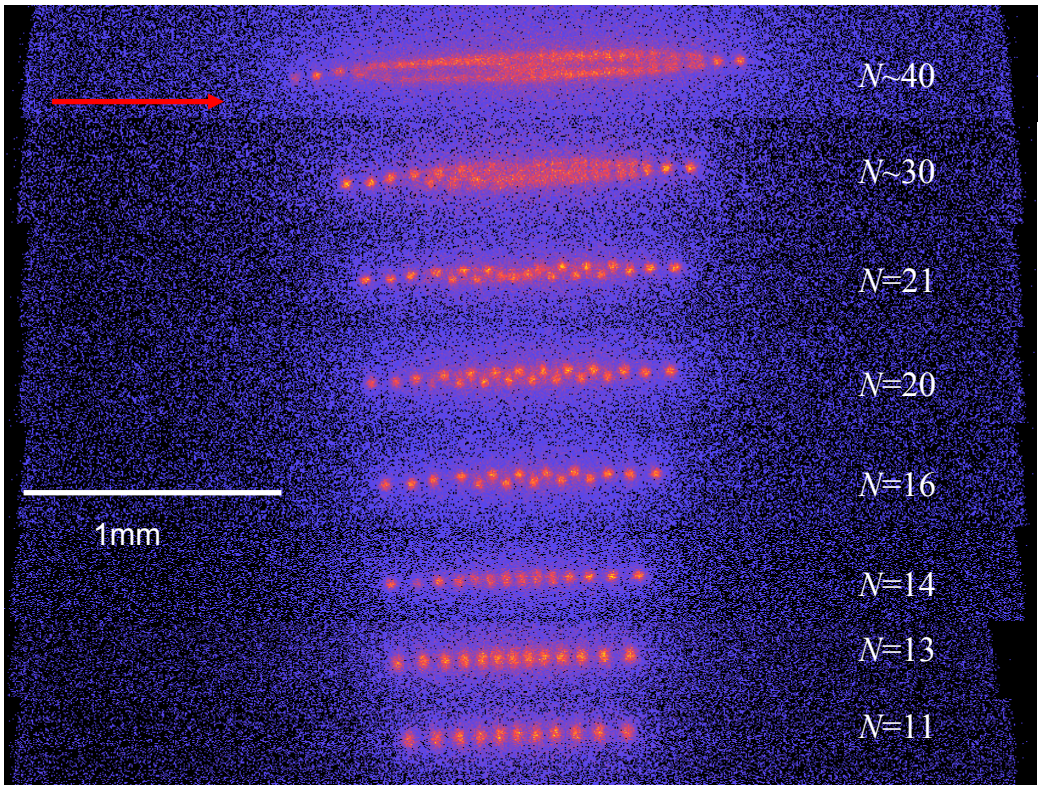

Fig. 37. Structure phase transition of ion crystals at constant α. (α~0.02).

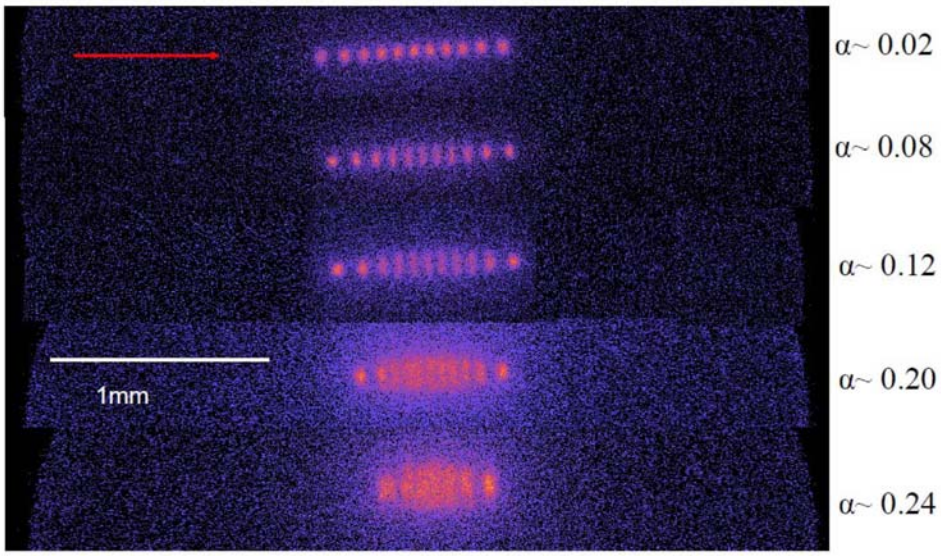

Fig. 38. Structure phase transition of ion crystals with 11 ions.

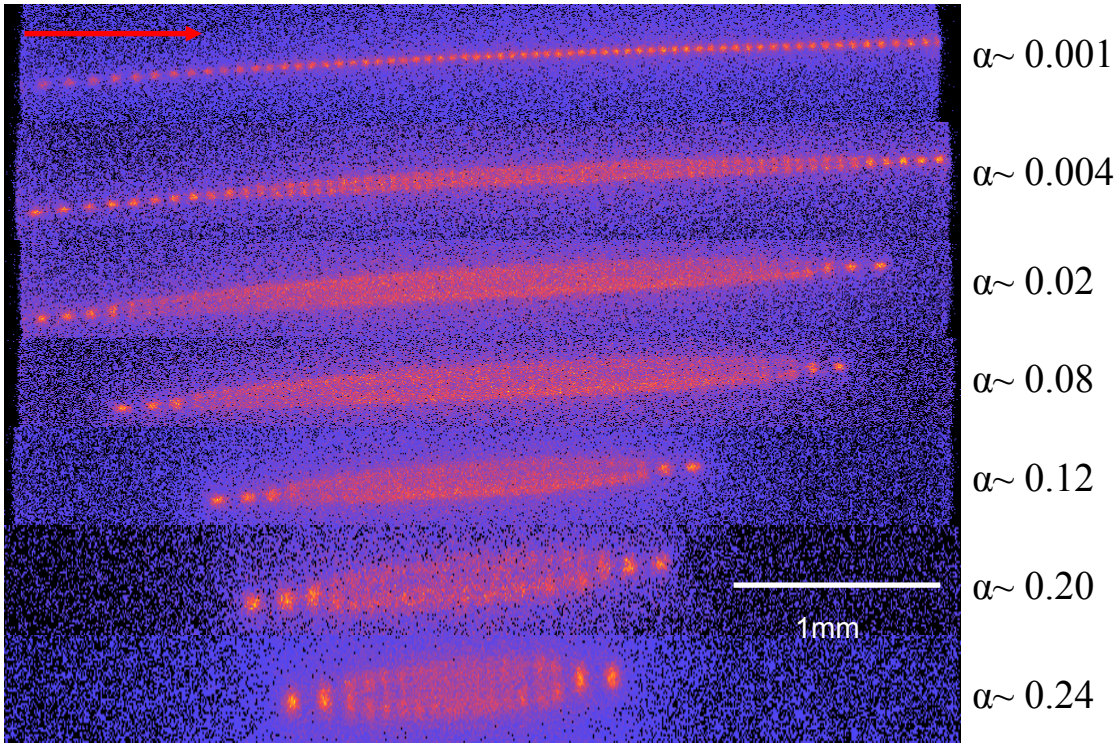

Fig. 39. Structure phase transition of ion crystals with ~70 ions.

In Fig. 37, the RF potential and end cap DC kept the same, and the crystal changed modes with different ion numbers. In Fig. 38 and Fig. 39, the ion numbers are roughly the same, while the end cap DC was changed with the recently added rings, thus the crystals changed modes with different parameter α. And in Fig. 38 and Fig. 39, the ions in the zigzag positions show some oscillations between different positions. Simply because in the zigzag mode, the energy configurations are the same if the ions jump to the other side of trap axis with an environment disturbance, such as residual gas collision, stray electric field, etc. And for the shell mode, the image is somehow blurred, but in the same configuration of camera and condenser, the ion chain modes with different RF and DC setting are quite clear. There are probably several reasons, the axial

confinement of the ions is not strong, thus not only quite large spaced ion chains are produced, but also the ion shell modes are larger, the width of the crystal can be around 200 μm. The amplitude of micro motion is larger with the ions are further away off the trap axis, also it might be that some of the ions at the surface of the shell mode are out of the focus plane of the image, which also makes the image blurred.

In a linear RF trap, the ions are confined in the trap axis to form an inhomogeneous 1D ion chain, if the α is small. As α increases, Coulomb repulsion induces an instability of the ion chain, and forms a zigzag mode for the ions near the trap center. As the α increase further, the zigzag develops a twist, forming an inhomogeneous helix or shell. For a is really large, the ions collapse into the x-y plane, forming a distorted 2D hexagonal lattice.

By comparing the energies of these structures, it was predicted that the transitions occur when the ratio of the Coulomb potential and the radial electric potential reaches some constants [20, 23],

$$(q^2 / md^3)^{1/2} / \omega_r = x_i , \tag{5.7}$$

where d is the axial spacing between charges of charge q. It was found that for zigzag transition, x_1 = 2.05 [59], and for helical transition, x_2 = 1.29 [60]. At lower transition values x_i, more complex structures occur consisting of concentric cylindrical shells of ions [60-63].

In reference [20], two equations were introduced to describe these two phase transition boundaries:

$$\alpha_i(N) = \left(\frac{8}{3x_i N}\right)^2 [\ln(3Nx_i / 2^{3/2}) - 1], i = 1,2, \tag{5.8}$$

where N is the ion number.

To produce the 2D planar disk mode of the ion crystals, a scaling law of the criterion is also given as:

$$\alpha_3(N) = (96N / \pi^3 w_1^3)^{1/2}, \tag{5.9}$$

where w_1=1.11 is the first 2D dimensional transition value from 3D helical shell mode, which is analogous to the 1D transition value x_1 [20].

Using the Eq.(5.8) and (5.9), the phase transition map could be drawn as Fig. 39. For the phase transition images in Fig. 37, Fig. 38 and Fig. 39, they are corresponding to the red, blue and black lines in the phase transition map of Fig. 40 respectively.

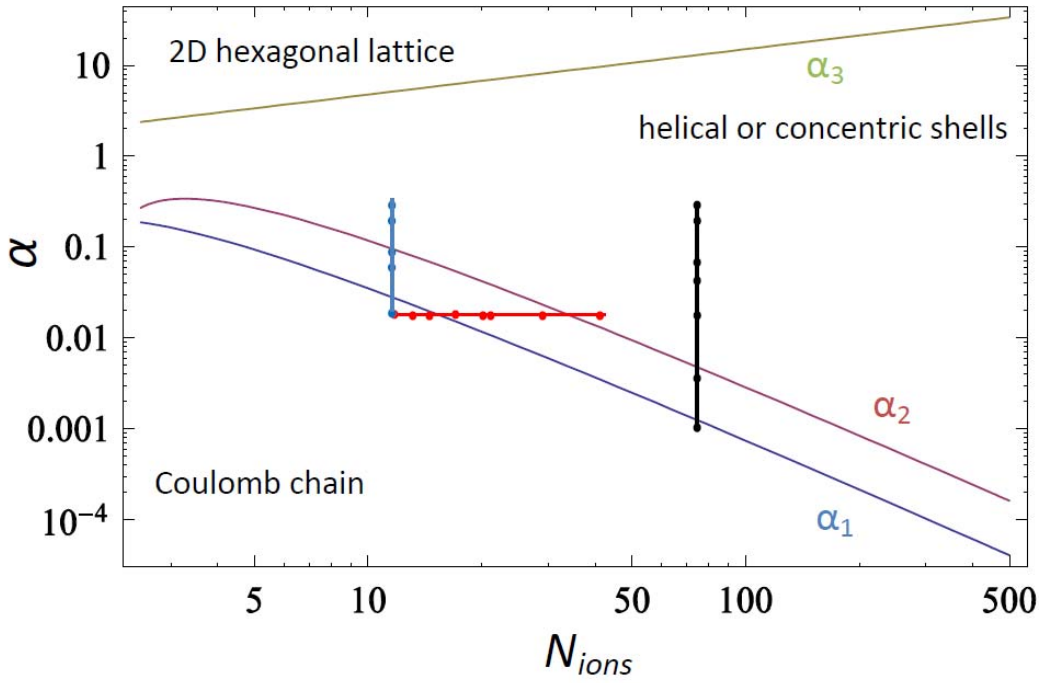

Fig. 40. Structure phase transition diagram of ion crystals in a linear RF trap.

In our present setup, the endcap DC voltages applied to the ring electrodes are limited to 2.5 kV. According to the structure phase transition map, we still need a magnitude higher endcap voltage to increase the parameter α to realize the 2D planar structure of the ion crystals.

4.3 Sympathetic cooling

The study of sympathetic cooling is also a major goal in this dissertation. Experimentally several ion species were studied, which includes the $^{26}Mg^{+}$, $^{4}He^{+}$, H_2^{+}, C_{60}^{+}.

In ion trap, the sympathetic cooling can be used to reduce the translational kinetic energy of the stored molecular ions. These cold molecules provide an opportunity to study the spectroscopic molecular properties precisely. Ultra cold molecules are proposed to be used in tests of the time independence of the proton to electron mass ratio [64]. Also they are proposed to be used in the quantum computations [65].

4.3.1 $^{26}Mg^{+}$

$^{26}Mg^{+}$ is an interesting target for studying the sympathetic cooling. In fact, even in the early stage of the experiments, when the ion cooling spectroscopy were taken, $^{26}Mg^{+}$ showed up with the $^{24}Mg^{+}$ in many situations if the laser scanning width extended to its cooling transition, which is about ~3.088 GHz above the transition of $^{24}Mg^{+}$ [44], as shown in Fig. 41.

Both of the spectrum peaks have the phase transition dips, which indicate $^{26}Mg^{+}$ ions are sympathetically cooled by $^{24}Mg^{+}$ ions when the laser is red tuned to $^{24}Mg^{+}$

cooling transition. When the laser passes the center of $^{24}Mg^{+}$ transition, laser cooling becomes laser heating, and some of the $^{24}Mg^{+}$ obtain sufficient kinetic energy and leave the trap. As the laser is moving close to $^{26}Mg^{+}$ transition, the $^{26}Mg^{+}$ ions get laser cooled and might also sympathetically cool the remaining $^{24}Mg^{+}$ in the trap.

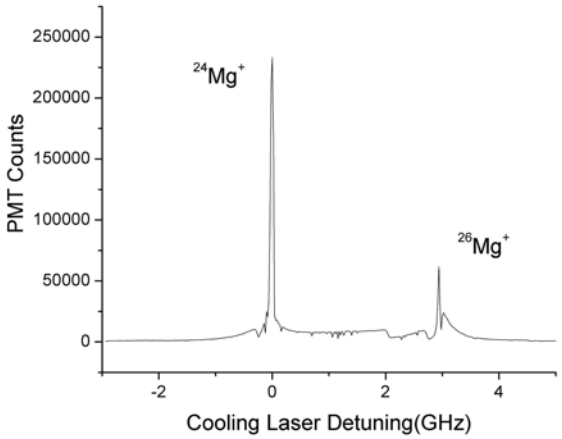

Fig. 41. Laser cooling spectra of $^{24}Mg^{+}$ and $^{26}Mg^{+}$.

Since two dye lasers are available, after individually photoionized $^{24}Mg^{+}$ and $^{26}Mg^{+}$ with different photoionization wavelengths (17525.63 $cm^{-1}\times2$ for $^{24}Mg^{+}$, 17525.68 $cm^{-1}\times2$ for $^{26}Mg^{+}$) the photoionization dye laser could be tuned to the $^{26}Mg^{+}$ cooling transition, and the SHG cavity needs to be realigned to get the right UV beam to cool $^{26}Mg^{+}$. Though it takes about half an hour to make the alignment, the ion life time is quite long in UHV. Thus the $^{26}Mg^{+}$ and $^{24}Mg^{+}$ mixed crystals could be imaged and studied.

As Fig. 42 shows, there are three sets of different numbers of $^{26}Mg^{+}$ and $^{24}Mg^{+}$ at constant α=0.02 for $^{24}Mg^{+}$. For each set, the top image was taken when both cooling

lasers for $^{26}Mg^{+}$ and $^{24}Mg^{+}$ were on, the middle image was taken when only $^{24}Mg^{+}$ cooling laser was on, the bottom image was taken when only $^{26}Mg^{+}$ cooling laser was on.

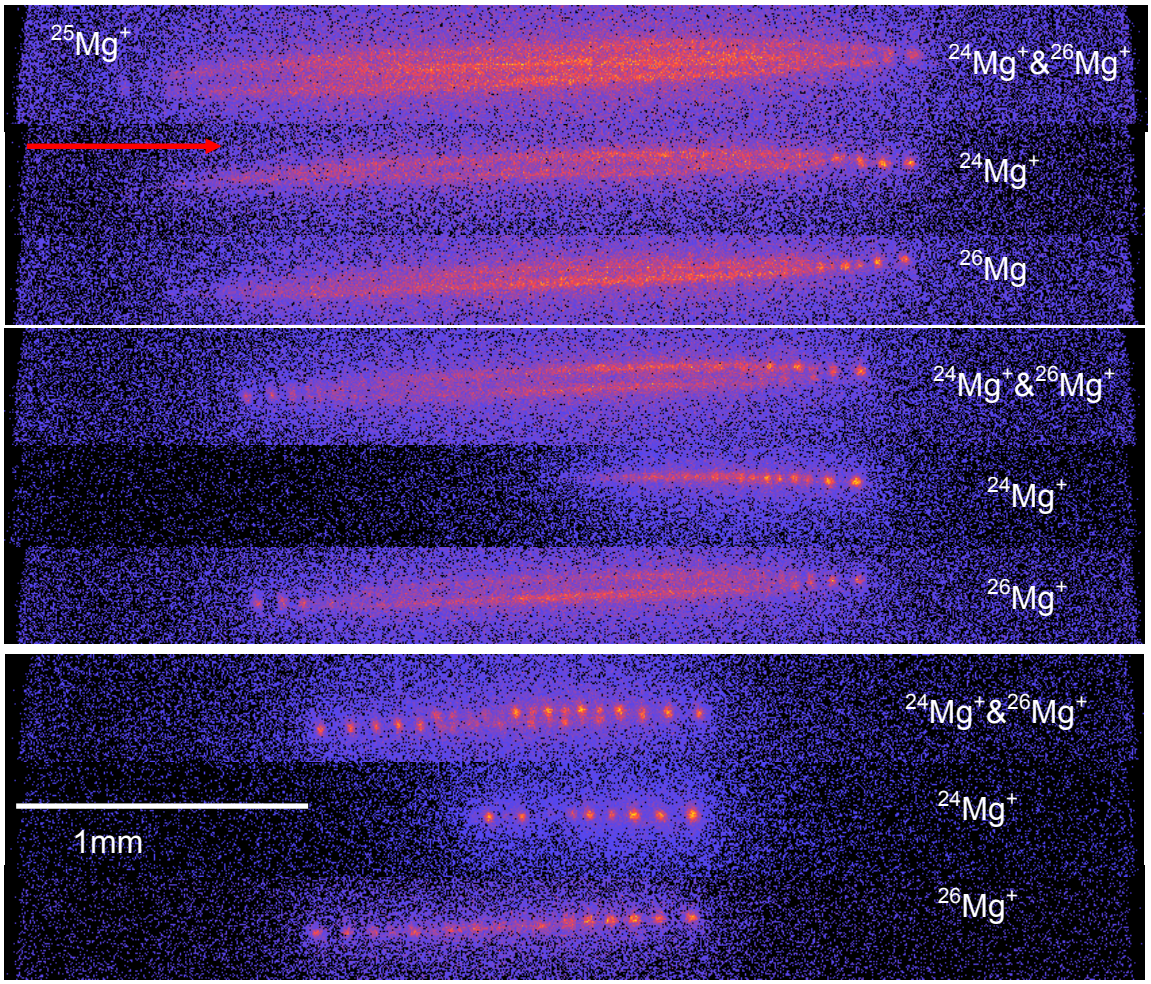

Fig. 42. $^{26}Mg^{+}$ and $^{24}Mg^{+}$ mixed ion crystals.

The charge to mass ratios of the $^{26}Mg^{+}$ and $^{24}Mg^{+}$ are very close, and the sympathetic cooling is quite effective. When the laser cooling only exists for one ion specie, only the laser cooled ions could be seen by fluorescence, but comparing these

images, the crystals almost remains the same shape with the crystals when both cooling lasers are on. Due to the radiation pressure, the laser cooled ions tend to occupy the positions in the crystal far away from the laser source and the dark or sympathetically cooled ions take positions of the ion crystals, which are close to the laser source.

4.3.2 $^{4}He^{+}$

In the other three sympathetic cooling species, $^{4}He^{+}$ has the lowest charge to mass ratio difference with the $^{24}Mg^{+}$, therefore it's relatively easy to trap, take the images and identify $^{4}He^{+}$ in the crystal. First, He was leaked into the chamber to about 10^{-8}mbar pressure, then the electron gun was turned on to bombard He atom to create and trap the $^{4}He^{+}$ in the trap. After that, the Mg oven was turned on, photoionization and cooling laser was directed through the trap to create and cool the $^{24}Mg^{+}$. Meanwhile the leak valve was shut off, and the vacuum was back to UHV in several minutes. After the loading of two ion species, the cooling laser was slowly scanned from far red detuned frequency to find the phase transition to get the mixed crystals. Fig. 43 shows typical images of the mixed $^{4}He^{+}$ and $^{24}Mg^{+}$ crystal. From the top to bottom, α = 0.02, 0.08 and 0.12 for $^{24}Mg^{+}$.

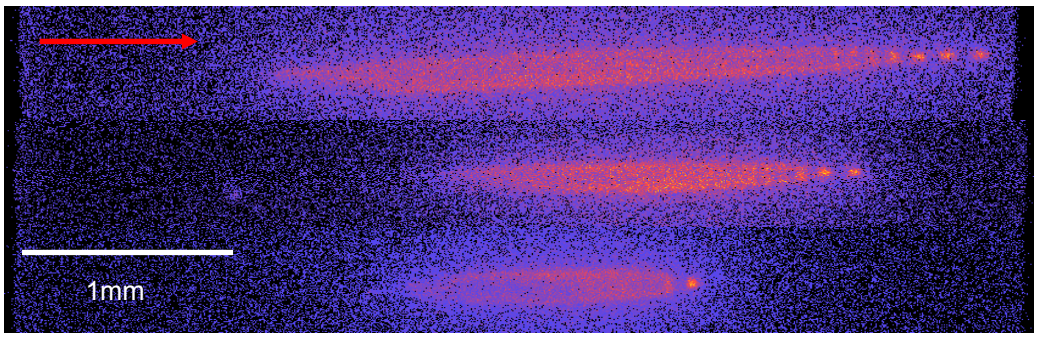

Fig. 43. $^{4}He^{+}$ and $^{24}Mg^{+}$ mixed ion crystals.

The bottom image of Fig. 43 was taken when the axial confinement DC increased, thus the ions were squeezed in the axial directions. Because of the radiation pressure, the $^{24}Mg^{+}$ ions occupied the positions of the ion crystal far away from cooling laser source. In this case, a high voltage of 1.6 kV was applied on the ring, the $^{24}Mg^{+}$ ions form the shell structure, while the $^{4}He^{+}$ ions were inside the shell structure and appeared as a darker region than the positions where $^{24}Mg^{+}$ ions were.

Optical secular scan was used to identify the ion species in the mixed crystals. It was quite successful for the $^{4}He^{+}$ and $^{24}Mg^{+}$ mixed ion crystals. An optical secular scan is shown in Fig. 44.

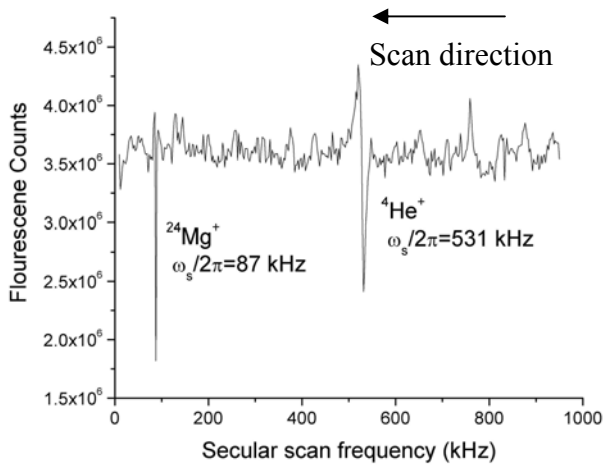

Fig. 44. Optical secular scan for a $^{4}He^{+}$ and $^{24}Mg^{+}$ mixed ion crystal.

The optical scan is based on observing the fluorescence while the secular frequency is scanned. Depending on the laser detuning, when the scanning frequency coincides with the secular frequency of the trapped ions, the fluorescence can rise or drop. As Fig. 29 shows, if the red laser detuning is not far from the center of the

transition, the ions get kinetic energy from the scanning RF field, the crystal melts to cloud, the fluorescence will drop momentarily, form a dip in the photon counts, just like Fig. 43 shows. If the red laser detuning is a little far from the center of the transition, then the fluorescence will rise shortly, form a peak in the photon counts. There are some noises in Fig. 44, mainly because the power of the UV beam was not stabilized.

The Qscan can be used to determine how many ions were trapped in the ion trap. A typical Qscan is like Fig. 25. Taking into account the 15% SEM detection efficiency, there were about ~60 $^{4}He^{+}$ and ~120 $^{24}Mg^{+}$ in the trap.

4.3.3 H_2^+

The procedure to create H_2^+ is just like the He^+, H_2 was leaked into the chamber and bombarded with electrons from the electron gun. However it was found that when the Mg^+ is at the excited state *3p*, it has probability to undergo chemical reaction with the H_2 in the background, and form the MgH^+ [17, 45],

$$Mg^+ (3p) + H_2 \rightarrow MgH^+ + H. \qquad (5.9)$$

The consequence of this reaction is that in the experiments the Mg^+ ions are lost very quickly in the H_2 environment, as indicated in Fig. 45, the $\alpha = 0.12$ constant for $^{24}Mg^{+}$ in this experiment. It was tried to minimize this unwanted reaction by precisely control the leak flow of the H_2 to the work chamber, and producing H_2^+ before the $^{24}Mg^{+}$ ions. First, H_2 was leaked into the chamber to about 5×10^{-9} mbar pressure through a precision leak valve, then the electron gun was turned on to bombard H_2 molecule to create and trap the H_2^+ in the trap. After that, the Mg oven was turned on, both photoionization and cooling laser were directed through the trap and create and cool the

$^{24}Mg^{+}$. Meanwhile the leak valve was shut off, and the vacuum was back to UHV in hours because the turbo molecular and VacIon pumps do not pump H_2 effectively. After the loading of two ion species, the cooling laser was slowly scanned from far red detuned frequency to find the phase transition to get the mixed crystals.

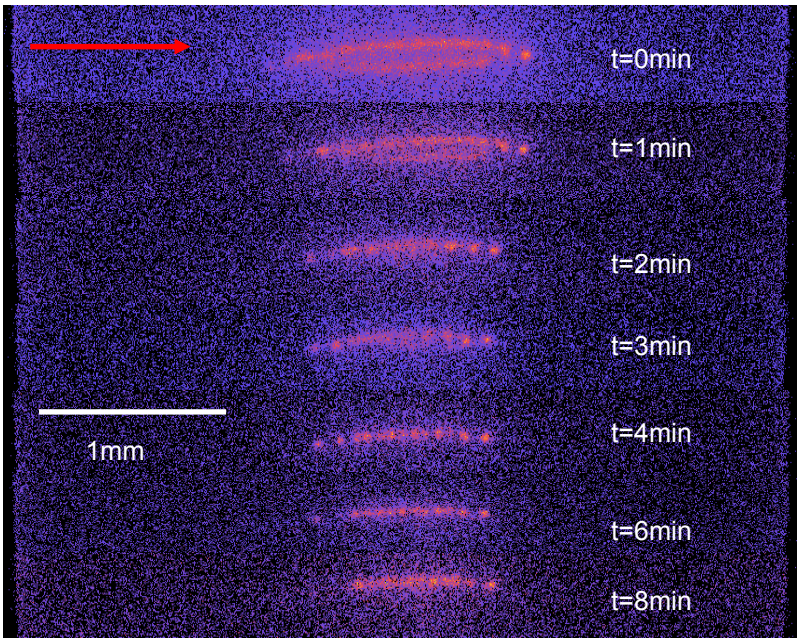

Fig. 45. H_2^{+} and $^{24}Mg^{+}$ mixed ion crystals in H_2.

The similar procedure as creating He^{+}, was used to create the mixed H_2^{+} and $^{24}Mg^{+}$. First, H_2 was leaked into the chamber to about 5×10^{-9} mbar pressure through a precision leak valve, then the electron gun was turned on to bombard H_2 molecule to create and trap the H_2^{+} in the trap. After that, the Mg oven was turned on, photoionization and cooling laser was directed through the trap and create and trap the $^{24}Mg^{+}$. Meanwhile the leak valve was shut off, and the vacuum was back to UHV in hours because the turbo molecular and VacIon pump do not pump H_2 effectively. After

the loading of two ion species, the cooling laser was slowly scanned from far red detuned frequency to find the phase transition to get the mixed crystals.

One of the mixed crystals is showed in Fig. 45. The crystals are somewhat blurred. This is due to the experimental situation where the background vacuum is at 10^{-9} mbar range and about one magnitude higher than the UHV, the $^{24}Mg^{+}$ ions have more collisions with the residual gas molecules, mainly H_2. As can be seen in Fig. 45, the $^{24}Mg^{+}$ ions lost rather quickly over period of minutes, while the remaining ions emitting fluorescence still kept almost the same shape, which indicates that there were still ions, which just did not emit fluorescence any more. This is caused by the $^{24}Mg^{+}$ ions at *3p* excited state have chemical reactions with background H_2, and the reactions produced $^{24}MgH^{+}$ ions, which were still sympathetically cooled, and maintained positions in the crystal.

Because the charge to mass ratio of $^{24}Mg^{+}$ and H_2^{+} is quite large, a small q for $^{24}Mg^{+}$ is a 12 times larger q for H_2^{+}. Thus the secular scan simultaneous identification was not convincing. The Qscan can be used to determine how many ions were trapped in the ion trap. A typical Qscan is like Fig. 46.

Taking into account the 15% SEM detection efficiency, there were about ~200 H_2^{+} and ~200 $^{24}Mg^{+}$ or $^{24}MgH^{+}$ in the trap. It turns out that H_2^{+} could be trapped and sympathetically cooled by $^{24}Mg^{+}$, but the period is limited by the chemical reaction rate of $^{24}Mg^{+}$ and H_2. Normally it's in the order of several minutes. This situation is quite a challenge for the proposed precision spectroscopy on H_2^{+}.

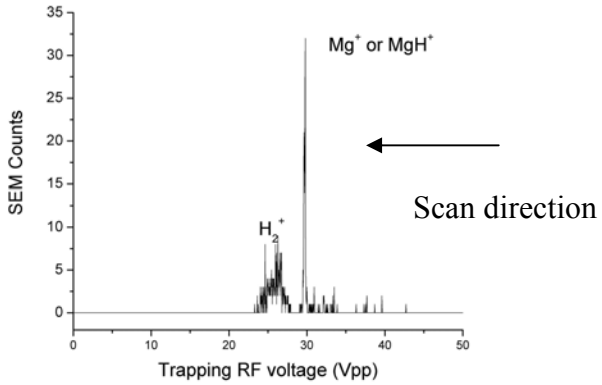

Fig. 46. Qscan of a H_2^+ and $^{24}Mg^+$ mixed ion crystal.

4.3.4 Fullerene ions

Because of the huge charge to mass ratio difference between C_{60}^+ (720 amu) and $^{24}Mg^+$ (24 amu), it was not possible to cool the C_{60}^+ and $^{24}Mg^+$ mixture to the crystal state. There are several reasons, C_{60}^+ has a 30 times the mass of $^{24}Mg^+$, it needs a higher RF voltage to trap the C_{60}^+ ions. While for simultaneously trapped $^{24}Mg^+$, the high RF voltage will bring much more RF heating. The stability diagram for simultaneously trapped $^{24}Mg^+$ and C_{60}^+ ions is depicted in Fig. 47. Also, in the cloud states, C_{60}^+ ions occupy the places which are far away from the trap axis, while the $^{24}Mg^+$ ions take the places near the trap axis, there is no cage of the laser cooled ions to the sympathetic cooled ions. And because of the large mass difference, the kinetic energy transferred by the collisions is quite small. Thus the efficiency of the sympathetic cooling is quite low.

The simultaneously secular scan identification of the C_{60}^+ and $^{24}Mg^+$ mixed cloud was not convincing. Fig. 48 shows one secular scan for C_{60}^+, the trapping voltage is around ~550 Vpp, it is a quite large q (~0.3) for $^{24}Mg^+$, a really low q (~0.01) for C_{60}^+. The Fig. 49 shows a better secular scan for the C_{60}^+ with a little high q setting for C_{60}^+,

the trapping voltage is around ~3000 Vpp, low q(~0.06) for C_{60}^{+}, not stable for $^{24}Mg^{+}$ (q~1.8).

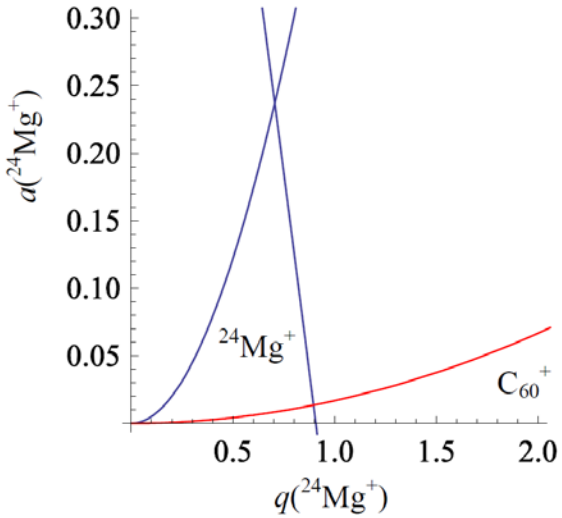

Fig. 47. Lowest stability region of $^{24}Mg^{+}$ and C_{60}^{+}.

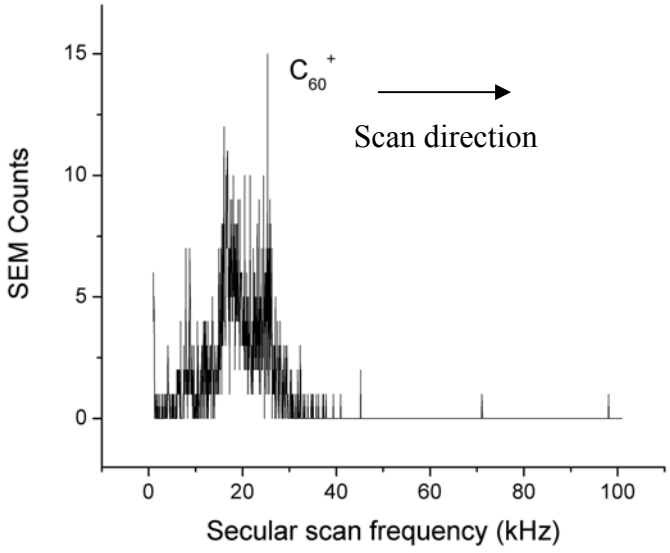

Fig. 48. Secular scan of C_{60}^{+} at q=0.01.

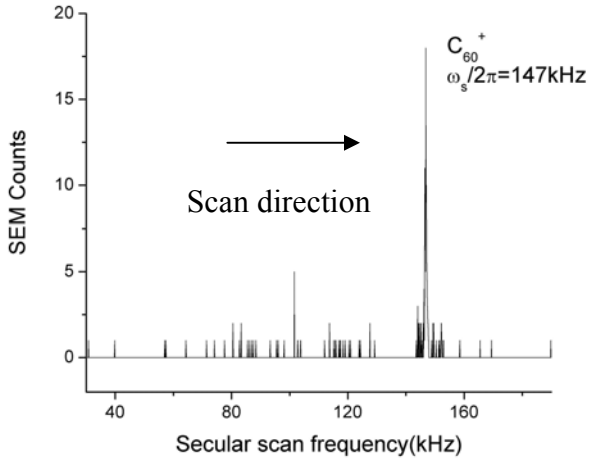

Fig. 49. Secular scan of C_{60}^{+} at q=0.06.

The laser cooling spectroscopy was used for the cooling evaluation, as in Fig. 50 shows. The HWHM linewidth is around 250 MHz. Accordingly, the temperature of the mixed ion cloud is estimated about ~10 K [22]. The Qscan could be used to determine how many ions were trapped in the ion trap. The typical Qscan is like Fig. 51.

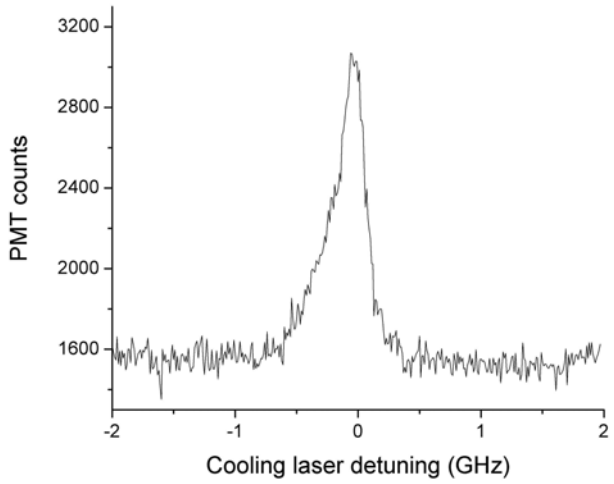

Fig. 50. Laser cooling spectroscopy of a mixed cloud of $^{24}Mg^{+}$ and C_{60}^{+}.

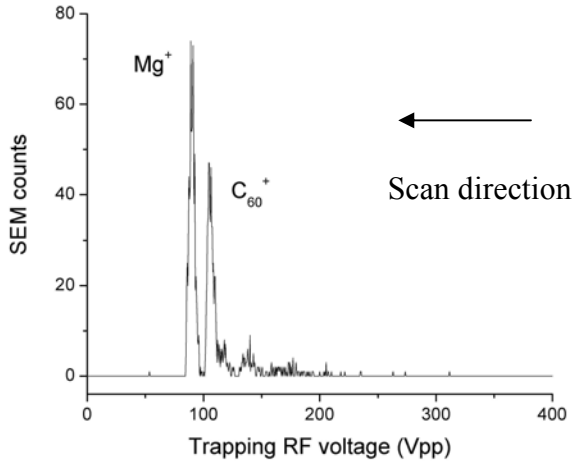

Fig. 51. Qscan of a mixed cloud of $^{24}Mg^{+}$ and C_{60}^{+}.

A typic Qscan of the mixed ion cloud is as Fig. 51. Taking into account the 15% SEM detection efficiency, there were about ~3000 C_{60}^{+} and ~4500 $^{24}Mg^{+}$ in the trap.

Experimentally, the largest mass of the singly charged ion specie, which has been sympathetically cooled to less than 150 mK with laser cooled $^{138}Ba^{+}$ ions in a linear RF trap, is glycyrrethinic acid molecules (471 amu) [16].

CHAPTER V

MOLECULAR DYNAMICS SIMULATION

Molecular dynamics (MD) simulation is a powerful tool in many research areas. In this chapter, a detailed description of the MD simulation for the ions in the linear RF trap and the comparison with the experimental images is provided.

5.1 Introduction

The MD simulation methods are based on directed numerical calculations of the equations of motion of the particles in a complicated system by approximations of the known physics. The numerical calculations allows the prediction and description of the bulk properties of the system, system dynamics and other complicated phenomena which could not be solved in analytical methods.

With the development of computer science, the MD simulation is applied in many fields, including trapped ions. For the ion trap, these virtual experiments with MD simulation are carried out to compare to the experimental results to verify the ion crystal shapes and structures [59, 63, 66, 67], and to extract information such as the ion number and temperature of the crystals [23, 42]. A variety of cooling or heating effects on the trapped ions can be studied individually or together. In particular, the simulations can be performed with the time varying RF field, or in the approximated pseudo potential, and the results can be compared. For many situations, the simulations only need to compute for a few tens of milliseconds. Therefore, for not too large ion numbers (~1000), if the

pseudo potential is used, the time requirement is about hours for a modern personal computer. This reasonable timing makes the simulations a practical tool.

MD simulations can be straightforwardly extended to study the sympathetic cooling of various ion species. It is used to investigate the ion mass range which can be sympathetically cooled [40, 68], to quantify interactions between a few highly charged molecular ions and large numbers of laser cooled atomic ions [69], and to obtain the temperature of sympathetically cooled heavy molecular ions [70].

5.2 Simulation model

5.2.1 Equations of motions and forces

The MD simulations of the ion crystals in a linear RF trap are based on numerically solving the Newton's equation of motion for each ion,

$$\frac{d^2\vec{r}_i}{dt^2} = \frac{\vec{F}_i(\vec{r}_1,...,\vec{r}_N,\vec{v}_i;t)}{m_i}, \tag{5.1}$$

where i=1,…,N. And m_i, $\vec{r}_i$ and $\vec{v}_i$ are the mass, position vector and velocity vector of the ith ion respectively; $\vec{F}_i$ is the total force acting on the ith ion, which depend on the positions and velocities of all ions, and on time t. There are several contributions to this total force:

$$\vec{F}_i(\vec{r}_1,...,\vec{r}_N,\vec{v}_i;t) = \vec{F}_i^{trap} + \vec{F}_i^{Coulomb} + \vec{F}_i^{Laser} + \vec{F}_i^{stochastic}. \tag{5.2}$$

The trapping force is determined by the trapping potential. Combine Eq. (2.4) and Eq. (2.24), also assume there is only very weak DC offset applied on the electrode, thus near the center of the trap, the trap potential is described by

$$\varphi(x,y,z;t)=\frac{V_{RF}}{2r_0^2}(x^2-y^2)\cos(\Omega t)+\frac{\kappa U_{endcap}}{z_0^2}[z^2-\frac{1}{2}(x^2+y^2)]. \tag{5.3}$$

Therefore the trapping force is calculated by the relation:

$$\vec{F}_i^{trap}=-e_i\nabla\varphi(\vec{r}_i;t), \tag{5.4}$$

where e_i is the charge of the ith ion. The trapping force only depends on the ith ion position and time, and it confines the ions in the ion trap.

As Eq. (2.18) points out, within a low q range, in such a potential, ions have a slow dominant secular motion, with a superimposed fast micro motion. The secular motion of a single ion can be described in a harmonic pseudo potential well. In some simulations, the time independent pseudo potential can be used to replace the time varying RF field,

$$\varphi(x,y,z;t)=\frac{eV_{RF}{}^2}{4m\Omega^2r_0^2}\frac{x^2+y^2}{r_0^2}+\frac{\kappa U_{endcap}}{z_0^2}[z^2-\frac{1}{2}(x^2+y^2)]. \tag{5.5}$$

With the pseudo potential approximation the trap potential is simplified and the micro motion is omitted. It is suitable to simulate a large ion ensemble (~ above 1000 ions) in the trap.

The Coulomb force is the repulsive force from all the other ions confined in the trap:

$$\vec{F}_i^{Coulomb}=\sum_{j=1,j\neq i}^{N}k_c\frac{e_ie_j}{r_{ij}^2}\cdot\frac{\vec{r}_{ij}}{r_{ij}}, \tag{5.6}$$

where is k_c the Coulomb constant, $\vec{r}_{ij}=\vec{r}_i-\vec{r}_j$ is the displacement between the ith and jth ions.

The laser force contains two parts as Eq. (2.35) shows, the velocity independent radiation pressure force, and the velocity dependent damping force, which contributes to the laser cooling. The maximum value of damping coefficient β is obtained when $\Delta = -\gamma/2$ and s=2. Thus the laser force can be simplified as:

$$F_i^{laser} = \frac{\hbar k\gamma}{4} - \frac{\hbar k^2 v_i}{4}. \tag{5.7}$$

The laser cooling force has the same direction with the laser propagation direction. This will be discussed in the cooling method.

The stochastic force is due to the random interaction of the ions with the surroundings, such as the collisions with the residual gas, potential introduced by stray electric field, RF phase shift, etc. A velocity kick model is introduced to simulate these effects. This will be introduced in the heating method.

5.2.2 Initial conditions

In order to solve Eq. (5.1) numerically, initial positions and initial velocities of N ions must be assigned for each ion. The velocity distribution of x, y, and z component of the ions at a certain temperature is Gaussian. So the initial x, y, and z components of velocities of the ions are assigned by a Gaussian random number generator, which makes the initial average translational kinetic energy corresponding to the assigned initial temperature. And the initial positions of the ions are assigned by the random number generator in a radial direction of 100 μm times 100 μm, the z direction about 2000 μm. For the radial direction, consider the UV beam waist is on the order of 100 μm, only if the ions are in the UV beam, the laser cooling force exists. For the axial

direction, it was estimated with the Rayleigh range of the UV beam, it's about several mm range. In the early stage of the simulation, periodic boundary conditions were used. Tt was found that it's not necessary for small ion numbers, especially if the goals of the simulation are to achieve the crystal state.

Sometimes, the settings of the initial conditions can be tricky, especially in the simulation of the process of sympathetic cooling. In simulations, it is often found that some ions are not cooled to the crystal state with the majority of the ions. Instead, they fly around the crystal with several orders larger velocities, while still remain trapped in the ion trap. It is found in simulation that lowering the starting temperature could partially solve this problem.

5.2.3 Algorithm

To solve the equation of motion of the *i*th ion, several algorithms were tried out. For the ion trap, if the real RF trap field is used and the laser cooling damping term is applied, the force or the acceleration of each ion *i* is depending on *t*, $\vec{r}_1, \vec{r}_2, ...\vec{r}_N$ and $\vec{v}_i$. The second order Runge Kutta or midpoint algorithm and fourth order Runge Kutta Nyström algorithm are employed in the simulations.

The basic idea of second order Runge Kutta algorithm is to use the acceleration at the midpoint of the time step to reduce the first order error in the calculation of the new velocity. Thus for each time step, the acceleration is calculated twice. And for each time step the algorithm is proceeding as following:

$$
\begin{aligned}
&\vec{a}_n = a(t,\vec{r}_n,\vec{v}_n)\\
&\vec{r}_{n+\frac{1}{2}} = \vec{r}_n + \vec{v}_n\frac{\Delta t}{2} + \frac{1}{2}\vec{a}_n\left(\frac{\Delta t}{2}\right)^2\\
&\vec{v}_{n+\frac{1}{2}} = \vec{v}_n + \frac{1}{2}\vec{a}_n\Delta t\\
&\vec{a}_{n+\frac{1}{2}} = a(t+\frac{\Delta t}{2},\vec{r}_{n+\frac{1}{2}},\vec{v}_{n+\frac{1}{2}})\\
&\vec{r}_{n+1} = \vec{r}_n + \vec{v}_{n+\frac{1}{2}}\Delta t\\
&\vec{v}_{n+1} = \vec{v}_n + \vec{a}_{n+\frac{1}{2}}\Delta t
\end{aligned}
\quad , \tag{5.8}
$$

where Δt is the time step used in the MD simulation. In the simulations where the RF field is used, the time step must be less than the RF oscillation period (~100ns), usually the range is from 2ns to 10ns. And for each time step, the error is at the order of Δt^3.In some simulations, the pseudo potential is used, the time step could be chosen that it is larger than the RF oscillation period, less than the secular motion period, it is usually 50ns~200ns. For such a large time step, the fourth order Runge Kutta Nyström algorithm is used. For each time step, the algorithm proceeds as following [71]:

$$
\begin{aligned}
&\vec{a}_n = \vec{a}_1 = a(t,\vec{r}_n,\vec{v}_n)\\
&\vec{a}_2 = a(t+\frac{\Delta t}{2},\vec{r}_n + \vec{v}_n\frac{\Delta t}{2} + \frac{1}{2}\vec{a}_1\left(\frac{\Delta t}{2}\right)^2,\vec{v}_n + \vec{a}_1\frac{\Delta t}{2})\\
&\vec{a}_3 = a(t+\frac{\Delta t}{2},\vec{r}_n + \vec{v}_n\frac{\Delta t}{2} + \frac{1}{2}\vec{a}_1\left(\frac{\Delta t}{2}\right)^2,\vec{v}_n + \vec{a}_2\frac{\Delta t}{2})\\
&\vec{a}_4 = a(t+\Delta t,\vec{r}_n + \vec{v}_n\Delta t + \frac{1}{2}\vec{a}_3\Delta t^2,\vec{v}_n + \vec{a}_3\Delta t)\\
&\vec{r}_{n+1} = \vec{r}_n + \vec{v}_n\Delta t + \frac{1}{6}\Delta t^2(\vec{a}_1 + \vec{a}_2 + \vec{a}_3)\\
&\vec{v}_{n+1} = \vec{v}_n + \frac{1}{6}\Delta t(\vec{a}_1 + 2\vec{a}_2 + 2\vec{a}_3 + \vec{a}_4)
\end{aligned}
\quad . \tag{5.9}
$$

Comparing to the second order Runge Kutta algorithm, the fourth order Runge Kutta Nyström algorithm calculates acceleration four times in one time step, $\vec{a}_1$ at the beginning of the time step, $\vec{a}_2$ and $\vec{a}_3$ at the midpoint of the time step with different velocity consideration, $\vec{a}_4$ at the end of the time step. For each time step, the error is at the order of Δt^5.

5.2.4 Temperature

From Eq. (2.18), the motions of the ions in a RF trap can be treated as two motions: the micro motion and the secular motion. Not only these two motions are running at different time scales with orders of magnitude difference, but also the translational kinetic energy associated with temperature of these two motions are different in the orders of magnitude, especially when the ions are cooled. Usually the secular energy, where the micro motion oscillation is averaged out, can be taken as an indication of the temperature of the ion crystal [40, 42, 72, 73]. The secular velocity is defined by the average over an RF period,

$$\bar{v}_{i\alpha} = \frac{1}{J}\sum_{j=1}^{J} v_{i\alpha}\,, \tag{5.10}$$

where $\alpha = x, y, z$ denotes the coordinates, j is the time step number and J is the total number of time steps in one RF period. Accordingly, the secular temperature of an ion ensemble can be introduced as,

$$T_{\sec} = \frac{2}{3k_B}E_{\sec} = \frac{1}{3Nk_B}\sum_{i=1}^{N} m_i(\langle \bar{v}_{ix}^2 \rangle + \langle \bar{v}_{iy}^2 \rangle + \langle \bar{v}_{iz}^2 \rangle)\,, \tag{5.11}$$

where $\langle\ \rangle$ denotes an average over many RF periods and N is the total ion number.

The micro motion temperature associated with the micro motion can be introduced as,

$$T_{micro} = \frac{2}{3k_B} E_{micro} = \frac{1}{3Nk_B} \sum_{i=1}^{N} m_i (\left\langle \left(v_{ix}^{rms}\right)^2 \right\rangle + \left\langle \left(v_{iy}^{rms}\right)^2 \right\rangle + \left\langle \left(v_{iz}^{rms}\right)^2 \right\rangle), \qquad (5.12)$$

where $(v_{i\alpha}^{rms})^2 = \frac{1}{J} \sum_{j=1}^{J} v_{i\alpha}^2$.

In the case of ion chains as shown in section 4.2.1, the ions are all arranged in a single line on the trap axis, where the micro motion is zero, and the secular motion is zero too. The friction damping force introduced from laser cooling is actually a time averaged force. It already averages out the photon recoil energy to zero from many absorption emission cycles. If there is no stochastic force, the temperature will approach to zero. The simulations also confirmed this particular case, the shape of the MD simulated ion chains look just like the one shown in section 4.2.1. But the temperature approaches zero. Besides this particular case, when ions are off the trap axis, inevitably the RF field is driving them to exhibit micro motions. For a large ensemble of ions, the micro motion kinetic energy could be several orders larger than the secular motion kinetic energy. And the shape of the ion crystal is also very important for the micro motion energy. In the 2D planar mode, the micro motion kinetic energy is much higher than it in the shell modes, mainly because in 2D planar mode, more ions are further away from the trap axis. In Fig. 52 and Fig. 53, the micro motion temperatures are compared with the secular motion temperatures in a shell mode, the simulation is for 100 ions in the RF potential with laser cooling, the initial temperature is corresponding to room temperature at 300 K.

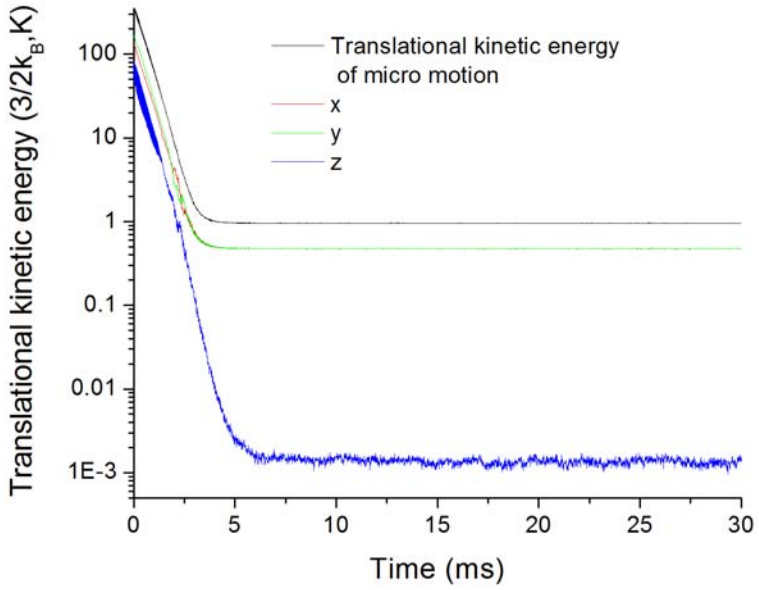

Fig. 52. Micro motion temperature in one simulation. The parameters are: 100 ions, $\alpha \sim$ 0.2, velocity kick magnitude 0.2 m/s, $\beta=3\times10^{-22}$ kg/s.

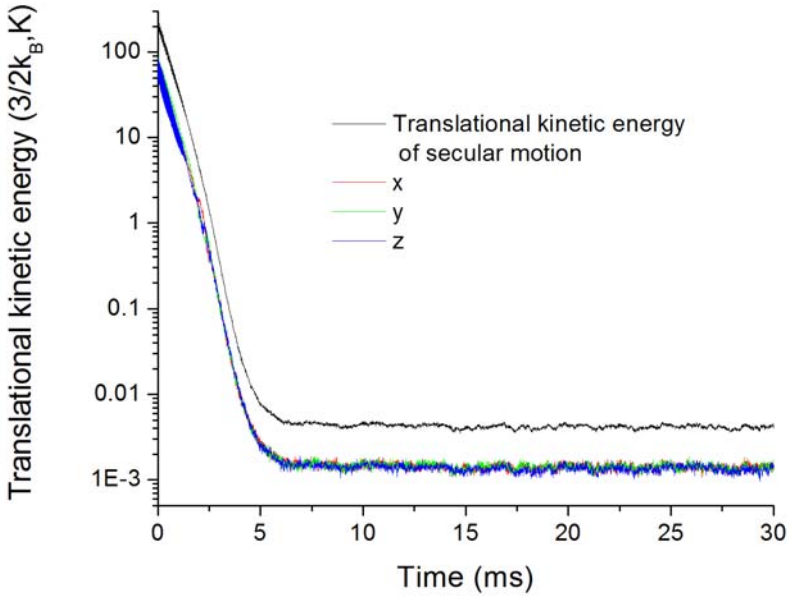

Fig. 53. Secular temperature in one simulation. The parameters are: 100 ions, $\alpha \sim 0.2$, velocity kick magnitude 0.2 m/s, $\beta=3\times10^{-22}$ kg/s.

Also it is found out in the Fig. 52, because of the large micro motion, the *x* and *y*, radial micro motion temperatures are always higher than the *z* direction, axial temperature throughout the cooling process. While for the secular temperature in Fig. 53, both radial and axial temperatures are close in the cooling process.

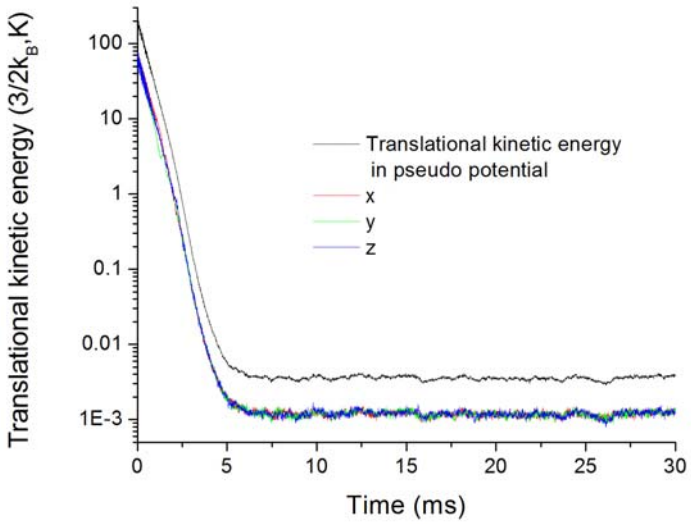

Fig. 54. Kinetic energy in pseudo potential simulation. The parameters are: 100 ions, $\alpha \sim$ 0.2, velocity kick magnitude 0.2 m/s, $\beta=3\times10^{-22}$ kg/s.

Fig. 54 shows the same ion crystal with the same setting of simulation, except that the RF field was replaced by the pseudo potential. Therefore micro motion is not considered directly. The Fig. 54 is quite similar with the Fig. 53, which indicates indeed, that the secular temperature can be taken as ion crystal temperature.

5.2.5 Heating effects

Two major heating effects in the ion trap are the RF heating and the residual gas heating. For a single ion, no energy can be transferred from the RF trapping to the secular motion of the ion, because as the Eq. (2.18) shows, the motion of the ion has

frequency components at ω_s and $\omega_s \pm \Omega$, but not at Ω. However, if a large number of ions are stored, during the collisions, the spectrum of the motion can have an overlap with Ω, thus the ion can gain energy from the RF trapping field. In the experiments, it was found that the RF heating was not detectable for small number of crystallized ions. Under the UHV and low q conditions, the cooling beam can be blocked for tens of seconds, and the crystals are still not melted in a ring trap [74]. But with a high q, the RF heating becomes stronger, especially for the ions are far away from the trap axis, where the fields are stronger and the micro motion amplitudes of the ions are larger.

The residual gas heating refers the kinetic energy transferred by the collisions between the residual gas molecules and trapped ions. This residual gas heating combined with the stray electric field, RF phase shift, etc is taken into the count of the stochastic force in the Eq. (5.1). However, it is hard to get an analytic force form for the stochastic force. In the simulations, a velocity kick model is used to simulate these factors.

For a typical UHV conditions, for the pressure about 10^{-10} mbar H_2, the collision rate calculated with Langevin rate is about $0.3 s^{-1}$ for 100 trapped ions [23, 75, 76], and the velocity kick magnitude is quite large.

Fig. 55 shows the kinetic energies of an ion ensemble of 399 ions and of a single ion, which has a head on collision with a hydrogen molecule of $\frac{3}{2}k_B(300\ \mathrm{K})$ kinetic energy. The simulation used the pseudo potential, therefore there was no micro motion. The colliding ion suddenly gains a large velocity (on the order of 100 m/s) and starts to oscillate in the whole trap volume. Each time when the ion passes through the ion

crystal, it transfers some energy to it. It takes some time (on the order of tenth of ms) for the crystal to reach a new balance.

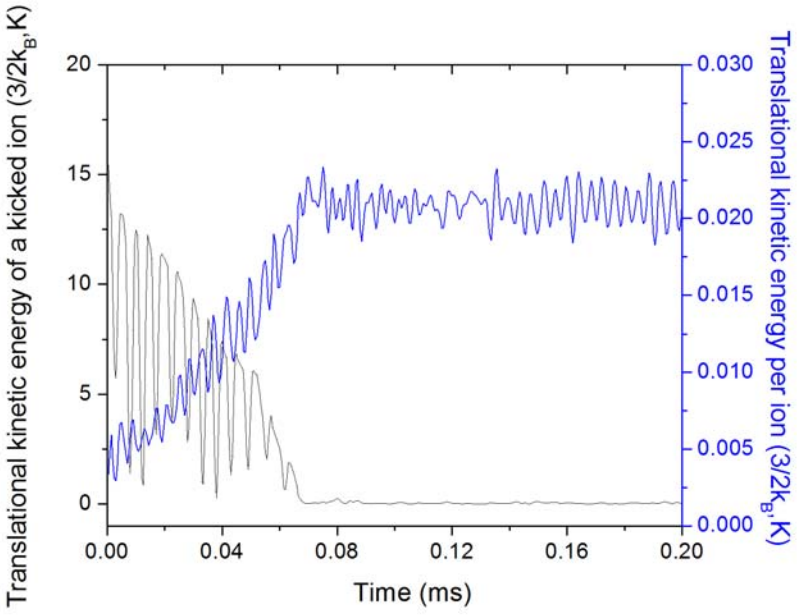

Fig. 55. Ion neutral head on collision.

To make the simulation simple, the velocity kick magnitude is set to be much lower, and it is more frequent, in this way the computation time can be saved because the equilibrium state can be reached faster [42]. Currently in the simulation, every 50RF oscillation ~6 μs, a small magnitude velocity (typical value of 0.5 m/s) kick of random direction imposed to each of the ions.

It is pointed out that the velocity kick model is quite important for the simulation, especially for the final temperature determination of the crystal [42, 23]. By varying the velocity kick magnitude and the value of the viscous friction damping term, the final temperature of the crystal can be varied and compared with the experimental results to extract the reasonable temperatures of the crystals [42]. Still it still remains a difficult

problem to evaluate all these effects with a simple velocity kick model. One research group is using the cold elastic collisions between trapped ions and virtual very light cold atoms to replace the laser cooling force [23]. It indicates reasonable temperatures being reached. However it also largely depends on the simulation conditions.

Fig. 56 provides a view of the velocity kick and RF heating effects. A hundred ions start at room temperature, cooling down to a crystal. Then all the laser cooling term and the velocity kick term are shut off at about 13 ms, the ion crystal remains at the same low temperature. This indicates that the RF heating is not detected during this process. At about 63 ms, the velocity kick term turns on, and with this the temperature of ion crystal increases gradually. When the temperature is in the range of 1~10 K, the temperature starts to increase drastically and oscillations build up, which indicates that the RF heating starts to affect the ions. This behavior agrees with the previous results on RF heating research that it has a high hat at from 5K to 15K [22, 77].

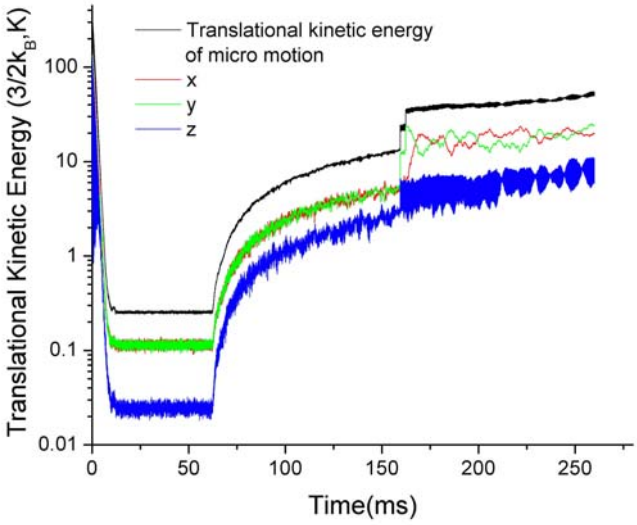

Fig. 56. Velocity kick and RF heating effects.

5.2.6 Cooling effect

According to Eq. (2.35), the laser cooling force is treated as a linear viscous damping force plus a constant light pressure force,

$$F = F_0 - \beta v \tag{5.13}$$

The direction of the force is along the propagation direction of laser beam. The light pressure force just pushes the laser cooled ions and creates a spatial offset from the trap center to the crystal center. If the electric field confinement of the trap is strong, which is the usual case, this offset is very small. The viscous damping force reduces the velocities of the laser cooled ions. The maximum of friction coefficient β is about $\sim 1.3\times10^{-20}$ kg/s for the cooling transition. In the simulation the value could be chosen to be one magnitude lower than the maximal value to simulate the more common situations [40, 42]. In most of the atom traps, three pairs of mutually orthogonal laser beams are used. But in ion trap, cooling with only one laser beam oblique to the trap axis is sufficient to reduce the secular motion of the ions in all directions. This is due to the coupling of the motions [78].

From Fig. 57 to Fig. 59 a comparison of the secular temperatures in the cooling process provided for the following situation, three orthogonal laser beams cooling from 100 K, one oblique beam cooling from 100 K, one collinear beam cooling from 10 K. For all the laser beams, the same radiation pressure force and viscous damping term is used. And the oblique beam has a 15º angle with the trap axis, which is described in the Chapter III as the cross beam.

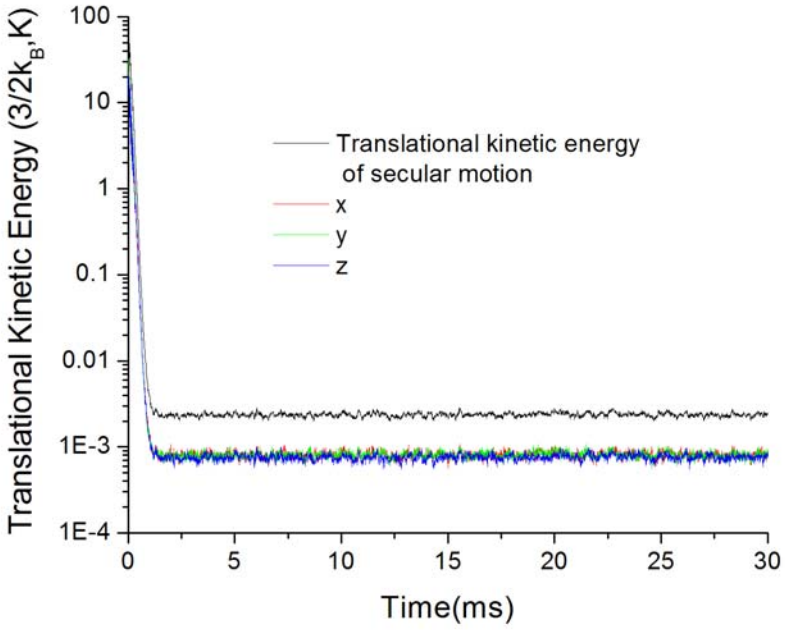

Fig. 57. Simulation of laser cooling with three orthogonal beams. The parameters are: 100 ions, $\alpha \sim 0.2$, velocity kick magnitude 0.2 m/s, $\beta=1.0\times10^{-21}$ kg/s.

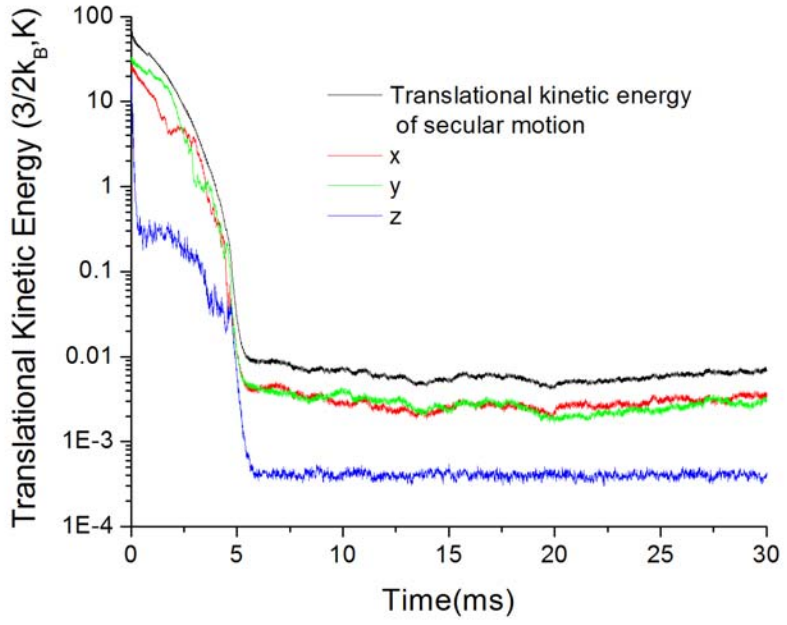

Fig. 58. Simulation of laser cooling with an oblique beam. The parameters are: 100 ions, $\alpha \sim 0.2$, velocity kick magnitude 0.2 m/s, $\beta=1.0\times10^{-21}$ kg/s.

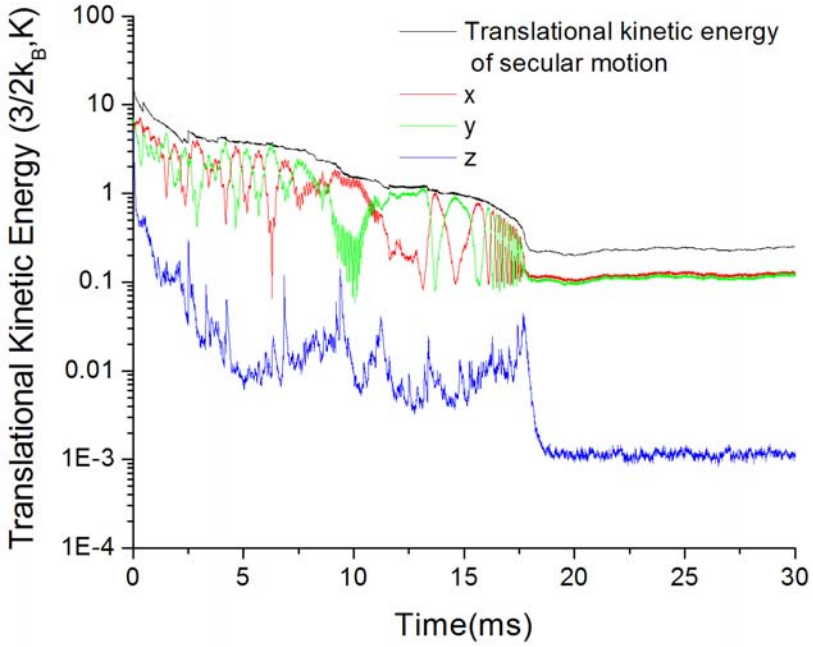

Fig. 59. Simulation of laser cooling with a collinear beam. The parameters are: 100 ions, $\alpha \sim 0.2$, velocity kick magnitude 0.2 m/s, $\beta=1.0\times10^{-21}$ kg/s.

The maximal laser cooling damping friction term β is about 1.3×10^{-20} kg/s, the actual number being used for this simulation is about 1.0×10^{-21} kg/s. For the Fig. 57 and Fig. 58, the initial velocity assignment of the ions corresponding to a temperature about 100 K, and the final balanced temperatures of three orthogonal beams and one oblique beam are within the same magnitude. It is also found out, that if the temperature is higher, such as 300 K at room temperature, for three beams case, there is not much difference. But for the 15º oblique beam, with 300 K initial conditions, several ions are not cooled in the crystals, they continue to fly around, and their velocities are several magnitude larger than the crystallized ones. As a consequence, the average temperature could not represent the ion crystal temperature. It is the same situation for the collinear

beam to cool ions at 100 K. Most likely, it is because the RF heating is quite large for the high temperature, if there is no directed cooling in all dimensions, the thermal stabilization by Coulomb interactions takes a very long time, probably minutes as observed in experiments, such durations correspond to 10^8 or more RF periods, and can not be simulated when ion numbers are large. For the initial temperature at 10 K, RF heating is much weaker, the ions cool down by two magnitude and form a crystal, but the final temperature is still about two magnitude higher than the other two as Fig. 59 shows. It is because the radial micro motions of the ions still somehow affect the secular motions, and the Coulomb interactions betweens the ions did not thermalize the kinetic energy in all directions evenly in a short RF period. Thus to save the computation time, this assumption was made, that there are the same small damping coefficients for all three directions, and many simulations are using this assumption [40, 42, 67, 72].

5.3 Structure phase transition simulation of ion crystals

The simulations of the shape of the ion crystals were carried out and compared with the experimental results. The results are quite similar to the experimental observations, as shown in Fig. 60. Different ion numbers from 10, 15, 20 to 30 were simulated under the same condition with α=0.02 to compare with the experimental results of Fig. 37. Also it provides some interesting views to the experimental results. First the radiation pressure does push the ion crystal in the beam propagating direction off the trap center, which is hard to confirm for pure ion crystals. The simulation parameters, such as RF voltage and DC voltage, could be compared with the

experimental results. For the endcap voltage there is a geometry factor. It can also be compared with the theoretical calculations. Also the simulation parameters were changed to fit the trap parameters of our Japanese collaborators' trap, and the simulation result matched their experimental results and simulations quite well [23].

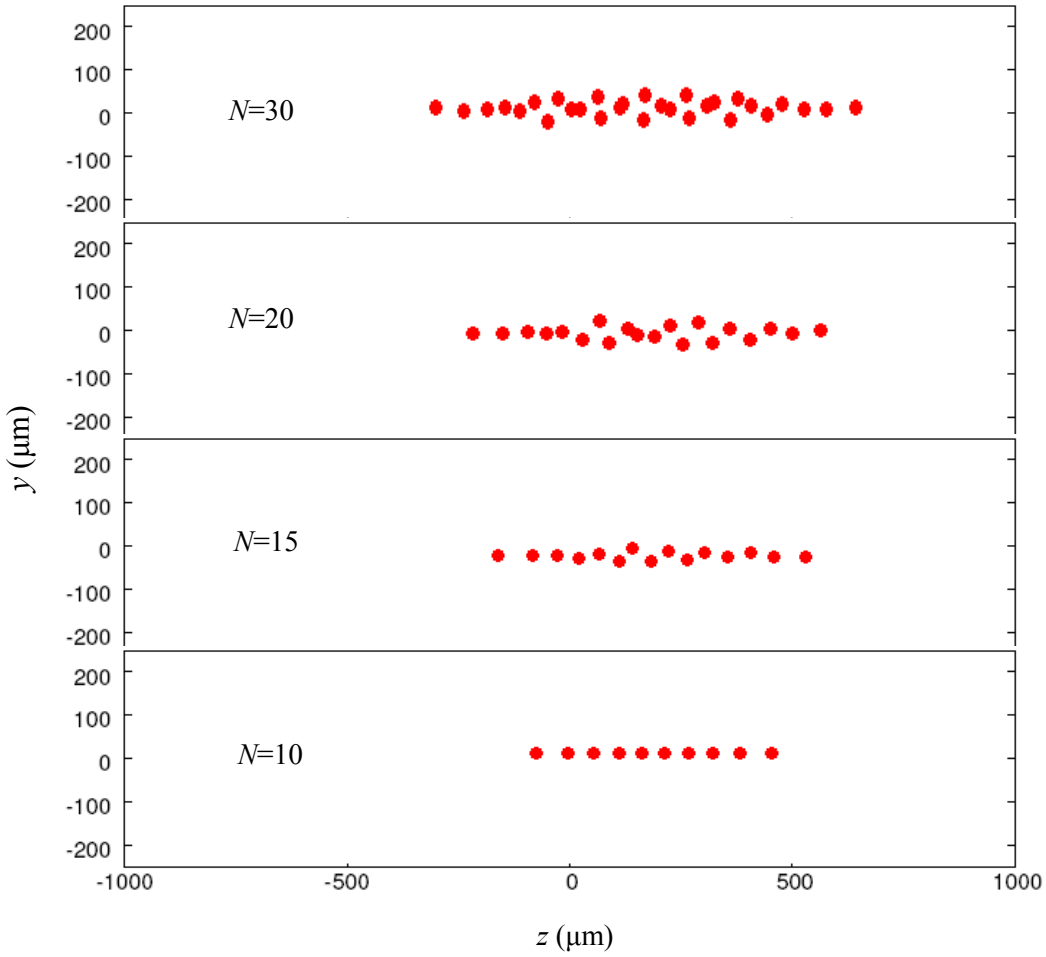

Fig. 60. Simulations of the ion crystal structure phase transition at constant α. (α~0.02).

Fig. 61 provides simulations of 30 ions with different α. When the axial confinement end cap DC voltage is large, the ion crystal goes to the 2D planar disk

mode. And because of this large electric potential, the offset of radiation pressure force is almost invisible compared to the weak end cap confinement.

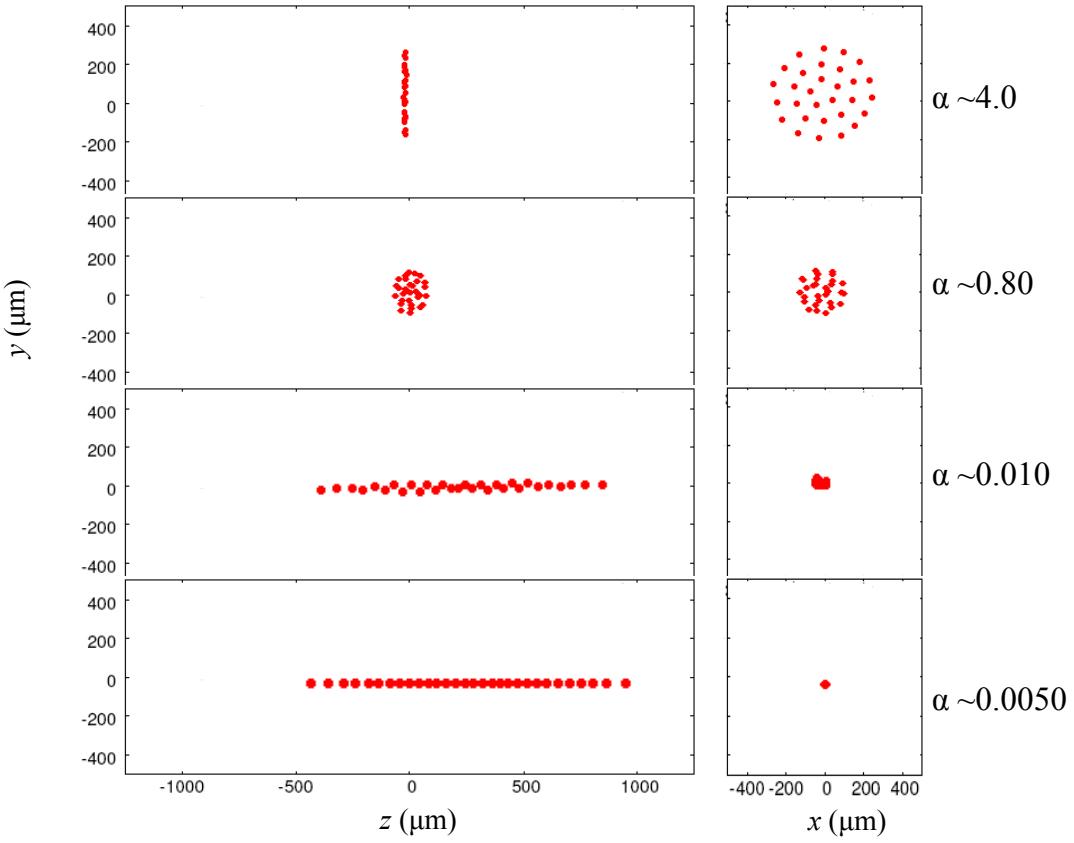

Fig. 61. Simulations of 30 ions with different α.

5.4 Large ion crystal simulation

Although experimentally, the recording of a sharp large number ion crystal image is quite challenging in our trap, simulations with large ion crystals are carried out to give a hint what these crystals should look like. For these large ion number crystals, the simulations use the pseudo potential and the large time step (about 50 ns), it takes

about six hours to calculate the ion ensemble of 1000 ions with the Supercomputer with CUDA cards in our laboratory.

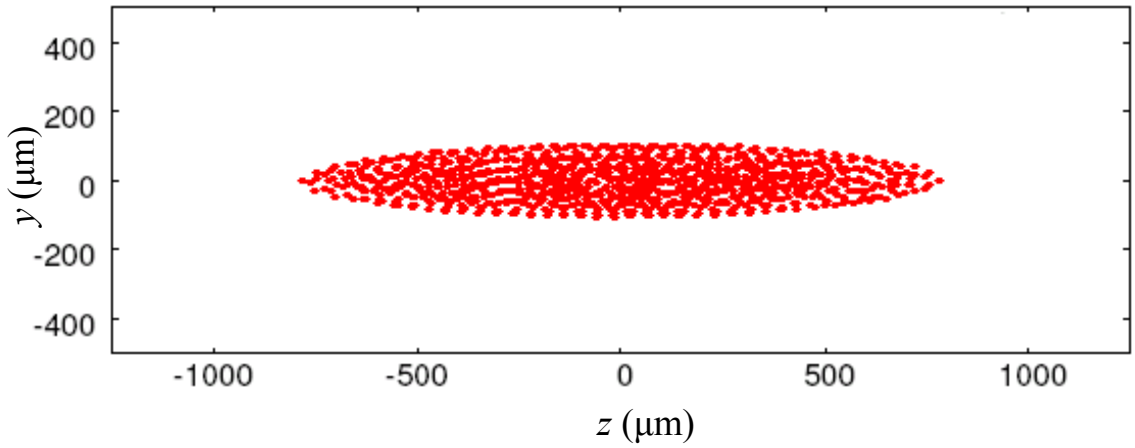

Fig. 62. Simulation of a large ion crystal. (N=1000, α~0.2).

5.5 Sympathetic cooling simulation

The MD simulation can straightforwardly extend to study the sympathetic cooling process and to compare with the experimental results. Various simulations are carried out to compare with the experimental results. In Fig. 62, the simulations of 20 ions of $^{4}He^{+}$ sympathetically cooled by 80 ions of $^{24}Mg^{+}$ under different DC axial confinement are compiled.

To avoid the large RF heating for the light ions, especially considering the high q value for the $^{4}He^{+}$ in this case, the initial temperature of the $^{4}He^{+}$ is chosen to be low at 20 K. In simulations, it is found out that if the initial temperature of the He^{+} is higher, such as 100 K, even though most of the $^{4}He^{+}$ are trapped and cooled in the mixed crystal, a few ions could be left out, they usually have a very large velocity compared with those

sympathetically cooled ones, which makes the average translational kinetic energy much bigger and doesn't represent the sympathetically cooled ions. Experimentally, such low temperature initial conditions are achieved by the cryogenic techniques [28, 29].

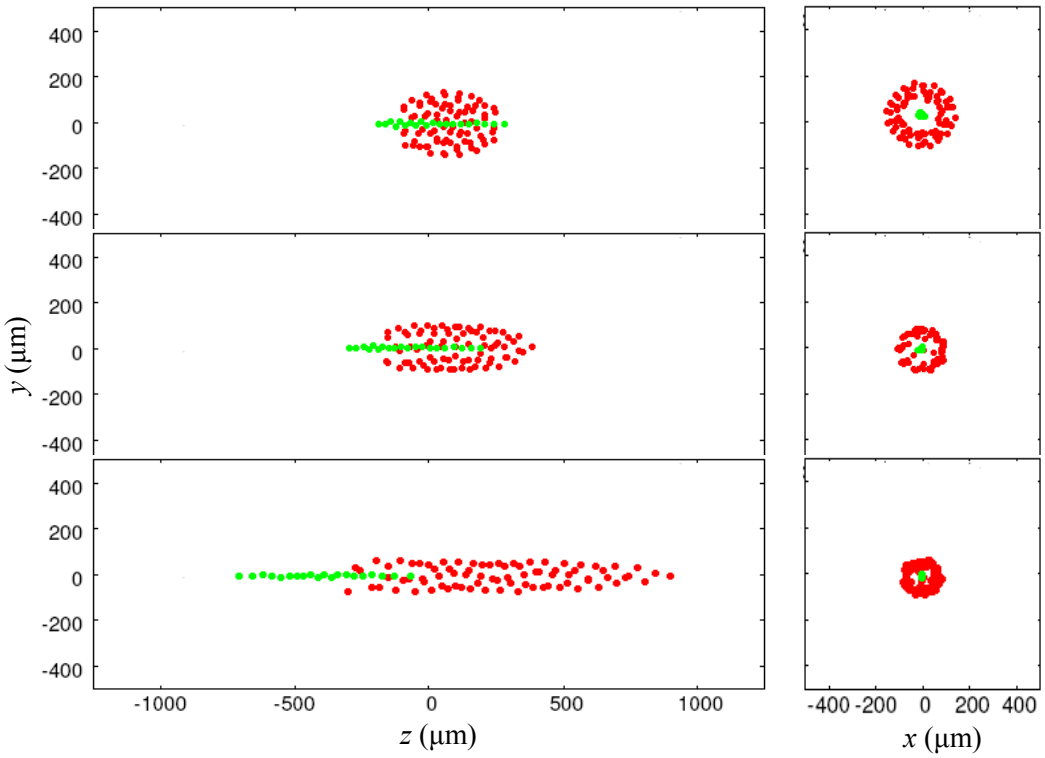

Fig. 63. Simulations of $^{4}He^{+}$ and $^{24}Mg^{+}$ mixed ion crystals.

In Fig. 63, from top to bottom, $\alpha \sim 0.02$, 0.12, and 0.20 for $^{24}Mg^{+}$, the corresponding experimental images are depicted in Fig. 43.

In Fig. 64, the temperatures of the mixed crystal during the cooling process are plotted. Because the $^{4}He^{+}$ is trapped and sympathetically cooled near the trap axis, the micro motion temperature of $^{4}He^{+}$ ions is actually smaller than $^{24}Mg^{+}$.

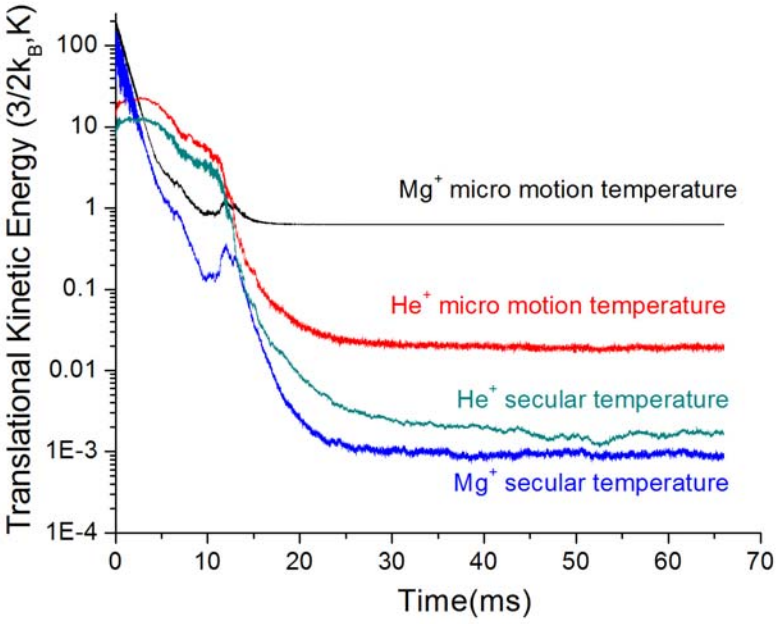

Fig. 64. Temperatures of a simulated $^{4}He^{+}$ and $^{24}Mg^{+}$ mixed ion crystal.

For the fullerene ions, simulations are carried out to see how effectively the $^{24}Mg^{+}$ sympathetically cool the heavy molecular ions. Fig. 65 shows the mixed crystal of 80 ions of $^{24}Mg^{+}$ and 20 heavy ions, which is about the 144 amu for singly charged ions. If considering the charge to mass ratios, it is corresponding to highly charged C_{60}^{5+} ions. And $\alpha \sim 0.004$ for $^{24}Mg^{+}$.

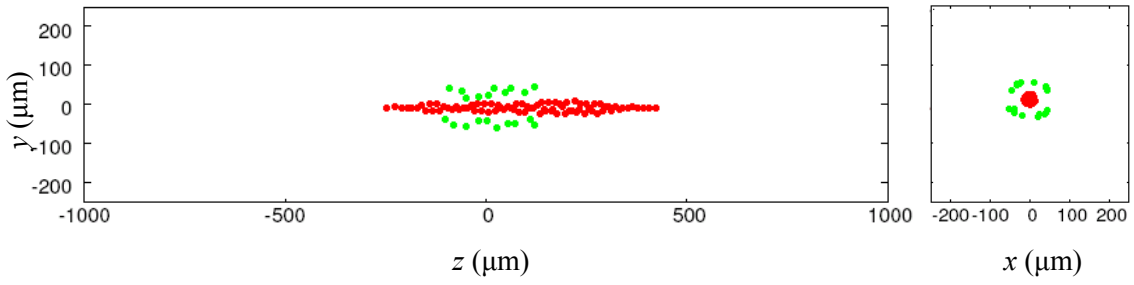

Fig. 65. Simulation of a C_{60}^{5+} and $^{24}Mg^{+}$ mixed ion crystal.

In the simulation, the initial temperature of $^{24}Mg^{+}$ was set at 200 K, and the initial temperature of C_{60}^{5+} was set at 100 K. The temperatures of the mixed crystal during the cooling process are plotted in Fig. 66.

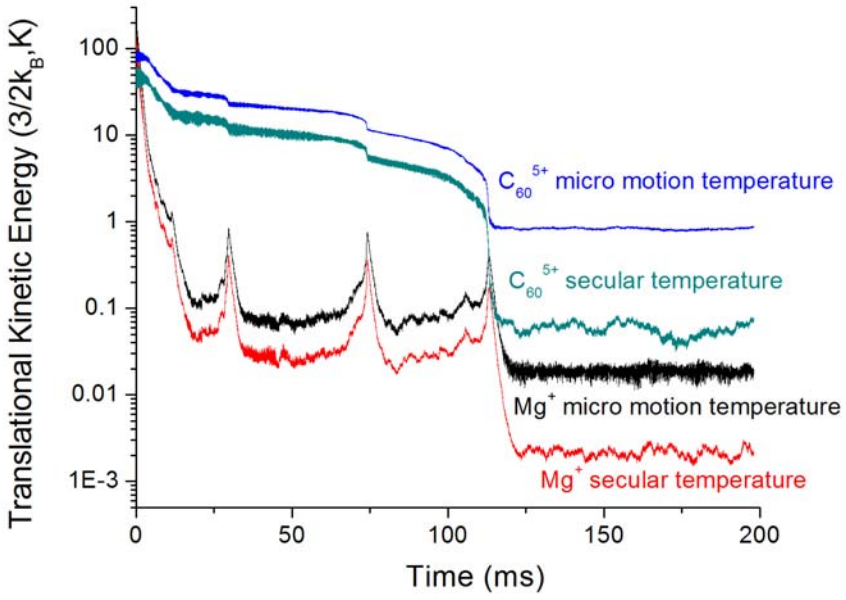

Fig. 66. Temperatures of a simulated C_{60}^{5+} and $^{24}Mg^{+}$ mixed ion crystal.

When the charge gets fewer for the fullerene ion, which corresponds to a heavier mass singly charged ion, the sympathetic cooling strength is lower. Simulation shows that the secular temperature of C_{60}^{5+} is the largest charge to mass ratio to get below 200 mK, which is usually considered that the ions are crystallized [79].

Fig. 67 shows the temperatures of simulated C_{60}^{+} and Mg^{+} mixed clouds. In the simulation, the initial temperature of $^{24}Mg^{+}$ was set at 200 K, and the initial temperature of C_{60}^{+} was set at 100 K.

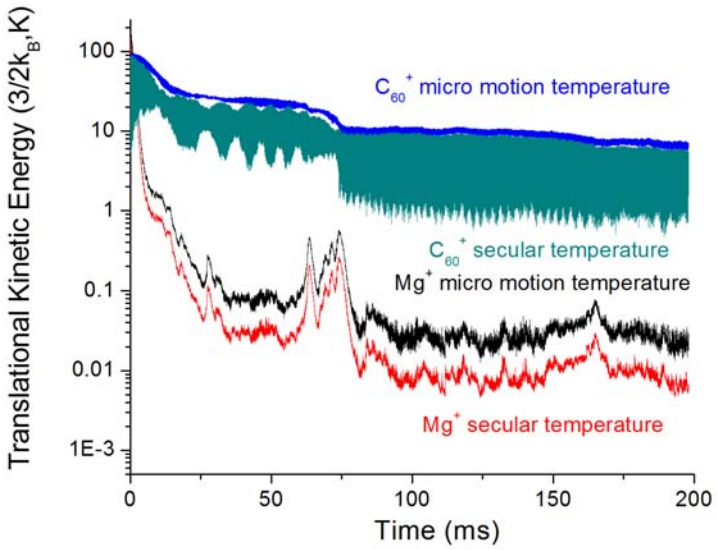

Fig. 67. Temperatures of a simulated C_{60}^+ and $^{24}Mg^+$ mixed cloud.

Both micro motion and secular temperature of C_{60}^+ dropped from 100 K to around 10 K, which is in the same magnitude with the experimental result and the previous simulation result [22, 46].

CHAPTER VI

ION CRYSTALS COOLED BY A LAGUERRE-GAUSSIAN BEAM

The Laguerre-Gaussian beam is a laser beam which possesses orbital angular momentum (OAM) and it has been predicted that such a light beam may be able to rotate particles with which it interacts [80]. Experiments are being made to detect this effect and measure it [81]. It is our near term goal to see if the Laguerre-Gaussian beam rotate the ion crystals in the ion trap. In this chapter, the basic of Laguerre-Gaussian beam will be introduced, the preliminary experimental results will be shown, and the simulations of the rotation of the ion crystals will be discussed.

6.1 Laguerre-Gaussian beam

Electromagnetic fields in free space (or in any uniform and isotropic medium) are governed in general by the scalar Helmholtz equation [82],

$$(\nabla^2 + k^2)E(x,y,z) = 0. \tag{6.1}$$

By using the paraxial approximation $\left|2k\frac{\partial E}{\partial z}\right|$ or $\left|\frac{\partial^2 E}{\partial x^2}\right|$ or $\left|\frac{\partial^2 E}{\partial y^2}\right| >> \left|\frac{\partial^2 E}{\partial z^2}\right|$, which assumes the amplitude of the field varies slowly in the z direction and using $E = Ee^{ikz}$, the scalar Helmholtz equation is:

$$\frac{\partial^2 E}{\partial x^2} + \frac{\partial^2 E}{\partial y^2} + 2ik\frac{\partial E}{\partial z} = 0. \tag{6.2}$$

Eq. (6.2) is known as the paraxial wave equation.

The solution of the paraxial wave equation in Cartesian coordinates gives the Hermite-Gaussian modes. In the cylindrical coordinates, the solutions are the Laguerre-Gaussian modes [82].

Using the trial solution,

$$E(x,y,z)=\frac{w_0}{w}f(x,y,z)\exp(\frac{ikr^2}{2R}), \tag{6.3}$$

where *f(x,y,z)* is an unknown transverse spatial distribution. By making the substitutions $x=w\xi/\sqrt{2}$, $y=w\eta/\sqrt{2}$ and $t=\arctan(z/z_0)$, and inserting into Eq. (6.2), it just gives the Schrödinger equation for the two dimensional harmonic oscillators in Cartesian coordinates:

$$(\partial_{\xi\xi}+\partial_{\eta\eta}-\xi^2-\eta^2+2i\partial_t)f=0. \tag{6.4}$$

The solutions upon substituting back to *x*, *y* and *z* are [82]:

$$HG_{nm}(x,y,z)=\frac{w_0}{w}H_n(\frac{\sqrt{2}x}{w})H_m(\frac{\sqrt{2}y}{w})\exp(-\frac{r^2}{w^2})\exp(\frac{ikr^2}{2R})e^{-i(n+m+1)\varphi(z)}e^{ikz}, \tag{6.5}$$

where H_n are the Hermite polynomials, *n* is the mode number in *x* direction, and *m* is the mode number in *y* direction.

The Laguerre-Gaussian modes are found by writing the Laplace operator of Eq.(6.4) in cylindrical coordinates,

$$(\partial_{\varepsilon\varepsilon}+\frac{1}{\varepsilon}\partial_\varepsilon+\frac{1}{\varepsilon^2}\partial_{\theta\theta}+\varepsilon^2+2i\partial_t)f=0. \tag{6.6}$$

The solutions to Eq. (6.6) are [83]:

$$LG_p^l(r,\theta,z)=\frac{w_0}{w}(\frac{\sqrt{2}r}{w})^{|l|}L_p^{|l|}(\frac{2r^2}{w^2})\exp(-\frac{r^2}{w^2})\exp(\frac{ikr^2}{2R})e^{-i(2p+|l|+1)\varphi(z)}e^{ikz}e^{il\theta}, \tag{6.7}$$

where $L_p^{|l|}$ are the associated Laguerre polynomials with radial mode number p and azimuthal mode number l. The solutions have multiple rings with p radial nodes and a phase dependence of $e^{il\theta}$. They have an azimuthal phase that gives rise to a spiral staircase structure with intertwined spirals. All Laguerre Gaussian modes having a nonzero azimuthal mode number $l \neq 0$ possess a vortex core (central dark spot of zero intensity). The vortex is the results of the phase being undetermined at the center [83].

A light beam with a phase singularity, e.g., a Laguerre-Gaussian beam, has a well defined OAM along its propagation axis. The amount of OAM takes discrete values equal to $l\hbar$ per photon [84].

6.2 Preliminary experimental results

When light interacts with matter, inevitably it involves the exchange of momentum. For linear momentum, laser Doppler cooling is a good example of the linear momentum transferred from a photon to a two level system atom or ion. For spin angular momentum, the mechanical effect on macroscopic matter was observed in an experiment where circularly polarized light rotated a birefringent plate [85]. For OAM, the mechanical effects on microscopic particles and atoms have been investigated [86]. It is of interest to see if the OAM could be transferred from the photon to the ion crystals in the ion trap, or in other words, to see if the Laguerre-Gaussian beam can rotate the ion crystals.

Laguerre Gaussian modes of the cooling beam were generated with a laser etched grating [83]. After two cylindrical lens shape the UV beam profile, the UV beam is

reflected by a flip mirror, incident on the laser etched grating. The diffraction patterns are shown as Fig. 68.

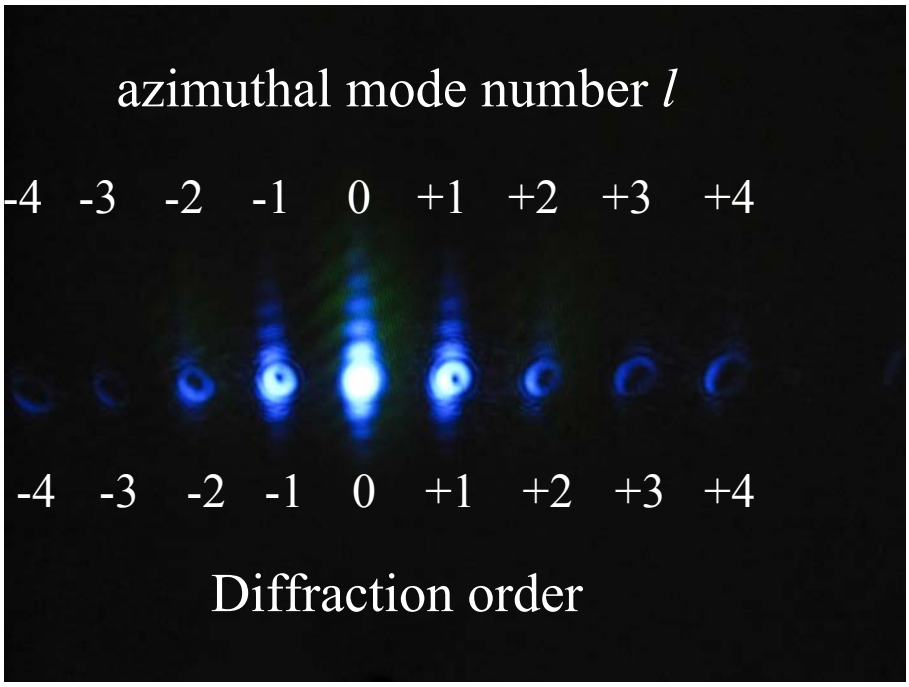

Fig. 68 Generated Laguerre-Gaussian beams.

The first order of the diffraction beam, which corresponds to $l = 1$ and $p = 0$ LG_0^1 mode, was directed into the trap and interacted with ion crystals. Unfortunately, the most favorable 2D planar mode of the ion crystals has not yet been produced in the trap. For the other crystal structure, there was no difference detected between the Lagurre-Gaussian beam and Hermit-Gaussian beam with the current image resolutions.

When the Lagurre-Gaussian beam was directed at the cross beam position, it was found that both ends of the ion chain were laser cooled, while the middle of the ion chain

was sympathetically cooled, as show in Fig. 69. It is a good starting point for the study of the ion chain dynamics.

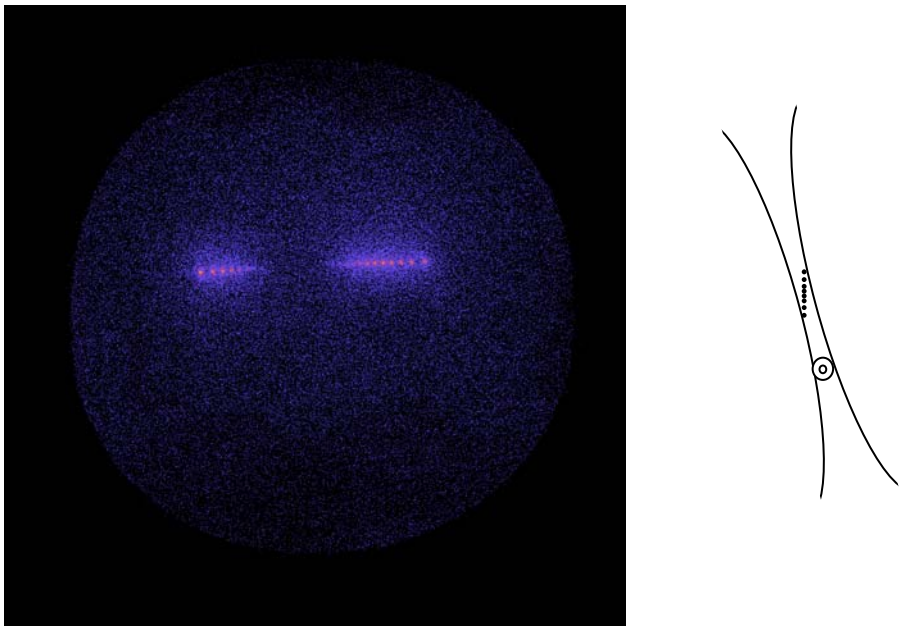

Fig. 69 Cross beam cooling with a Laguerre-Gaussian beam.

6.3 Simulations of ion crystals rotated by a Laguerre-Gaussian beam

The MD simulations with Lagurre-Gaussian beams are straightforward, just needs to reevaluate the force with the Lagurre-Gaussian beam instead of the Hermit-Gaussian beam. Very similar to Eq. (2.34), the force can be written as [80]:

$$\vec{F} = \hbar\vec{\nabla}\theta \frac{nG_{n,m}^2\gamma}{\gamma^2 + 2nG_{n,m}^2 + 4(\Delta - kv)^2}, \tag{6.8}$$

where in cylindrical coordinate,

$$\vec{\nabla}\theta = -\left(\frac{kr}{R}\right)\hat{e}_r - \left(\frac{l}{r}\right)\hat{e}_\phi - \left[k - \frac{1}{2}\frac{kr^2}{z^2+z_0^2}\left(\frac{2z^2}{z^2+z_0^2}-1\right) + \frac{(n+m+1)z_0}{z^2+z_0^2}\right]\hat{e}_z . \qquad (6.9)$$

By making the approximation $z_0 \to \infty$, which implies $R \to \infty$ and $w \to w_0$, and converting it to the Cartesian coordinates, using $s = 2nG_{n,m}^2/\gamma^2$, the force is:

$$\vec{F} = \hbar\frac{s\gamma/2}{1+s+4(\Delta - k_z v_z)^2/\gamma^2}\left(\frac{ly}{x^2+y^2}\hat{e}_x - \frac{lx}{x^2+y^2}\hat{e}_y - k_z\hat{e}_z\right). \qquad (6.10)$$

Let $\Delta = -\gamma/2$ and *s*=2, which are same parameters we chose for in Chapter II, the force can be expanded in the order of v_z. Only taking the first two orders, then the force is:

$$\vec{F} = \frac{1}{4}(\hbar k_z\gamma - \hbar k_z^2 v_z)\left(\frac{ly}{k_z(x^2+y^2)}\hat{e}_x - \frac{lx}{k_z(x^2+y^2)}\hat{e}_y + \hat{e}_z\right). \qquad (6.11)$$

As expected, if *l*=0, the force is the same with Eq. (5.7), as the beam propagates along the *z* direction.

Using Eq. (6.11), the simulation is performed in the trap of Ref. 23, in which the 2D planar mode of ion crystal was observed. The simulation is carried out as following. First a 2D planar mode of ion crystal (*N*=30, α~4.0) was generated, then all the ions were frozen to zero temperature. At time zero, a Hermit-Gaussian (0,0 mode) beam and a Laguerre-Gaussian (0,1 mode), which propagate along the trap axis start to interact with the disk mode of ion crystal. The intensity of ratio of Hermit-Gaussian beam and Laguerre-Gaussian beam set at 10:1, and for the Hermit-Gaussian beam, *s*=2. To match the diameter of the 2D planar ion crystal, the beam waist is set at ~300 μm for Hermit-

Gaussian, and inner diameter is ~30 μm and out diameter is ~300 μm for the the Laguerre-Gaussian beam. The result is shown in Fig. 70.

One ion labeled green was tracked in Fig. 70. Clearly it is rotating in the counter clockwise direction with the ion crystal. Each row has the same time interval. In the first row, the green ion slowly starts to rotate. In the second row, the ion takes a pace of two ion spots. In the third row, the ion takes a pace of about four ion spots. And if the l=1 changed to l=-1, the simulation shows the ion crystal rotates in the clockwise direction with about the same angular speed.

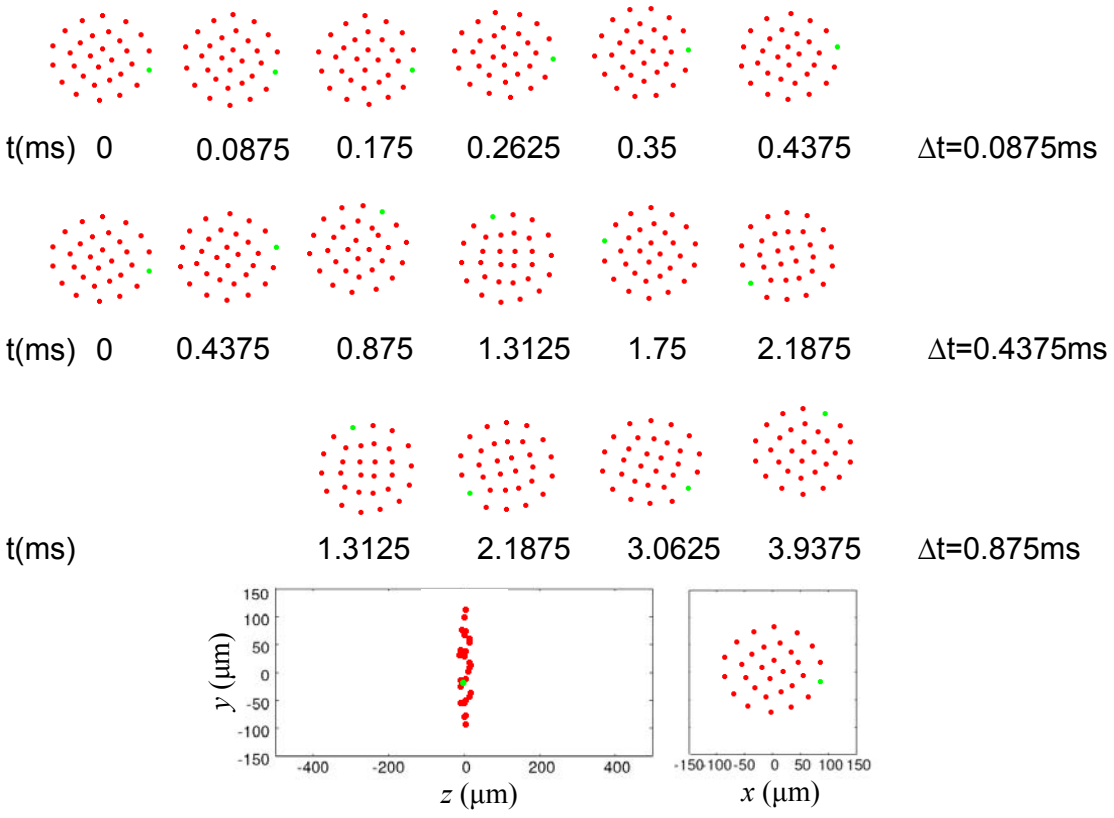

Fig. 70. Simulation of an ion crystal rotated by a Laguerre-Gaussian beam.

CHAPTER VII

SUMMARY AND RECOMMENDATIONS

An investigation of the ion crystals produced by laser and sympathetic cooling in a linear RF ion trap has been conducted.

The ultimate goal is to conduct the laser spectroscopy on various species. With this in mind, the ion trap apparatus was modified and expanded. New elements were added on the trap to provide better manipulations of the trapped ions. Two SHG cavities were built to provide reliable laser sources for the photonionization and cooling of $^{24}Mg^{+}$ ions. The imaging system was reconfigured and used to take images of single ions.

The laser cooling techniques were examined and applied to the trapped $^{24}Mg^{+}$ ions. The crystals produced by the laser cooling was studied systematically, including the RF voltage, endcap DC voltage, laser power and laser frequency. By manipulating the different RF voltage and endcap DC voltage, the structure phase transition of the ion crystals was studied.

Sympathetic cooling of different ion species with the laser cooled $^{24}Mg^{+}$ was carried out. Mixed $^{24}Mg^{+}$ and $^{4}He^{+}$ ion crystals were created and identified, and mixed Mg^{+} and H_2^{+} ion crystals were created, and the effect of the chemical reaction of Mg and H_2 has been shown. The sympathetic cooling of heavy molecular ions such as fullerene ions has been carried out, and the achieved cooling temperature of C_{60}^{+} is about ~10 K.

The MD simulations of the laser cooling and sympathetic cooling were implemented. The simulation model was discussed in detail. And the simulation results were compared with the experimental results.

The largest advantage for this trap is its large size of the center segments. This not only provides the ability to trap millions of ions, also under the weak axial confinement, the single ions have a large distance between them. It might provide a unique opportunity to study the ion chain dynamics. For example, the collinear beam can be used to cool the ion chain, while the 15º cross beam can be used to heat part of the ion chain. Depending on the heating and cooling power, the ions could show different oscillations, and extend the single ion phonon laser [87, 88], to a multi ion photon laser. Also, it is of interest to study if the oscillations of the ions propagate in the ion chain, or in other words, display a conductivity of this particular ion chain system, which is very large.

Another interesting idea is to continue to investigate the effects of the Laguerre Gaussian beam on the ion crystals. To pave the way, the simulations were carried out on this topic. The results are encouraging that the Laguerre-Gaussian beam does rotate the ion crystals in the simulations. However, to successfully carry out these experiments, a 2D planar disk mode of ion crystal is more favorable, which has not been produced in our trap yet. Because the ion crystals formed by the linear RF trap usually have a cylindrical symmetry, it remains a challenge to observe this effect.

REFERENCES

[1] W. Paul, O. Osberghaus, and E. Fischer, *Forschungsberichte des Wirtschaft und Verkehrministeriums Nordrhein Westfalen* (Westdeutscher Verlag, Koln, 1958), No. 415.

[2] W. Paul, Rev. Mod. Phys. **62**, 531 (1990).

[3] W. Neuhauser, M. Hohenstattt, P. Toschek, and H. Dehmelt, Phys. Rev. Lett. **41**, 233 (1978).

[4] D. J. Wineland, R. E. Drulinger, and F. L. Walls, Phys. Rev. Lett. **40**, 1639 (1978).

[5] H. A. Schuessler, in *Progress in Atomic Spectroscopy*, edited by W. Hanle and H. Kleinpoppen (Plenum Publishing Company, New York, 1979), pp. 999-1029.

[6] G. Z. K. Horvath, R. C. Thompson, and P. L. Knight, Contemp. Phys. **38**, 25(1997).

[7] F. Diedrich, E. Peik, J. M. Chen, W. Quint, and H. Walther, Phys. Rev. Lett. **59**, 2931 (1987).

[8] P. O. Schmidt, T. Rosenband, C. Langer, W. M. Itano, J. C. Bergquist, and D. J. Wineland, Science **309**, 749 (2005).

[9] M. Herrmann, V. Batteiger, S. Knünz, G. Saathoff, Th, Udem, and T. W. Hänsch, Phys. Rev. Lett. **102**, 013006 (2009).

[10] T. Rosenband, D. B. Hume, P. O. Schmidt, C. W. Chou, A. Bruch, L. Lorini, W. H. Oskay, R. E. Drullinger, T. M. Fortier, J. E. Stalnaker, S. A. Diddams, W. C. Swann, N. R. Newbury, W. M. Itano, D. J. Wineland, and J. C. Bergquist, Science, **319**, 1808 (2008).

[11] H. A. Schuessler, Metrologia, **7**, 103 (1971).

[12] D. Leibfried, B. Demarco, V. Meyer, D. Lucas, M. Barrett, J. Britton, W. M. Itano, B. Jelenkovic, C. Langer, T. Rosenband, and D. J. Wineland, Nature **422**, 412 (2003).

[13] F. Schmidt-Kaler, H. Häffner, M. Riebe, S. Gulde, G. P. T. Lancaster, T. Deuschle, C. Becher, C. F. Roos, J. Eschner, and R. Blatt, Nature, **422**, 408 (2003).

[14] R. Blatt and D. Wineland, Nature **453**, 1008 (2008).

[15] J. I. Cirac and P. Zoller, Phys. Rev. Lett. **74**, 4091 (1995).

[16] D. Offenberg, C. B. Zhang, Ch. Wellers, B. Roth, and S. Schiller, Phys. Rev. A **78**, 061401(R) (2008).

[17] P. F. Staanum, K. Højbjerre, R. Wester, and M. Drewsen, Phys. Rev. Lett. **100**, 243003 (2008).

[18] M. Herrman, M. Haas, U. D. Jentschura, F. Kottmann, D. Leibfried, G. Saathoff, C. Gohle, A. Ozawa, V. Batteiger, S. Knünz, N. Kolachevsky, H. A. Schuessler, T. W. Hänsch, and Th. Udem, Phys. Rev. A **79**, 052505 (2009).

[19] K. Højbjerre, D. Offenberg, C. Z. Bisgaard, H. Stapelfeldt, P. F. Staanum, A. Mortensen, and M. Drewsen, Phys. Rev. A **77**, 030702(R) (2008).

[20] D. H. E. Dubin, Phys. Rev. Lett. **71**, 2753 (1993).

[21] X. Zhao, Ph.D. dissertation, Texas A&M University, 2001.

[22] V. Ryjkov, Ph.D. dissertation, Texas A&M University, 2003.

[23] K. Okada, M. Wada, T. Takayanagi, S. Ohtani, and H. A. Schuessler, Phys. Rev. A **81**, 013420 (2010).

[24] E. Moreno and D. Balomir, IEE Proc. **127**, A, 399 (1980).

[25] F. M. Penning, Physica **3**, 873 (1936).

[26] L. S. Brown and G. Gabrielse, Rev. Mod. Phys. **58**, 233 (1986).

[27] H. G. Dehmelt, Adv. At. Mol. Phys. **3**, 53 (1967).

[28] M. E. Poitsch, J. C. Bergquist, W. M. Itano, and D. J. Wineland, Rev. Sci. Instrum. **67**, 129 (1996).

[29] K. Okada, M. Wada, T. Nakamira, I. Katayama, L. Boesten, and S. Ohtani, Jpn. J. Appl. Phys. **40**, 4221 (2001).

[30] D. Leibfried, R. Blatt, C. Monroe, and D. Wineland, Rev. Mod. Phys. **75**, 281 (2003).

[31] R. E. Drullinger, D. J. Wineland, and J. C. Bergquist, Appl. Phys. **22**, 365 (1980).

[32] D. J. Larson, J. C. Bergquist, J. J. Bollinger, W. M. Itano, and D. J. Wineland, Phys. Rev. Lett. **57**, 70 (1986).

[33] T. W. Hänsch and A. L. Schawlow, Opt. Commun. **13**, 68 (1975).

[34] D. J. Wineland and W. M. Itano, Phys. Rev. A **20**, 1521 (1979).

[35] F. Diedrich, J. C. Bergquist, W. M. Itano, and D. J. Wineland, Phys. Rev. Lett. **62**, 403 (1989).

[36] H. J. Metcalf and P. van der Straten, *Laser Cooling and Trapping* (Springer, New York, 1999).

[37] M. O. Scully and M. S. Zubariy, *Quantum Optics* (Cambridge University Press, Cambridge, 1997).

[38] L. Hornekær, N. Kjærgaard, A. M. Thommesen, and M. Drewsen, Phys. Rev. Lett. **86**, 1994 (2001).

[39] D. J. Wineland, in *Proceedings of the Cooling, Condensation, and Storage of Hydrogen Cluster Ions Workshop* edited by J. T. Bahns (Dayton University, Menlo Park, CA, 1987), p. 181.

[40] S. Schiller and C. Lämmerzahl, Phys. Rev. A **68**, 053406 (2003).

[41] B. Roth, U. Fröhlich, and S. Schiller, Phys. Rev. Lett. **94**, 053001 (2005).

[42] C. B. Zhang, D. Offenberg, B. Roth, M. A. Wilson, and S. Schiller, Phys. Rev. A **76**, 012719 (2007).

[43] P. Blythe, B. Roth, U. Fröhlich, and S. Schiller, Phys. Rev. Lett. **95**, 183002 (2005).

[44] V. Batteiger, S. Knünz, M. Herrmann, G. Saathoff, H. A. Schuessler, B. Bernhardt, T. Wilken, R. Holzwarth, T. W. Hänsch, and Th. Udem, Phys. Rev. A **80**, 022503 (2009).

[45] K. Mølhave and M. Drewsen, Phys. Rev. A **62**, 011401 (2000).

[46] V. L. Ryjkov, X. Zhao, and H. A. Schuessler, Phys. Rev. A **74**, 023401 (2006).

[47] N. S. Harris, *Modern Vacuum Practice* (McGraw-Hill, New York, 2007).

[48] N. Kjærgaard, L. Hornekær, A. M. Thommesen, Z. Videsen, M. Drewsen, Appl. Phys. B **71**, 207 (2000).

[49] E. J. Salumbides, S. Hannemann, K. S. E. Eikema, and W. Ubachs, Mon. Not. R. Astron. Soc. **373**, L41 (2006).

[50] M. Welling, H. A. Schuessler, R. I. Thompson, and H. Walther, Int. J. Mass. Spectrom. **172**, 95 (1998).

[51] M. Levenson and A. Schawlow, Phys. Rev. A **6**, 10 (1972).

[52] J. Hall, L. Hollberg, T. Baer, and H. Robinson, Appl. Phys. Lett. **39**, 680 (1981).

[53] H. Kato, M. Baba, S. Kasahara, K. Ishikawa, M. Misono, et al., *Doppler-Free High Resolution Spectral Atlas of Iodine Molecule 15,000 to 19,000 cm^{-1}* (Japan Society for the Promotion of Science, Japan, 2000).

[54] T. W. Hänsch and B. Couillaud, Opt. Commun. **35**, 441 (1980).

[55] All crystal data taken from SNLO program by Sandia National Laboratories. For further information see http://www.sandia.gov/pcnsc/departments/lasers/snlo-software.html (accessed on 10/6/2010).

[56] D. H. E. Dubin and T. M. O'Neil, Rev. Mod. Phys. **71**, 87 (1999).

[57] X. Zhao, V. Ryjkov, and H. A. Schuessler, Phys. Rev. A **73**, 033412 (2006).

[58] D. F. V. James, Appl. Phys. B **66**, 181 (1998).

[59] H. Totsuji and J. L. Barrat, Phys. Rev. Lett. **60**, 2484 (1988).

[60] R. W. Hasse and J. P. Schiffer, Ann. Phys. (New York) **203**, 419 (1990).

[61] G. Birkl, S. Kassner, and H. Walther, Nature, **357**, 310 (1992).

[62] I. Waki, S. Kassner, G. Birkl, and H. Walther, Phys. Rev. Lett. **68**, 2007 (1992).

[63] J. P. Schiffer, Phys. Rev. Lett. **70**, 818 (1993).

[64] S. Schiller and V. Korobov, Phys. Rev. A **71**, 032505 (2005).

[65] D. DeMille, Phys. Rev. Lett. **88**, 067901 (2002).

[66] A. Rahman and J. P. Schiffer, Phys. Rev. Lett. **57**, 1133 (1986).

[67] K. Okada, K. Yasuda, T. Takayanagi, M. Wada, H. A. Schuessler, and S. Ohtani, Phys. Rev. A **75**, 033409 (2007).

[68] T. Baba and I. Waki, Appl. Phys. B **74**, 375 (2002).

[69] M. Bussmann, U. Schramm, D. Habs, V. S. Kolhinen, and J. Szerypo, Int. J. Mass. Spectrom. **252**, 179 (2005).

[70] A. Ostendorf, C. B. Zhang, M. A. Wilson, D. Offenberg, B. Roth, and S. Schiller, Phys. Rev. Lett. **97**, 243005 (2006).

[71] L. Collatz, *The Numerical Treatment of Differential Equations* (Springer, Berlin, 1960).

[72] J. Prestage, A. Williams, L. Maleki, M. Djomehri, and E. Harabetian, Phys. Rev. Lett. **66**, 2964 (1991).

[73] J. P. Schiffer, M. Drewsen, J. S. Hangst, and L. Hornekr, Proc. Natl. Acad. Sci. U.S.A. **97**, 10697 (2000).

[74] T. Schätz, U. Schramm, and D. Habs, Nature **412**, 717 (2001).

[75] T. M. Kojima, N. Oshima, D. Dumitriu, H. Oyama, A. Mohri, and Y. Yamazaki, Riken Rev. **31**, 70 (2000).

[76] P. Banks, Planet. Space Sci. **14**, 1105 (1966).

[77] V. L. Ryjkov, X. Zhao, and H. A. Schuessler, Phys. Rev. A **71**, 033414 (2005).

[78] H. S. Lakkaraju, P. J. Walian, and H. A. Schuessler, J. Appl. Phys. **72**, 3246 (1992).

[79] B. Roth and S. Schiller, in *Cold Molecules: Theory, Experiment, Applications* edited by R. Krems, B. Friedrich, and W. Stwalley (Taylor & Francis Group, Boca Raton, FL, 2009), pp. 651-704.

[80] M. Babiker, W. L. Power, and L. Allen, Phys. Rev. Lett. **73**, 1239 (1994).

[81] M. F. Andersen, C. Ryu, P. Clade, V. Natarajan, A. Vaziri, K. Helmerson, and W. D. Philips, Phys. Rev. Lett. **97**, 170406 (2006).

[82] A. E. Siegman, *Lasers* (University Science Books, Mill Valley, CA, 1986).

[83] J. Strohaber, Ph.D. dissertation, University of Nebraska, 2008.

[84] L. Allen, M. W. Beijersbergen, R. J. C. Spreeuw, and J. P. Woerdman, Phys. Rev. A, **45**, 8182 (1992).

[85] R. A. Beth, Phys. Rev. **50**, 115 (1936).

[86] S. Allen, S. Barnett, and M. J. Padgett (eds.), *Optical Angular Momentum* (IOP Publishing, Bristol, 2003).

[87] K. Vahala, M. Herrmann, S. Knünz, V. Batteiger, G. Saathoff, T. W. Hänsch, and Th. Udem, Nature Phys. **5**, 682 (2009).

[88] S. Knünz, M. Herrmann, V. Batteiger, G. Saathoff, T. W. Hänsch, K. Vahala, and Th. Udem, Phys. Rev. Lett. **105**, 013004 (2010).

VITA

Feng Zhu received his Bachelor of Science degree from the Department of Physics at Tsinghua University, Beijing, China. He entered the Department of Physics at Texas A&M University in January 2002, received his Master of Science degree in August 2005, and received his Ph.D. degree in December 2010. For his address and other current information please contact Prof. Hans A. Schuessler, Department of Physics and Astronomy, College Station, TX 77843-4242